Nuclear envelope tethering of the genome modulates cohesin loop extrusion

Fengnian Shan[1,9], Han Zhao[1,8,9], Shiyi Qin[1,9], En Lin[1,9], Sijian Xia[2,9], Yinzhi Lin[3,4,1,9], Fangxuan Lyu[1], Chongren Pei[1], Fuhai Liu[1], Qiao Guo[4], Siyu Li[5], Lirong Shu[3,4,1], Manzhu Wang[2], Yongjia Weng[6], Bicheng Li[1], Kai Huang[1,*] and Haoyue Zhang[1,*]

[1] Institute of Molecular Physiology, Shenzhen Bay Laboratory, Shenzhen, Guangdong, China
[2] School of Basic Medicine, Capital Medical University, Beijing, China
[3] Shenzhen Medical Academy of Research and Translation, Shenzhen, China
[4] Westlake University, Hangzhou, China
[5] School of Biological Science, The University of Hong Kong, Hong Kong, China
[6] State Key Laboratory of Biotherapy, Sichuan University
[7] Cancer Institute, Peking University- Hong Kong University of Science and Technology (PKU-HKUST) Medical Center, Shenzhen, Guangdong, China
[8] Present affiliation: College of Life Sciences, Hunan Normal University, Hunan, China
[9] These authors contribute equally to this work.

*Correspondence:
zhang_adam@szbl.ac.cn (H. Zhang)
huangkai@szbl.ac.cn (K.H.)

Abstract:

The nuclear envelope (NE) plays a crucial role in genome organization by tethering heterochromatin to the nuclear periphery. Yet, how individual NE-associating factors regulate 3D genome architecture remains incompletely understood. Here, we leverage the mitosis-to-G1 phase transition as an experimental system to dissect the roles of Lamin A/C and Lamin B receptor (LBR) in post-mitotic genome refolding. Loss of LBR but not Lamin A/C triggers profound architectural aberrations, including enhanced self-interaction of lamina-associating domains (LADs) and a concomitant decrease in local intra-loop contacts. Although LBR rapidly re-associates with chromatin in early-G1, its structural impacts manifest only in late-G1, suggesting a temporal decoupling between chromatin binding and architectural function. Mechanistically, we demonstrate that such aberrations are not driven by altered heterochromatin self-attraction, but instead reflect the relief of a biophysical constraint imposed by LBR on cohesin-mediated loop extrusion. In support of this, reducing cohesin occupancy via Nipbl degradation mitigates the architectural impacts of LBR loss, while selective mapping of cohesin contacts reveals that LBR depletion directly increases cohesin extrusion processivity. Moving beyond an LBR-centric view, we extend these findings through an inducible synthetic tethering system and polymer simulations to establish a universal NE-mechanical tethering framework. In this framework, the NE regulates cohesin loop extrusion in a tethering-mode-specific manner: while bulk chromatin anchorage imposes a mechanical constraint that restricts cohesin processivity, focal tethering of CTCF-binding sites (CBS) facilitates loop formation. Our study establishes the NE as a general mechanical governor of the genome that regulates 3D chromatin architecture by modulating cohesin extrusion capacity.

Introduction:

The nuclear envelope (NE) is a composite structure defined by the nuclear membranes and the underlying nuclear lamina (NL), a filamentous meshwork primarily composed of Lamin proteins (Lamin A, C, B1, and B2) [1,2]. The NL interacts with a variety of factors that are integral to the inner nuclear membrane (INM), such as Lamin B1 receptor (LBR), SUN1 and Emerin [3-5]. Both NL and INM-associating proteins have been shown to interact with the genome, providing a docking site for chromatin at the nuclear periphery [6-9]. Genomic regions that interact with the NL are collectively termed as the lamina-associating domains (LADs) [10-13]. LADs typically span hundreds of kilobases to megabase scales, are frequently located in gene-poor regions, and are often enriched with the constitutive heterochromatin mark H3K9me3, accounting for approximately 30-40% of the genome [10,12-15]. Artificial tethering of active genes to the NL can induce gene silencing, indicating a direct suppressive effect of NL on transcription [16]. Accordingly, tissue-specific genes relocate from the NL to the nuclear interior to activate transcription during differentiation [17,18].

Chromatin within the nucleus is not randomly distributed but folds into a multi-layered hierarchical organization [19-21]. At the megabase scale, chromatin can be partitioned into two mutually segregated compartments: the euchromatin-enriched A-type compartments and heterochromatin-enriched B-type compartments [19]. At finer scales, chromatin is organized into topologically associating domains and chromatin loops by loop extrusion, a process wherein cohesin complexes translocate along the DNA fiber, extruding loops until arrested by convergently oriented CTCF molecules [22-27]. The exact mechanism underpinning A/B chromatin compartmentalization is not fully understood. Integrative analysis reveals a remarkable overlap between B-type compartments and LADs, suggesting that heterochromatin tethering to the nuclear periphery may play a role in regulating genome compartmentalization [12,28]. However, studies investigating this relationship have yielded controversial findings. In *C.elegans*, disruption of perinuclear heterochromatin tethering by deleting CEC4 was shown to diminish the segregation between A/B compartments [29]. In mammalian cells, deletion of Lamin B1 was reported to attenuate compartmentalization [30]. A recent study reported that triple knockout of Lamin A, B1 and B2 in human mesenchymal stem cells resulted in extensive weakening of chromatin compartmentalization [31]. However, a similar triple knockout of Lamins in mouse embryonic stem cells failed to show such dramatic changes in

compartments [32]. In the striking case of inverted nuclei, in which heterochromatin tethering is completely abolished due to the combined loss of Lamin A/C and LBR, chromatin compartmentalization remains largely unaffected [33]. These conflicting observations suggest that our understanding of how the NE influences genome organization is fundamentally incomplete.

Chromatin architecture is dynamically regulated throughout the cell cycle [34-42]. During mitosis, hallmark chromatin architectural features including A/B compartments, topologically associating domains (TADs), and chromatin loops are transiently disrupted [35,41]. Concurrently, the NE is disassembled [8,43]. As cells enter G1, chromatin structures are gradually established, coinciding with the re-establishment of LADs [8,34,35,39,44]. Different NL components and INM-associating proteins may exhibit diverse chromatin re-association dynamics. Live-cell imaging experiments revealed that Lamin B1 and LBR rapidly coat the still-condensed genome during ana/telophase, while Lamin A/C exhibits a delayed recruitment [44-46]. This transitional stage from mitosis to G1 phase offers a unique opportunity to investigate how NL components and INM-associating factors regulate the *de novo* re-establishment of chromatin architecture.

Here, we aim to dissect the roles of Lamin A/C and LBR, two crucial factors mediating heterochromatin perinuclear distribution, in the *de novo* re-establishment of the interphase genome. We identify LBR, but not Lamin A/C, as a critical regulator of post-mitotic chromatin re-configuration. We find that LBR functions by restricting the processivity of cohesin-mediated loop extrusion within LADs. Importantly, utilizing an inducible artificial tethering system and polymer simulations, we expand this observation to show that the inhibitory role of LBR on cohesin is not dependent on its specific biochemical features. Instead, it represents a generalized principle, in which the spatial positioning of chromatin at the nuclear periphery serves as a biophysical constraint to suppress cohesin extrusion capacity. We further complemented this principle by demonstrating that focal tethering of CTCF-binding sites (CBS) to the NE, unlike bulk anchorage, facilitates loop stabilization rather than cohesin restriction. Collectively, our study establishes a universal NE-mechanical tethering framework where the NE serves as a general mechanical governor of the genome, regulating 3D chromatin architecture through mode-specific mechanical effects on cohesin processivity.

Results:

Post-mitotic chromatin re-association dynamics of Lamin A/C, Lamin B1 and LBR.

To dissect the specific contributions of different nuclear periphery factors to post-mitotic genome re-establishment, we first sought to characterize their dynamic re-association with chromatin after cell division. We conducted cleavage under targets and tagmentation (CUT&Tag) experiments [47], at defined time points following nocodazole-mediated prometaphase arrest and release in G1E-ER4 cells, a well-characterized erythroblast line (Fig. 1a). We focused on two important factors, previously implicated in mediating NE-heterochromatin tethering: Lamin A/C and LBR (Fig. 1a) [48]. Lamin B1 was tested in parallel (Fig. 1a). To ensure high purity of cell populations, we employed a fluorescence-activated cell sorting (FACS) strategy based on a mitotic-degron cell cycle marker and DNA content staining (Extended Data Fig. 1a, b) [35,49].

We obtained highly concordant CUT&Tag datasets among biological replicates (Extended Data Fig. 1c, d). At 45 minutes post nocodazole-release, chromatin exhibited robust LBR association that overlapped with the constitutive heterochromatin mark H3K9me3 and inversely correlated with genome-wide eigenvector 1 (EV1) values (Fig. 1b; Extended Data Fig. 1d, e). This finding corroborates the previously reported overlap between LADs and B-type compartments [12,32]. Notably, Lamin B1 showed no discernible chromatin binding at this early stage (Extended Data Fig. 1d). As cells proceed to late-G1 phase (4h), both LBR and Lamin B1 occupancy were strengthened, with LBR displaying a more rapid re-association (Fig. 1c; Extended Data Fig. 1d). Interactions between Lamin A/C and chromatin were undetectable until late-G1 phase, suggesting a significantly slower re-association kinetics (Extended Data Fig. 1d). Furthermore, Lamin A/C occupancy at late-G1 phase was less correlated with B-type compartments than LBR or Lamin B1, implying a potentially distinct role in genome organization (Fig. 1b). Taken together, our data define a sequential re-association of NE-factors with chromatin after mitosis, following the order: LBR > Lamin B1 > Lamin A/C.

Genome-wide classification of LADs.

Given that LBR exhibits stronger chromatin binding and more extensive overlap with B-compartments than Lamin B1 or Lamin A/C (Fig. 1b; Extended Data Fig. 1d), we focused our analysis on LBR-associating genomic regions. Given their nearly identical distribution to

156 classically defined lamina-associating domains, we refer to these regions as LADs throughout this
157 study to maintain consistency with established nomenclature, while noting their specific
158 enrichment for LBR.
159
160 We identified a non-redundant set of 1,022 LADs genome-wide (Supplementary Table 1)
161 according to LBR CUT&Tag signals. Using *k*-means clustering, we subcategorized LADs into
162 three distinct types: Type1 (rapid-forming, n=179) LADs reached near-maximal LBR and Lamin
163 B1 binding at 1h and 2h, respectively, after mitosis (Fig. 1d-f); Type 2 (slow-forming, n=777)
164 LADs exhibited a more progressive accumulation of LBR and Lamin B1 signals, which continued
165 to strengthen until 4h post-mitosis (Fig. 1d-f); and Type 3 (transient, n=66) LADs displayed
166 transient chromatin binding signals during early-G1 (45min-1h) that gradually diminished in late-
167 G1 (Fig. 1d-f).
168
169 Closer examination revealed distinct epigenetic and positional features of LAD subtypes. Type1
170 LADs displayed the highest enrichment of H3K9me3 and were preferentially occupied by lamins
171 and LBR (Fig. 1g, h). Interestingly, we found that Type 1 LADs were predominantly located at
172 telomere-proximal regions (Extended Data Fig. 1f, g). By contrast, Type2 LADs were positioned
173 closer to centromeres (Extended Data Fig. 1f, g). Type3 LADs were also found to be telomere-
174 proximal (Extended Data Fig. 1f, g), consistent with a prior report of transient chromatin-lamina
175 interactions near telomeres after mitosis [8]. In summary, these results demonstrate that genomic
176 positioning may regulate the kinetics of chromatin association with the NE following mitosis.
177
178 **Lamin A/C loss does not affect post-mitotic genome refolding.**
179 The weak and delayed re-association of Lamin A/C with chromatin prompted us to evaluate its
180 role in post-mitotic genome refolding. We engineered a G1E-ER4 cell line harboring a minimal
181 auxin-inducible degron (mAID) tagged to the N terminus of endogenous Lamin A/C protein
182 (*Lmna*^{mAID}), and co-expressed OsTIR2 to enable rapid protein degradation (Extended Data Fig.
183 2a-d) [50]. Intriguingly, prolonged depletion of Lamin A/C did not affect cell proliferation (Extended
184 Data Fig. 2e). To determine the effects of Lamin A/C loss on post-mitotic genome reorganization,
185 we conducted *in-situ* Hi-C on synchronously purified *Lmna*^{mAID} cells at defined intervals following
186 mitosis, with or without 5-Ph-IAA treatment (Extended Data Fig. 2f). Consistent with prior studies,

A/B compartments re-emerged in early-G1 phase (1h) and were progressively intensified in the untreated control samples (Extended Data Fig. 2g) [35]. Importantly, acute depletion of Lamin A/C failed to induce any detectable alterations in this process (Extended Data Fig. 2g). In line with this, we observed highly concordant EV1 values in cells with or without Lamin A/C after mitosis (Extended Data Fig. 2h). Reordering saddle plots based on Lamin A/C CUT&Tag signal intensity revealed that the self-association of genomic regions with high Lamin A/C density was not affected by Lamin A/C loss (Extended Data Fig. 2i, j). Finally, loss of Lamin A/C failed to disrupt the re-establishment of TADs, CTCF/cohesin-anchored structural loops or contacts between *cis*-regulatory elements (CREs) (Extended Data Fig. 3a-e). Taken together, our data indicate that Lamin A/C is dispensable for the re-establishment of higher-order chromatin architecture following mitosis. Consistent with this structural preservation, transient-transcriptome sequencing (TT-seq) revealed that post-mitotic transcription reactivation proceeded normally in the absence of Lamin A/C (Extended Data Fig. 3f). While Lamin A/C appears non-essential for the initial folding of the post-mitotic genome, it remains to be determined whether its long-term loss leads to more pronounced defects.

LBR loss progressively strengthens LAD self-association *in cis* but not *in trans* after mitosis.

The resilience of post-mitotic genome refolding to Lamin A/C loss may reflect a compensatory role for LBR, which is known to anchor heterochromatin at the nuclear periphery in the absence of Lamin A/C [48]. Utilizing CRISPR/Cas9-directed genome editing, we generated a dual inducible degron cell line with mAID tagged to Lamin A/C and a proteolysis targeting chimera (PROTAC) FKBP12^{F36V} degron (dTag) fused to LBR (*Lmna*^{mAID}/*Lbr*^{dTag}) (Fig. 2a; Extended Data Fig. 4a-e) [51]. Of note, the dTag system exhibited a high level of background degradation (Extended Data Fig. 4f, g). dTag13 treatment further reduced LBR signal intensity to an undetectable level (Extended Data Fig. 4f, g). To delineate the specific function of LBR in post-mitotic genome refolding, we fully ablated LBR in the *Lmna*^{mAID}/*Lbr*^{dTag} cells using dTag13 treatment. We performed *in situ* Hi-C at post-mitotic time points benchmarked against our previously established *Lmna*^{mAID} datasets, which served as the LBR-replete control (Fig. 2b). Given that LBR is fully associated with chromatin by early-G1 (1h) and can promote chromatin compaction *in vitro* [52], we postulated that its loss would immediately affect the re-establishment of genome architecture in newborn cells, potentially disrupting the self-association of LADs.

Contrary to our initial hypothesis, homotypic interactions among Type 1 LADs were unaffected in early-G1 following LBR loss, despite robust chromatin occupancy of LBR at this stage (Fig. 2c-e). Remarkably, starting from mid-G1 (2h), we observed an increase in Type 1 LAD self-association in the absence of LBR. This gain in contacts became progressively more pronounced as cells proceeded into late G1 (4h and 6h) (Fig. 2d, e). A similar, albeit delayed, increase in homotypic contacts occurred for Type 2 LADs, manifesting only during the late-G1 phase (Fig. 2d, e). The effect size for Type2 LADs was smaller compared to that of Type 1, consistent with their lower levels of LBR binding (Fig. 1h; 2d, e). Meanwhile, contacts among Type 3 LADs, which displayed the lowest LBR signals, remained unperturbed across all tested time points (Fig. 1h; 2e). Given the extensive overlap between LADs and heterochromatin, we next examined whether these changes extended to the compartment level genome-wide. Consistent with our findings in LADs, we observed a gain in B-B compartmental interactions following LBR loss that became increasingly pronounced as progressed into late-G1 (Extended Data Fig. 5a–c). Taken together, our data indicate that LBR does not promote heterochromatin self-clustering immediately after mitosis, but instead plays a delayed role in restraining its self-association.

We next assessed whether LBR inhibits LAD self-association by modulating their homotypic affinity. We reasoned that if LBR loss increased homotypic affinity of LADs, the resulting interaction gains should occur uniformly in both intra-chromosomal (*cis*) and inter-chromosomal (*trans*) contexts. To test this, we generated saddle plots by ranking genomic bins based on their LBR occupancy. This analysis revealed a critical divergence: while *cis*-interactions among LBR-enriched regions were markedly enhanced upon LBR loss in late-G1, trans-interactions exhibited no such gain (Fig. 2f). This phenotypic confinement to *cis*-interactions argues against a model of increased homotypic affinity between LADs. Instead, our data implicate a progressive, intra-chromosomal-centric mechanism, through which LBR regulates post-mitotic genome architecture. Notably, the above observations were fully recapitulated in cells lacking Lamin A/C, corroborating that Lamin A/C does not participate in post-mitotic genome refolding (Extended Data Fig. 6a-g).

LBR loss attenuates the progressive intensification of intra-loop contacts after mitosis.

Cohesin-mediated loop extrusion represents a compelling candidate mechanism that establishes a link between LBR and chromatin architecture. It is operated predominantly *in cis* and has been shown to influence heterochromatin organization, providing a plausible explanation for the altered self-association of LADs [38]. Furthermore, the established progressive reloading of cohesin after mitosis provides a temporal basis for the delayed impact of LBR loss on chromatin structure [35]. These converging lines of evidence prompted us to assess whether LBR influences cohesin-mediated loop extrusion.

To begin with, we asked whether LBR loss would affect post-mitotic chromatin loop reformation. Using a modified HICCUPS algorithm, we identified 17,345 loops (Supplementary Table 2) progressively gained from early- (1h) to late-G1 phase (6h) [35-38]. LBR ablation did not measurably alter the number of loop calls throughout G1 phase (Extended Data Fig. 7a). CRE contacts (n=3,970) remained largely unaffected without LBR (Extended Data Fig. 7b). In line with this, post-mitotic transcription reactivation only displayed a minor change (Supplementary Note 1, Extended Data Fig. 7c-f). We then focused on structural loops (n=5,236) demarcated by CTCF/cohesin binding at both anchors [35-38]. Aggregated peak analysis (APA) revealed that the intensity of structural loops was only marginally affected LBR loss (Extended Data Fig. 7g). These data indicate that the loop-forming capacity of cohesin remained largely intact in the absence of LBR.

Besides stable, CTCF-anchored structural loops, cohesin-mediated loop extrusion may also yield dynamic extruding intermediates that are not yet arrested by CTCF barriers. These transient structures collectively contribute to the population-averaged composite signal of interactions within stable structural loops (intra-loop contacts) (Fig. 2g). Visual inspection of Hi-C contact matrices revealed progressively intensified intra-loops after mitosis (Fig. 2h). This enrichment of nested interactions suggests elevated levels of extruding intermediates, consistent with gradually increased cohesin occupancy after mitosis (Fig. 2h). Remarkably, LBR depletion specifically weakened these intra-loop contacts in late- but not early-G1 phase, corroborating its delayed impact on post-mitotic genome re-configuration (Fig. 2h). The magnitude of this reduction scaled positively with the average LBR occupancy within loop bodies, suggesting a role of LBR in regulating cohesin-mediated extruding intermediates (Fig. 2i). Reintroducing full-length LBR in

the dTag13-treated *Lmna*^{mAID}/*Lbr*^{dTag} cells partially rescued the defects in intra-loop contact signals (Supplementary Note 2; Extended Data Fig. 8a, b). Furthermore, the reduction in intra-loop contacts upon LBR depletion was fully recapitulated in Lamin A/C-deficient cells (Extended Data Fig. 6h, i). Notably, this phenotype was not restricted to G1E-ER4 cells, as LBR-deficient C2C12 cells exhibited a similar reduction in intra-loop contacts, ruling out the possibility of cell-type-specific artifact (Supplementary Note 3; Extended Data Fig. 9).

In sum, our data imply that LBR could reinforce intra-loop contact strength (a proxy of extruding intermediates) within LADs, potentially by modulating the processive extrusion of cohesin, as it is gradually loaded after mitosis.

Reducing cohesin loading attenuates the impact of LBR loss on post-mitotic genome refolding.

To test the hypothesis that LBR regulates 3D chromatin architecture by modulating cohesin-driven loop extrusion, we investigated whether reducing cohesin occupancy could mitigate the phenotypic consequences of LBR loss on post-mitotic genome refolding. To approach this, we utilized our previously generated orthogonal dual-inducible degradation cell line *Nipbl*^{mAID}/*Wapl*^{dTag}, which allows for independent acute degradation of the cohesin loading factor Nipbl or/and releasing factor Wapl via 5-Ph-IAA or/and dTag13 treatment, respectively (Fig. 3a; Extended Data Fig. 10a) [23,27]. LBR-knockout clones (*Lbr*$^{-/-}$) were generated in this background (Fig. 3b). Control and *Lbr*$^{-/-}$ cells were arrested at prometaphase using nocodazole and selectively depleted of Nipbl using 5-Ph-IAA (Fig. 3c). Subsequently, cells were released from nocodazole for 6 hours and late-G1 phase samples were isolated using FACS for *in-situ* Hi-C experiments (Fig. 3c). Consistent with previous reports, degrading Nipbl resulted in reduced cell proliferation and a massive loss of structural loops, particularly those spanning larger genomic distances (Extended Data Fig. 10b-e). Notably, this loss of loops was similarly evident the *Lbr*$^{-/-}$ cells (Extended Data Fig. 10b-e).

Degrading Nipbl led to a significant reduction of intra-loop contacts in the control *Lbr*$^{+/+}$ cells, confirming that these internal signals are largely driven by cohesin loop extrusion (Fig. 3d, e). These results establish intra-loop contact signals as a robust metric for measuring loop extrusion

activity. Consistent with our results in the LBR-degron line (*Lmna*^{mAID}/*Lbr*^{dTag}), LBR knockout in the untreated *Nipbl*^{mAID}/*Wapl*^{dTag} cells also led to a marked reduction in intra-loop contacts within LADs (Fig. 3d, e), which coincided with increased LAD self-association (Fig. 3g-i; Extended Data Fig. 10f, g). Crucially, the impact of LBR loss on both intra-loop contacts (Fig. 3f) and LAD self-clustering was significantly attenuated upon Nipbl degradation (Fig. 3g-i; Extended Data Fig. 10f, g). The fact that Nipbl depletion mitigates the structural changes induced by LBR loss demonstrates that LBR's regulatory influence on 3D genome architecture is mechanistically contingent upon active cohesin loop extrusion.

LBR potentially constrains cohesin loop extrusion within LADs.

Having established that LBR's impact on genome architecture is cohesin-dependent, we next investigated how LBR modulates cohesin loop extrusion. We sought a single mechanistic model to unify the observed reduction of intra-loop contacts as well as the extensive strengthening of LAD self-association in *cis* upon LBR loss. We reasoned that both phenotypes could be driven by the cohesin hyper-processivity, a state previously exemplified by Wapl depletion [23]. In Wapl-deficient cells, hyper-processive cohesin produces two linked outcomes: (1) a reduction in local, short-range extruding intermediates, manifesting as reduced intra-loop contact frequency (Extended Data Fig. 11a), and (2) an increase in homotypic B-B interactions as cohesin travels beyond CTCF anchors and juxtaposes distal B-type compartments (Extended Data Fig. 11a). This change in extrusion capacity is characterized by a bidirectional shift in the distance-dependent contact probability decay curves (P_S): a reduction in contact probability for short genomic separations (<1Mb) and an increase in contact strength for larger genomic distances (1-10Mb) (Extended Data Fig. 11b). Importantly, LBR-deficient cells also exhibit a similar bidirectional shift in the P_S curve, albeit less pronounced compared to Wapl deficiency (Fig. 3j). Crucially, deleting Nipbl strongly attenuated the LBR loss-induced changes in P_S curve, confirming that these architectural alterations are driven by cohesin (Fig. 3j). The phenotypic similarities between LBR and Wapl deficiency suggest that LBR potentially constrains cohesin loop extrusion. In its absence, cohesin extrudes more extensively within LADs.

We reasoned that if LBR acts to suppress cohesin loop extrusion, then maximizing cohesin extrusion potential should theoretically override its regulatory influence. To test this, we examined

the outcome of LBR loss in a Wapl-deficient background, where cohesin becomes hyper-processive. To approach this, we treated both *Lbr*$^{+/+}$ and *Lbr*$^{-/-}$ *Nipbl*^{mAID}/*Wapl*^{dTag} cells with dTag13 to eliminate Wapl and collected late-G1 phase samples for Hi-C experiments (Fig. 3c). As expected, Wapl removal induced extensive structural loop formation (Fig. 3d; Extended Data Fig. 10c-e). Remarkably, this state of constitutive hyper-extrusion almost completely abolished the architectural changes induced by LBR loss (Fig. 3d-j; Extended Data Fig. 10f, g).

Taken together, our data support a model wherein LBR constrains cohesin loop extrusion, particularly within LADs. Deleting LBR unleashes this constraint, transforming the extrusion landscape from nested, short-range intermediates into large, expansive ones that facilitate long-range interactions of distal LADs (Fig. 3k).

Selective mapping of cohesin-mediated contacts confirmed a role of LBR in constraining loop extrusion.

Conventional Hi-C experiments capture the combined signals of both cohesin loop extrusion and affinity based homotypic heterochromatin interactions. To rigorously deconvolute loop extrusion from heterochromatin compartmentalization and unveil LBR's impact on both mechanisms, we employed a parallel micro-HiChIP strategy [53], a high-resolution method combining micrococcal nuclease digestion with HiChIP, on the *Nipbl*^{mAID}/*Wapl*^{dTag} cells with or without LBR (Fig. 4a). We targeted Rad21 to exclusively capture cohesin-mediated contacts (Supplementary Note 4; Fig. 4a; Extended Data Fig. 12a-c). In parallel, we performed H3K9me3 micro-HiChIP in a Nipbl-depleted background to isolate intrinsic heterochromatic affinity signals, while minimizing confounding influences from loop extrusion (Supplementary Note 4; Fig. 4a; Extended Data Fig. 12d-f).

Rad21 micro-HiChIP uncovered structural details that were obscured in conventional Hi-C. In the *Lbr*$^{+/+}$ control cells, for structural loops located within LADs, cohesin-mediated contacts were concentrated near the diagonal, indicative of abundant short-range extruding intermediates (Fig. 4b). Upon LBR depletion, these diagonal-proximal contacts were dramatically attenuated, whereas larger contacts within the same loop were increased (Fig. 4b; Extended Data Fig. 13a). To quantitatively define these changes, we segmented each structural loop into 100kb stripes (Fig. 4c).

For each stripe, we calculated the $\log_2$ fold change in contact frequency upon LBR loss. Deleting LBR induced a marked drop in contacts for short genomic separations (<2Mb) and a progressive increase in contacts at genomic distances beyond 2-3Mb, specifically within LAD-located structural loops (Fig. 4d; Extended Data Fig. 13a, b). By contrast, no such effects were observed for loops outside of LADs, confirming a direct involvement of LBR in regulating cohesin-mediated contacts (Fig. 4d; Extended Data Fig. 13a, b). This expansion of extrusion intermediates produced a bi-directional shift in the P_S curve, mirroring what we observed in Hi-C experiments but with a larger effect size (Fig. 3j, 4e).

In contrast to the dramatic shifts observed in cohesin-mediated contacts (Fig. 4b-e), Loss of LBR in the Nipbl-deficient background triggered only mild perturbations in the H3K9me3 micro-HiChIP contact maps, for both intra-loop contact signals (Fig. 4f-h) and P_S curves (Fig. 4i). Furthermore, while the H3K9me3 micro-HiChIP maps showed an increase in LAD self-association upon LBR depletion, these changes occurred largely among regions with the highest occupancy of LBR (Fig. 4l, m; Extended Data Fig. 13e, f). By contrast, Rad21-mediated contacts exhibited a more global and pronounced strengthening of LAD self-aggregation (Fig. 4j, k; Extended Data Fig. 13c, d, g, h). Importantly, as residual cohesin activity can persist even under Nipbl-deficient conditions, the modest changes we observed in the H3K9me3 micro-HiChIP maps may be partially inflated by trace extrusion activity. Hence, the direct impact of LBR on intrinsic chromatin affinity is likely even more negligible than these measurements suggest [54].

Taken together, our data demonstrate that LBR organizes the 3D genome primarily by imposing a regulatory constrainton cohesin-mediated loop extrusion, whereas its contribution to affinity-based heterochromatin self-association is comparatively negligible.

Artificial tethering of bulk chromatin to the nuclear rim constrains cohesin loop extrusion.

Our rescue experiments revealed that the transmembrane domain of LBR is indispensable for restoring intra-loop contacts in LBR-deficient cells (Supplementary Note 2; Extended Data Fig. 8), underscoring the necessity of membrane localization for LBR-mediated cohesin regulation. This finding suggests that LBR's architectural impact may stem from its capacity to physically link chromatin to the NE.

We therefore moved beyond an LBR-centric view to propose a generalized biophysical model: mechanical anchorage of chromatin to the nuclear periphery, independent of the specific molecular bridge, generates tension or biophysical resistance that antagonizes the processivity of the cohesin motor (Fig. 5a). We reason that if this model holds true, then artificial anchorage of chromatin to the nuclear rim, using synthetic tools entirely independent of LBR, should be sufficient to counteract cohesin loop extrusion in the *Lbr*$^{-/-}$ cells and recapitulate the architectural constraints observed in LBR-replete samples.

To test this, we developed an inducible artificial nuclear peripheral tethering system using the plant abscisic acid (ABA)-dependent dimerization module (ABI-PYL1) [55]. In our system, the ABI module was fused to H2B (H2B-ABI^{HaloTag}) to label bulk chromatin, while the PYL1 module was fused to Lamin A (Lamin A-PYL1^{GFP}) to serve as a nuclear peripheral bait (Fig. 5b). These constructs were ectopically expressed in the *Lbr* $^{-/-}$ cells, enabling the rapid, ABA-induced sequestration of chromatin to the nuclear lamina (Fig. 5b). We selected Lamin A as the nuclear periphery anchor because our prior data demonstrated that Lamin A/C depletion does not inherently disrupt chromatin architecture. This allowed us to use Lamin A as a functionally neutral docking site, thereby maximally isolating the biophysical impact of peripheral recruitment *per se* from other potential biochemical confounding factors. Incubating the cells with ABA induced a widespread peripheral recruitment of H2B within 24 hours (Fig. 5c; Extended Data Fig. 14a). This was accompanied by a concomitant concentration of DAPI signal at the nuclear rim, demonstrating the parallel relocation of DNA and confirming the successful tethering of bulk chromatin (Fig. 5c; Extended Data Fig. 14a).

Remarkably, Rad21 micro-HiChIP experiments revealed that ABA-treated cells displayed a marked increase in short-range intra-loop contacts compared to DMSO-treated controls (Fig. 5d, e; Extended Data Fig. 14b), mirroring the phenotypic differences observed between *Lbr* $^{+/+}$ and *Lbr* $^{-/-}$ cells (Fig. 4b-d). Notably, this restriction was most pronounced in loops located within LADs (Fig. 5f; Extended Data Fig. 14c). We reason that this effect is attenuated in non-LAD regions due to the high density of CTCF in euchromatin, which likely acts as a dominant architectural barrier that overrides the mechanical constraints imposed by peripheral tethering.

Furthermore, bulk-chromatin tethering to the nuclear periphery led to a selective reduction in the signal intensity of large chromatin loops, while smaller loops remained relatively unaffected (Fig. 5d, e, g; Extended Data Fig. 14b, d), consistent with the notion that loop extrusion was inhibited. Notably, the reduction in loop signal was not caused by a decrease in Rad21 binding at loop anchors (Fig. 5h; Extended Data Fig. 14e).

Taken together, by utilizing Lamin A as a neutral dock to isolate the physical consequences of NE-tethering, our results establish that simple physical anchorage of the genome to the nuclear periphery is sufficient to restrict cohesin loop extrusion.

Focal tethering of CTCF binding sites (CBS) to the nuclear periphery stabilizes long-range loops.

Having established that sequestration of bulk chromatin to the nuclear rim restricts cohesin processivity, we next investigated whether anchoring specific genomic landmarks (focal-tethering) to the NE would elicit similar or diverse effects. We focused on CTCF binding sites (CBS), the primary genomic signature responsible for arresting cohesin loop extrusion. To address this, we endogenously fused a HaloTag-ABI module to the C-terminus of CTCF and co-expressed a PYL1-GFP-Lamin A fusion protein to serve as the nuclear rim bait (Fig. 6a, b; Extended Data Fig. 15a). The CTCF-ABI^{Halo} protein maintained the native genomic binding profiles of wildtype CTCF (Extended Data Fig. 15c). Treating these cells with ABA for 24 hours induced a widespread enrichment of CTCF at the nuclear periphery (Fig. 6c), allowing us to selectively evaluate the impact of CBS nuclear lamina anchoring on cohesin-mediated loop extrusion.

ChIP-seq experiments revealed that CTCF-ABI^{Halo} occupancy remained consistent before and after ABA treatment (Fig. 6d, e; Extended Data Fig. 15c, d). Remarkably, despite invariant CTCF occupancy, Rad21 micro-HiChIP revealed a widespread gain of cohesin binding at CBS following ABA treatment (Fig. 6d, e; Extended Data Fig. 15c-e). Of note, protein levels of the cohesin core subunits SMC1 and Rad21 remained unaffected (Extended Data Fig. 15b). This result indicates that relocating CBS to the nuclear rim facilitates focal deposition of cohesin. To investigate whether altered cohesin binding profiles could also affect chromatin loop formation, we performed HICCUPS analysis. We identified a greater number of loops in the ABA-treated samples compared

to the controls (Fig. 6f). In line with this, quantitative analysis unveiled significantly enhanced loop strength upon ABA treatment (19,259, 46.55% loops increased with 1.5-fold cutoff) (Fig. 6g-i; Extended Data Fig. 15f).

This reinforcement represents a striking divergence from the H2B-mediated bulk chromatin tethering, in which large chromatin loops were significantly reduced (Fig. 5d, e, g; Extended Data Fig. 14b, d). Analysis of loop strength relative to loop sizes indicates that both large and small loops were strengthened upon ABA treatment, suggesting a general role for peripheral CBS anchoring in stabilizing CTCF/cohesin-mediated chromatin loops (Fig. 6j, k; Extended Data Fig. 15g). Finally, we examined loop extrusion intermediates. Unlike the bulk-tethered samples, in which intra-loop contacts were shifted toward short ranges, peripheral CBS docking did not measurably alter these interactions (Extended Data Fig. 15h, i). These results suggest that cohesin processivity remains largely unperturbed when tethering is restricted to a limited number of isolated loci.

Taken together, our results highlight a phenotypic divergence between focal- and bulk-tethering of the genome. While sequestering bulk chromatin to the nuclear rim restricts cohesin loop extrusion, focal-tethering of CBS does not disrupt global cohesin processivity. Instead, CBS anchorage enhances the formation of stable structural loops, potentially by either facilitating the engagement of distal anchors or by stabilizing cohesin/CTCF interactions.

Polymer simulation confirms that chromatin nuclear periphery tethering modulates cohesin loop extrusion.

To gain deeper insights into the influence of chromatin peripheral sequestration on cohesin-mediated loop extrusion, we performed polymer simulations on both bulk- and focal CBS-based chromatin tethering. The model utilized a 500-bead polymer partitioned into seven interspersed A- and B-type compartments with scattered CBS (Fig. 7a, b). The NE was simulated as a 2D plane containing randomly distributed chromatin anchors with adjustable affinity for B-type compartments or CBS (Fig. 7a). Our simulation established that under a fixed density, increasing the affinity of anchors to B-type compartments led to a progressively tighter association of chromatin with the NE (Fig. 7c). Remarkably, this peripheral anchorage led to a dramatic

shortening of cohesin-mediated contacts and a reduction in CTCF loops, suggesting restricted cohesin extrusion potential (Fig. 7d-f). Of note, this effect is positively scaled with anchor/chromatin affinity (Fig. 7d-f). Similarly, at a fixed affinity, increasing the density of anchors also progressively restricted cohesin extrusion capacity (Fig. 7g-j).

To complement our experimental observations of focal CBS tethering, we simulated a configuration where bulk chromatin affinity to the anchors was abolished, restricting attractions exclusively to CBS (Extended Data Fig. 16a, b). Utilizing a peak affinity of 5.0 across varying densities (n=16, 100, 625) and lateral mobility states of anchors (Extended Data Fig. 16c), we observed that focal CBS tethering did not induce short-range cohesin contact accumulation, consistent with our micro-HiChIP data (Extended Data Fig. 16d; 15h, i). Notably, tethering CBS to stationary anchors dramatically suppressed CTCF loop formation, particularly at high densities, a result that contradicts our experimental evidence of loop strengthening (Extended Data Fig. 16e, f, h, i). This inhibition is physically consistent with a model where fixed anchors generate massive tension that antagonizes cohesin-mediated extrusion, effectively stalling the motor before loop completion. In contrast, tethering of CBS to mobile anchors at low density (n=16) significantly strengthened CTCF loops, compared to the non-tethered controls (Extended Data Fig. 16e-g). This result is consistent with our experimental finding that focal tethering of CBS to the nuclear periphery via ABA treatment markedly improves structural loop strength (Fig. 6f-k). Increasing lateral anchor mobility did not dramatically change the magnitude of loop enhancement (Extended Data Fig. 16e-g). Interestingly, we found that increasing the anchor density progressively diminished this gain in loop strength (Extended Data Fig. 16e-i). We speculate that a higher density of anchors creates a "jammed" 2D surface, where steric hindrance between neighboring anchors counteracts their lateral displacement. This condition mimicks a stationary state, increasing spatial resistance and preventing cohesin from establishing stable architectural loops. Therefore, our observation of strengthened loops in the ABA-based nuclear lamina tethering system suggests that these synthetic anchors (PYL1-GFP-Lamin A) are not entirely stationary and operate in a regime where they are not exceedingly crowded so as to impede CBS engagement.

In summary, our polymer simulations not only recapitulated our experimental findings but also provide a quantitative foundation for the universal NE-mechanical tethering framework. By

528 demonstrating that the NE regulates 3D genome architecture through tethering-mode-specific
529 effects, where bulk tethering restricts cohesin processivity while focal CBS-tethering facilitates
530 loop stabilization, we establish the nuclear periphery as a general mechanical governor of the
531 genome. The coordinated action between nuclear periphery sequestration and cohesin loop
532 extrusion thus regulates the reconfiguration of chromatin architecture after mitosis.
533
534 **Discussion**
535 It is well established that many NE-associating factors mediate heterochromatin tethering at the
536 nuclear periphery [11,32,48]. Yet, whether the spatial arrangement of heterochromatin directly
537 influences 3D genome architecture remains unclear. In this study, we adopted the mitosis-to-G1
538 phase transition as a unique framework to interrogate the roles of Lamin A/C and LBR, two key
539 factors involved in heterochromatin positioning, in chromatin structural regulation.
540
541 The transition from mitosis to G1 phase provides a powerful tool for dissecting the intricate
542 mechanisms that shape 3D genome structure, offering several advantages over the canonical
543 asynchronous system. First, it provides precise control of the cell cycle. In asynchronous cells,
544 deleting a target protein may inadvertently affect cell cycle distribution, thereby complicating data
545 interpretation. The synchronized post-mitotic system eliminates this confounding factor, ensuring
546 that observed chromatin architectural changes are directly caused by protein loss, rather than a cell
547 cycle shift. Second, it enables us to observe chromatin structural reconstruction *de novo*, thereby
548 allowing us to distinguish the establishment of genome folding patterns from their maintenance.
549 Third, by integrating the post-mitotic, time-resolved Hi-C data with the dynamic binding profile
550 of LBR, we decoupled its chromatin association from its functional impact, demonstrating that
551 protein binding does not necessarily confer a regulatory function. Importantly, this temporal
552 disconnection clarifies whether LBR directly modulates genome folding or acts through a
553 secondary mechanism involving intermediate rate-limiting factors. These advantages highlight the
554 utility of the post-mitotic system for rigorous assessment of specific factors in genome folding and
555 other dynamic biological processes.
556
557 While Lamin A/C and LBR both facilitate the peripheral recruitment of heterochromatin, their
558 respective depletion reveals highly divergent impacts in post-mitotic genome refolding. Unlike the

559 negligible impact of Lamin A/C loss, likely a consequence of its weak chromatin association in
560 our cells, LBR deficiency profoundly disrupts chromatin architecture, manifesting in enhanced
561 LAD self-association alongside an attenuation of intra-loop contacts within LAD-resident loops.
562 To identify the primary mechanism through which LBR regulates post-mitotic genome
563 architecture, we considered two major forces known to shape the 3D genome: affinity-based
564 heterochromatin self-attraction and cohesin-mediated loop extrusion.
565
566 In contrast, we found that cohesin-mediated loop extrusion serves as the primary intermediate
567 mechanism through which LBR modulates genome architecture. We established this functional
568 link through several lines of evidence. First, while LBR engages chromatin early after mitosis, the
569 resulting structural perturbations only emerged in late-G1, temporally aligning with the
570 progressive loading of cohesin [35]. Second, the gain in LAD self-association observed upon LBR
571 depletion is concordant with our previous observations of strengthened B-B compartmentalization
572 in condensin-null mitotic cells loaded with extrusive-cohesin [38]. Third, deleting the cohesin
573 loader Nipbl effectively attenuated the impact of LBR loss on post-mitotic genome folding,
574 providing definitive evidence that LBR-loss-induced architectural aberrations are cohesin-
575 dependent. Finally, selective mapping of cohesin-mediated contacts via Rad21 micro-
576 HiChIP demonstrated that cohesin processivity is extended in LBR-deficient cells. Together, these
577 findings identify the modulation of the cohesin machinery as the primary pathway through which
578 LBR shapes the post-mitotic genome.
579
580 Given that heterochromatic B-type compartments extensively overlap with LADs, it is natural to
581 conceive that LBR might regulate 3D architecture by modulating affinity-based heterochromatin
582 self-aggregation. However, our H3K9me3 micro-HiChIP experiments demonstrated that these
583 homotypic interactions remain largely intact upon LBR depletion, suggesting that the spatial
584 arrangement of the genome by LBR targets loop extrusion rather than affinity-based
585 compartmentalization. Nevertheless, additional work is required to further dissect how the LBR
586 might differentially influence these two organizational forces
587
588 Rescue experiments using LBR truncation mutants confirmed that the transmembrane domain is
589 indispensable for regulating intra-loop contacts, underscoring the critical role of nuclear periphery

localization in modulating 3D genome folding. This spatial requirement, combined with recent evidence that cohesin-mediated long-range interactions can mechanically detach CTCF binding sites from the nuclear lamina [56], suggests a model of reciprocal mechanical interplay. We propose a "tension model" in which chromatin-NE interactions, such as those mediated by LBR, impose a counteractive physical tension that antagonizes the cohesin motor's pulling force, thereby restricting its loop extrusion capacity. Using an ABI-PYL1-based inducible dimerization system, we demonstrated that tethering bulk chromatin to the nuclear lamina is sufficient to recapitulate signs of restricted loop extrusion, including the enrichment of short-range extrusion intermediates and a global reduction of chromatin loops. Interestingly, focal tethering of CBS to the periphery did not inhibit cohesin extrusion processivity but rather enhanced its loop-forming capacity, implying that the specific mode of attachment governs the impact of NE on cohesin extrusion machinery.

Crucially, our tethering strategy allows us to decouple the physical act of anchoring from specific biochemical signaling. In this system, we used Lamin A as the nuclear peripheral bait. Given that Lamin A loss itself exerts no baseline impact on 3D genome architecture, the resulting impacts on cohesin extrusion can be interpreted as a purely biophysically mediated.

Our polymer simulations provide a mechanistic foundation for this biophysical interaction and explain the divergent outcomes of bulk versus focal tethering. In the case of bulk chromatin tethering, our model suggests that increased anchor density and affinity more effectively "zipped" the B-compartment to the periphery. This widespread attachment may impose a counteractive mechanical tension that transmits along the chromatin fiber, thereby preventing cohesin from sustaining loop extrusion. On the other hand, the strengthening of CTCF-anchored loops upon the peripheral tethering of CBS potentially arises from a reduction in the entropic cost required to bring distal CBS into proximity. By constraining CBS to a 2D interface, the system facilitates a "sliding" trajectory that bypasses the stochastic spatial hindrance inherent in 3D nucleoplasmic extrusion. This facilitation, however, is conditional upon anchor compliance. While mobile anchors yield to cohesin-generated tension to facilitate loop completion, stationary or "jammed" high-density anchors create a rigid boundary that stalls extrusion. Given the complexity of effects that depend on different physical parameters, it is reasonable to deduce that different

NE-associating factors, which display diverse densities, mobilities, and affinities for chromatin, may exert distinct influences on loop extrusion; for example, LBR likely functions as a high-affinity, anchor that imposes a robust mechanical brake on cohesin processivity, whereas Lamin A/C may lack the necessary affinity to exert a similar baseline constraint. Further studies are required to determine how other NE-associating factors, such as Lamin B1, SUN1, or Emerin, integrate these distinct mechanical signals to regulate cohesin loop extrusion and sculpt the 3D genome.

In summary, leveraging synchronized post-mitotic cells, synthetic biology, protein-specific chromatin conformation capture and polymer simulations, we establish a universal NE-mechanical tethering framework, in which NE-associating proteins like LBR modulate 3D genome folding by imposing mode-specific mechanical effects on cohesin loop extrusion. Hence, the spatial positioning of chromatin at the NE serves as a potent biophysical signal to tune the processivity of the extrusion machinery, thereby regulating 3D chromatin architecture.

Acknowledgements

We thank Dr. G.A. Blobel, Mr. N.G. Aboreden, Dr. M. Vermunt and members of the Zhang lab for helpful discussions. We thank Dr. Q. Peng from Shenzhen Bay Laboratory for providing C2C12 cells. We acknowledge the technical support from M. Li, Z. Huang and D. Cheng from the Flow-cytometry Core of Shenzhen Bay Laboratory. We thank S. Huang and M. Yu from the Bioimaging Core of Shenzhen Bay Laboratory for imaging support. We acknowledge computational support from the Shenzhen Bay Laboratory High Performance Computing and Informatics Core. This work was supported by the National Natural Science Foundation of China: grant no. 32521002 to H.Zhang and K.H., 82471197 to H.Zhang, 32100422 to H.Zhang, 32571445 to K.H., and 32521002 to K.H. Shenzhen Medical Research Fund: grant no. D2401002 to H. Zhang and S241101001 to K.H.

Author contributions

H.Zhang conceived the study and designed experiments. F.S., H.Zhao, E.L. performed Hi-C and CUT&Tag experiments with help from L.S., S.L., and M.W. Y.L. developed and performed micro-HiChIP experiments with help from Q.G. S.X was responsible for data analysis with help from

C.P., F.L., L.S., and Y.W. K. H. and S.Q. performed polymer simulation with help from F.L. H.Zhang wrote the manuscript with inputs from all authors.

Declaration of interests

The authors declare no competing interests.

Methods:

Cell culture.

G1E-ER4 cells and all derivative cell lines were cultured in IMDM medium supplemented with 15% FBS (v/v), 2% penicillin-streptomycin (v/v), 50ng/ml murine stem cell factor, 7.5ng/ml Epogen and 1:100000 1-Thioglycerol (v/v). Cells were maintained at a density of lower than 10^6 cells/ml. The C2C12 mouse myoblast cells were cultured in DMEM medium supplemented with 10% FBS (v/v) and 2% penicillin-streptomycin. All cell lines were periodically tested to be negative for mycoplasma. All cell lines were cultured in a humidified incubator at 37°C, with 5% CO_2.

CRISPR/Cas9 mediated genome editing.

To enable rapid degradation of Lamin A/C, mAID degron was inserted at the N terminus of Lamin A/C proteins. Note that this tag must be inserted at the N terminus to allow simultaneous degradation of both Lamin A and Lamin C proteins and avoid interrupting the farnesylation process of Lamin A. The repair template containing mCherry-mAID tag was designed as below: (1) a ~800bp fragment covering the 5' UTR of *Lmna* gene before start codon was PCR amplified from mouse genomic DNA as the left homology arm; (2) a ~800bp fragment after the start codon of *Lmna* gene was PCR amplified from the mouse genomic DNA as the right homology arm; (3) an insert fragment containing mCherry fluorescent protein and mAID degron was amplified and assembled together with the left and right homology arms into pcDNA3.1 plasmids using Gibson assembly. A sgRNA targeting the start codon region of the *Lmna* gene was designed using the Benchling online tool and cloned into the px458 plasmid. To enable genome editing, we electroporated 5million G1E-ER4 parental cells with 18μg of repair template and 18μg of the sgRNA containing px458 plasmids. Electroporation was performed with an Amaxa 2b nucleofector using the program G16. 24h after electroporation, single cells with high mCherry

683 signals were sorted into 96 well round-bottom plates. 7-10 days later, single cell clones were
684 subject to genome typing using PCR primers flanking the homology arms. Homozygous knock-in
685 clones were expanded for further experiments.
686
687 The *Lmna*^{mAID}/*Lbr*^{dTag} cells were generated based on *Lmna*^{mAID} cells using similar strategies. In
688 detail, the repair template targeting *Lbr* locus was generated as follows: (1) a ~800bp fragment
689 covering the 5' UTR of *Lbr* gene before start codon was PCR amplified from mouse genomic
690 DNA as the left homology arm; (2) a ~800bp fragment after the start codon was PCR amplified as
691 the right homology arm; (3) the insertion fragment consists of a GFP fluorescent protein and dTag
692 degron linked by a P2A sequence. The insertion fragment and two homology arms were assembled
693 together into pcDNA3.1 plasmid. A sgRNA targeting the start codon region of the *Lbr* gene was
694 designed using the Benchling online tool and cloned into the pLenti-CRISPR-BFP plasmids.
695 Electroporation was performed as above described.
696
697 The CTCF-ABI^{Halo} cells were generated using similar strategies. In detail, the repair template
698 targeting *Ctcf* locus was generated as follows: (1) a ~800bp fragment covering the 5'UTR of *Ctcf*
699 before and after stop codon was amplified from the mouse genome as left and right homology
700 arms. (2) a SV40 NLS sequence followed by a HaloTag and ABI dimerization module were
701 inserted between homology arms. Repair template and pLenti-CRISPR-BFP plasmid containing a
702 sgRNA was electroporated into parental G1E-ER4 cells as above described.
703
704 To deplete LBR in the *Nipbl*^{mAID}/*Wapl*^{dTag} cell line or C2C12 cells, we designed two sgRNAs
705 targeting exon2 of the *Lbr* gene. sgRNAs was cloned into px458 plasmid and delivered into target
706 cells using electroporation as described above. Positively transfected cells were single cell sorted
707 into 96 well plates. Single cell clones were then subject to genotyping. LBR knockout was
708 confirmed through immunofluorescence staining.
709
710 Oligos used in genome editing and genotyping are listed in Supplementary Table 3
711
712 **Retroviral infection of murine cells**

OsTIR2 was delivered into *Lmna*^{mAID} and *Lmna*^{mAID}/*Lbr*^{dTag} cells through retroviral infection as previously described. Briefly, 15μg of the MigR1-OsTIR2-TagBFP plasmid and 15μg of pCL-Eco packaging plasmid were co-transfected into HEK293T cells using PEI (Cat#23966, Polysciences). Virus-containing medium was respectively collected at 48 and 72 hours after transfection and filtered through a 0.45μm filter to remove cell debris. For retroviral infection, 3 million cells were seeded per well into a 6-well plate with 1ml of culture medium. Then, 1ml of virus containing medium was applied into each well together with 8mg/ml (final concentration) polybrene and 10mM HEPES buffer (Gibco, Cat#15630-106). The plate was sealed with parafilm and spun at 3000 rpm for 1.5 hours at room temperature. After spin infection, cells were washed with PBS and re-suspended in fresh medium. 48 hours after infection, cells expressing TagBFP were sorted using a BD FACS AriaIII cell sorter. The same strategy was adopted to deliver retroviruses encoding H2B-ABI^{Halo} or Lamin A-PYL1^{GFP} into target cells (*Nipbl*^{mAID}/*Wapl*^{dTag}/*Lbr* $^{-/-}$ or CTCF-ABI^{Halo}). 48 hours after infection, cells expressing H2B-ABI^{Halo} and/or Lamin A-PYL1^{GFP} were collected using a BD FACS AriaIII cell sorter.

Cell growth curve

To examine the influence of Lamin A/C depletion on cell growth, Lamin A/C^{mAID} cells expressing OsTiR2 were seeded into untreated non-adhesive 6-well plates at a density of ~1-5×10^4/ml. Cells were treated with or without 5-Ph-IAA (1μM). Cell density of each condition was counted every 24 hours for a total of 72-hour duration. Four independent biological replicates were performed across two clones. Similar strategy was adopted to assess the impact of Nipbl or/and Wapl loss in the *Nipbl*^{mAID}/*Wapl*^{dTag} cells

Immunofluorescence staining

Cells with indicated treatment were fixed with 1% formaldehyde in l×PBS for 10min at room temperature. Fixation was quenched by 1mM Glycine (BBI, cat#A502065-0500) at room temperature for 5min. Cells were then washed once with 1×PBS and resuspended in 100ul Staining buffer (0.1% Triton x-100 (Sigma-Aldrich, cat#T8787-50ML), 2mM EDTA (BBI, B540625-0500) in 1×PBS) containing diluted primary antibodies (1:100) and incubated for 3 h at room temperature or overnight at 4℃. Cells were then washed once with 1×PBS, resuspended in 100ul staining buffer containing diluted secondary antibody (1:500) and incubated at room temperature for 1h.

744 Cells were then pelleted and re-suspended in staining buffer containing DAPI (4ug/ml, Roche
745 cat#10236276001) and seeded into glass bottom 384-well plates. Images were obtained using an
746 Olympus Spin SR spinning disc confocal microscope. Fluorescence intensity was quantified in
747 ImageJ by selecting target nuclei (⩾40 per condition) with the polygon tool to measure mean
748 fluorescence intensity values. Background signals from blank regions were also recorded for
749 background subtraction.
750
751 **Nocodazole mediated prometaphase arrest/release and protein degradation**
752 For parent G1E-ER4 cells.
753 Asynchronously growing cells were synchronized with prometaphase through nocodazole
754 treatment (200ng/ml) for 8 hours at a density of 0.5million/ml. To obtain post-mitotic cells at
755 defined time points, nocodazole synchronized cells were pelleted at 1200rpm for 3min. Cells were
756 washed twice with PBS and then immediately re-suspended in fresh warm medium free of
757 nocodazole. Cells were harvested at 45 minutes, 1 hour, 2 hours or 4 hours after release into G1
758 phase.
759
760 For *Lmna*^{mAID} cells.
761 The exact same procedure of nocodazole mediated arrest release was applied to this cell line. To
762 degrade Lamin A/C during mitosis, 5-Ph-IAA (1μM) was added into the culture for 4 hours before
763 nocodazole release. Nocodazole release was performed in 5-Ph-IAA containing medium for 1 hour,
764 2 hours, 4 hours or 6 hours respectively. Control cells treated without 5-Ph-IAA treatment were
765 processed in parallel.
766
767 For *Lmna*^{mAID}/*Lbr*^{dTag} cells.
768 The exact same procedure of nocodazole mediated arrest release was applied to this cell line. To
769 completely degrade LBR, dTag13 (1μM) was added into the culture for 4 hours before nocodazole
770 release. Cells with or without 5-Ph-IAA treatment were both collected. To assess the impact of
771 residual LBR signals in the *Lmna*^{mAID}/*Lbr*^{dTag} cells, a similar strategy was implemented but without
772 dTag13 treatment.
773
774 For *Nipbl*^{mAID}/*Wapl*^{dTag} cells.

The exact same procedure of nocodazole mediated arrest release was applied to this cell line. To deplete Nipbl or Wapl, cells were treated with 5-Ph-IAA or dTag13 for 4 hours before nocodazole release. Late-G1 phase cells were then harvested at 6h after nocodazole release. Cells without any treatment were processed in parallel as control.

Artificial tethering of chromatin to the nuclear periphery.

To tether chromatin to the nuclear lamina H2B-ABI^{Halo}/Lamin A-PYL1^{GFP} and CTCF-ABI^{Halo}/Lamin A-PYL1GFP cells were treated with 1.3mM and 2.5mM ABA, respectively for 24 hours. DMSO was treated in parallel as controls. Peripheral enrichment of H2B or CTCF was visualized by staining the cells with JFX650 fluorescent ligand (Promega HT107A) using an Olympus Spin SR spinning disc confocal microscope.

Cleavage Under Targets and Tagmentation (CUT&Tag)

G1E-ER4 cells expressing mCherry tagged murine cyclin B1 mitotic degron (mCherry-MD) were arrested to prometaphase through nocodazole treatment for 8 h. Cells were harvested at 45 min, 1h, 2h or 4h after nocodazole release. Cells were fixed with 95% pre-cooled methanol for 15 min at -20℃. After fixation, cells were pelleted and resuspended in 1 mL 1× PBS buffer (fresh supplemented with 1:500 protease inhibitors and 1:100 PMSF) containing 1 μL Hoechst 33342 (10 mg/mL). Cells were purified for G1 phase cells via FACS based on Hoechst 33342 and mCherry signals. Following sorting, CUT&Tag was then performed using an Hieff NGS® G-Type In-Situ DNA Binding Profiling Library Prep Kit for Illumina® (Yeasen, 12598). In brief, Con A magnetic beads were used to capture cells and 5% Digitonin was utilized to perforate the cell membrane. The target protein was detected using 5μl of primary antibody (Lamin A/C (Abcam, ab238303), Lamin B1 (Abcam, ab16048) or Lamin B Receptor (Abcam, ab232731)), followed by incubation with the secondary antibody (Goat Anti-Rabbit IgG H&L (Abcam, ab150079) or Goat Anti-Mouse IgG H&L (Abcam, ab150115)) and Protein A/G-Tn5. The targeted DNA sequence bound by the target protein was sheared by the transposase and PCR amplification was then performed to obtain the DNA library. CUT&Tag libraries were sequenced on the Illumina Novaseq 6000 sequencing platform.

***In-situ* Hi-C**

In-situ Hi-C was performed as previously described [35-38]. In brief, cells were initially fixed with 2% formaldehyde for 10 minutes at room temperature and subsequently permeabilized with 0.1% Triton X-100. To enrich for cells in the G1 phase, samples were purified based on their DAPI signal (2N) using FACS. The purified cells (2×10^5) were then subjected to a low-input Hi-C protocol. This involved cell lysis, isolation of nuclei, and treatment with SDS before restriction digestion. Chromatin was digested overnight with 25U DpnII, followed by a second enzyme addition (25U). The sticky ends generated were blunted using Klenow fragment in the presence of biotinylated dATP. Proximity ligation was then performed using 2000U T4 DNA ligase. Following ligation, crosslinking was reversed in the presence of 1% SDS and proteinase K at 65°C for 12 hours, and DNA was purified using phenol-chloroform extraction. The purified DNA was then sheared to a fragment size of 200-300bp using sonication. Biotinylated DNA fragments, representing the ligation junctions, were enriched using streptavidin-coated beads. Library construction, including end repair, dA-tailing, and adaptor ligation, was carried out on the beads using the VAHTS Universal DNA Library Prep Kit. The libraries were then eluted, purified, and PCR amplified for 8-9 cycles using the VAHTS® HiFi Amplification Mix. Finally, the amplified libraries were sequenced on an MGI DNBSEQ-T7 platform.

Micro-HiChIP

Micro-HiChIP was optimized based on the a previous micro-C-ChIP method described by Metelova et al [53]. Briefly, 10-20 million cells were harvested and resuspended in 9ml PBS. The first crosslinking was initiated by adding 37% formaldehyde to a final concentration of 1% and incubating on a roller mixer at room temperature (RT) for exactly 10min. The reaction was quenched by adding cold 2M glycine to a final concentration of 0.25M and mixing for 5min at room temperature. Cells were washed once with 10ml ice-cold PBS and subsequently resuspended in 3mM EGS (MCE, HY-130458) in 1×PBS at a density of 1million cells/ml. A second crosslinking was performed for 40min at RT and quenched by adding cold 2M glycine to a final concentration of 0.4M, followed by incubation for 10min at RT. Cells were washed once with 1× PBS containing 0.5% BSA. Pelleted samples were either processed immediately or snap-frozen and stored at -80℃.

Double-crosslinked samples were divided into 5 million cell aliquots for parallel processing. Cells were lysed in 1ml ice-cold cell lysis buffer (10mM Tris-HCl pH 8.0, 10mM NaCl, 0.2% NP-40/Igepal) supplemented with 1×protease inhibitor cocktail (Yeasen, 20135ES03) for 20min on ice. After centrifugation, chromatin was digested with 35U MNase (NEB, M0247S) in 400μl MNase reaction buffer (50mM Tris-HCl pH 8, 0.1mM $CaCl_2$) at 37℃ for exactly 30min with shaking (850rpm). Digestion was terminated by adding 500mM EGTA to a final concentration of 5mM, followed by incubation at 65℃ for 10min. Nuclei were washed once with 0.2ml ice-cold complete MB#2 buffer (50mM NaCl, 50mM Tris-HCl pH 7.5, 10mM $MgCl_2$, 100μg/mL BSA). End-blunting and proximity ligation were carried out in a single reaction by incubating the digested chromatin with 0.1mM dTTP (Diamond, BN10057-0002), 0.1mM dGTP (Diamond, BN10057-0004), biotin-14-dATP (Active Motif, 14139), biotin-11-dCTP (MCE, HY-D1668), 1×T4 ligase buffer , 2.5mM EGTA, 10U Klenow fragment (NEB, M0210L), 60U T4 DNA ligase (Thermo, EL0013), and 20U T4 PNK (NEB, M0201L). The mixture was incubated at 37℃ for 2h with shaking (850 rpm), followed by an overnight incubation at 16℃ (200 rpm). To remove biotin from unligated chromatin ends, proximity-ligated chromatin was resuspended in 200μl 1×NEBuffer 1 (NEB, B7001S) with 200U Exonuclease III (NEB, M0206L) and incubated at 37℃ for 15min. Nuclei were subsequently lysed in 200μl nuclei lysis buffer (50 mM Tris-HCl pH 8.0, 10mM EDTA, 1% SDS, 1×protease inhibitor cocktail) and fragmented using a Qsonica Q800R3 sonicator (80% amplitude, 20s ON/40s OFF, 5 min total on time).

The supernatant was diluted 1:4 with IP dilution buffer (1% Triton X-100, 20mM Tris-HCl pH 8.0, 2mM EDTA, 150mM NaCl, 0.01% SDS, 1 × protease inhibitor cocktail). Immunoprecipitation was performed by incubating the diluted chromatin with antibodies (Abcam ab992 for Rad21 and Abcam ab8898 for H3K9me3) overnight at 4℃ with rotation. Antibody-chromatin complexes were captured by adding 30μl pretreated Protein A/G magnetic beads (Vazyme, PB101) and rotating for 4h at 4℃. Beads with antibody-chromatin complex were sequentially washed twice with IP Wash Buffer 1 (20mM Tris-HCl pH 8.0, 50mM NaCl, 2mM EDTA, 1% Triton X-100, 0.1% SDS), twice with High-Salt Buffer (20mM Tris-HCl pH 8.0, 500mM NaCl, 2mM EDTA, 1% Triton X-100, 0.01% SDS), once with IP Wash Buffer 2 (10mM Tris-HCl pH 8.0, 250mM LiCl, 1% Igepal, 1% sodium deoxycholate, 1mM EDTA), and twice

with 1×TE buffer (10mM Tris-HCl pH 8.0, 1mM EDTA). Chromatin was eluted and reverse-crosslinked by incubating beads in 200µl elution buffer (20mM Tris-HCl pH 8.0, 10mM EDTA, 5mM EGTA, 300mM NaCl, 1% SDS, 300µg/mL Proteinase K) overnight at 65℃. DNA was purified using the ChIP DNA Clean & Concentrator kit (Zymo, D5201) and eluted in 140µL TE buffer.

DNA end repair, dA-tailing and adaptor ligation were constructed on beads, using the VAHTS Universal DNA Library Prep Kit for Illumina or MGI (Vazyme, ND610-02/ NDM607-02) based on the manufacturer's protocol. Libraries were amplified for 9–15 cycles using VAHTS HiFi Amplification Mix, purified with VAHTS DNA clean beads (Vazyme, N411), and sequenced on an MGI DNBSEQ-T7 platform.

LBR rescue experiments.

The full-length LBR (T0) coding sequence was amplified from the cDNA library of parental G1E-ER4 cells. A HaloTag protein and 5×Flag tags were fused to the C terminus of full-length LBR. Coding sequence of the fusion protein was then cloned into the MigR1 retroviral vector. Virus production and transduction into the *Lmna*^{mAID}/*Lbr*^{dTag} cells were carried out as above mentioned. 48 hours later, the infected cells were stained with Janelia Fluor® 646 HaloTag® Ligand (Promega, Cat#GA112A) for 25min. Positively stained cells were then sorted using a BD FACS AriaIII cell sorter and further expanded for Hi-C experiments. Truncation LBR mutants were assembled by various combinations of its three domains: the Tudor&RS domain (1-89a.a.), the secondary globular domain (90-211a.a.), and the transmembrane domain (212-616a.a.). Six different truncation mutants were generated: Tudor&RS-halo-tag-5×Flag (T1), Globular II-halo-tag-5×Flag (T2), Transmembrane-halo-tag-5×Flag (T3), Tudor&RS-globular II-halo-tag-5×Flag (T4), Tudor&RS-transmembrane-halo-tag-5×Flag (T5), and Transmembrane-globular II-halo-tag-5×Flag (T6). Virus packaging, transduction and purification of positively infected cells were performed as described above.

ChIP-seq

To define structural loops in C2C12 cells, we performed chromatin immunoprecipitation and sequencing (ChIP-seq) using antibodies against CTCF (Millipore Cat#07-729, 7.5µl/IP), Rad21

(Abcam Cat#ab992, 5µl/IP) and H3K27ac (Abcam Cat#ab4729, 3µl/IP). Briefly, 5-10 million cells were crosslinked with 1% formaldehyde for 10min at room temperature. Crosslinking was then quenched by glycine (final concentration 1M) for 5min at room temperature. Cells were then pelleted and re-suspended in 1ml cold Cell Lysis Buffer (10mM Tris pH 8, 10mM NaCl and 0.2% NP-40, 1:500 protease inhibitor and 1:100 PMSF) and incubated on ice for 20min. Nuclei were pelleted and re-suspended in 1ml Nuclear Lysis Buffer (50mM Tris pH 8, 10mM EDTA, 1% SDS containing 1:1000 protease inhibtor and 1:100 PMSF) and incubated on ice for 20min. Chromatin was fragmented by sonication using a Qsonica Q800R3 sonicator (80% amplitude, 20s ON, 40s OFF) for 17min. Chromatin was centrifuged at 15000g for 10min at 4℃ for 10min to remove cell debris. Chromatin was diluted with 4 volumes of IP dilution buffer (20mM Tris pH 8.0, 2mM EDTA, 150mM NaCl, 1% Triton X-100, 0.01% SDS, 1:1000 protease inhibitor and 1:100 PMSF). 50µl of protein A/G agarose beads (Santa Cruz Cat#sc-2003) were added into the mixture for 4-8h at 4℃ to preclear the chromatin. Precleared chromatin was mixed with 35µl protein A/G agarose beads pre-bound with antibody and incubated on a rotator at 4℃ overnight. Chromatin bound beads were washed once with IP wash buffer I (20mM Tris pH 8, 2mM EDTA, 50mMNaCl, 1% Triton X-100, 0.1% SDS), twice with high salt buffer (20mMTris pH 8, 2mM EDTA, 500mMNaCl, 1% Triton X-100, 0.01% SDS), once with IP wash buffer II (10mMTris pH 8, 1mM EDTA, 0.25 M LiCl, 1% NP-40/Igepal, 1% sodium deoxycholate) and twice with TE buffer (10mM Tris pH 8, 1mM EDTA pH 8). Chromatin was then eluted in 200µl fresh Elution Buffer (100mM NaHCO3, 1%SDS). Reverse crosslinking was performed at 65℃ overnight in the presence of proteinase K. DNA was purified using the PCR purification kit (QIAGEN Cat#28106). ChIP-seq libraries were constructed using the VAHTS Universal DNA Library Prep Kit for MGI (Vazyme, Cat#NDM610-02) according to the manufacture's protocol. ChIP libraries were sequenced on the MGI DNBSEQ-T7 sequencing platform.

To assess CTCF binding before and after nuclear periphery tethering, we performed ChIP-seq on DMSO or ABA treated CTCF-ABI^{Halo}/Lamin A-PYL1^{GFP} cells, using antibody against CTCF (Millipore Cat#07-729, 10µl/IP). The exact same protocol was carried out except that cells were subject to 1% formaldehyde and 3mM EGS double crosslinking as was done for micro-HiChIP experiments. 5% 293T cells were added into each condition as spike-in controls.

927

928 **Transient transcriptome sequencing (TT-seq).** TT-seq was performed as described (Schwalb et
929 al, 2016) with minor changes. Briefly, cells were metabolically labeled with 500 μM 4-thiouridine
930 (4sU, MCE, HY-W011793) for 10 minutes to incorporate the uridine analog into newly
931 synthesized nascent RNA. After 10min, culture medium was promptly removed and total RNA
932 was extracted using TRIzol reagent (Thermo Fisher Scientific, 15596026CN). Fragmented RNA
933 was incubated with EZ-Link Biotin-HPDP (Thermo Fisher Scientific, A35390) in dark for 2 hours
934 with rotation. RNA was then purified through pheno-chloroform purification and dissolved in
935 nuclease free water. Biotinylated RNA was denatured at 65°C for 10 minutes and incubated
936 with Dynabeads MyOne Streptavidin C1 beads (ThermoFisher Scientific, 65002) for 30 min in
937 dark at room temperature. Subsequently, beads were washed four times with 1× binding and wash
938 buffer (2× Bind and Wash (B&W) buffer: 200mM Tris-HCl pH 7.5, 2M NaCl, 20mM EDTA,
939 0.1%(v/v) Tween20 in DEPC-Treated water) to remove unspecific binding. To elute 4sU labeled
940 RNA, beads were re-suspended in 50μl 1× binding and wash buffer containing 100mM DL-
941 dithiothreitol (DTT) (Sigma Aldrich, D0632) and incubated at room temperature in dark for 15min.
942 RNA was precipitated by adding 10 μL of 3M Sodium Acetate (pH 5.5), 2 μL of 15 mg/mL
943 GlycoBlue co-precipitant (ThermoFisher Scientific, AM9515) and an equal volume of isopropanol,
944 followed by mixing and incubation at room temperature for 5 minutes. The RNA pellet was washed
945 with 1 mL of 80% ethanol and resuspended in DEPC-treated water. For library preparation, 100
946 ng of labeled RNA were used as input for strand-specific library preparation using the Vazyme
947 Universal V8 RNA-seq Library Prep Kit for MGI. Double-stranded cDNA was synthesized,
948 followed by RNA adapter ligation, purification, and amplification with 2×HF Amplification Mix.
949 All samples were sequenced on the MGI DNBSEQ-T7 platform.

950

951 **Quantification and data analysis.**

952 **ChIP-seq and CUT&Tag data processing.** ChIP-seq and CUT&Tag data were processed in a
953 similar pipeline as follows. Briefly, ChIP-seq paired-end reads were aligned to mouse reference
954 genome mm9 through the Bowtie2 (v2.3.5.1) software with default parameters, while CUT&Tag
955 adopted stricter parameters setting as '--very-sensitive -I 10 -X 700'. All unmapped reads and low-
956 quality alignments with MAPQ score lower than 30 were removed using SAMtools (v1.9). PCR
957 duplicates were removed using Picard (v2.23.3) with default parameters. The de-duplicated data

was then converted into bed file format to remove the reads aligned to mitochondria, random contigs and blacklisted regions using BEDtools (v2.27.1). Finally, the bed files were reconverted into bam files and were mapped to the genome using bamcoverage from deeptools(v3.1.3), with normalization method set to CPM.

For spike-in normalization of CTCF ChIP-seq in CTCF-ABI^{Halo}/Lamin A-PYL1^{GFP} cells, raw reads were sequentially aligned to human (hg19) and mouse (mm9) genomes using Bowtie2 (v2.3.5.1) with default parameters. The resulting alignments were filtered to retain only high-quality reads (MAPQ > 30), and PCR duplicates were removed using Picard (v2.23.3). A scaling factor was calculated as: 2×10^6/hg19_counts. Unique reads aligned to mouse genome was then normalized using the above scaling factor by Deeptools (v3.1.3).

Peak calling. CTCF, Rad21 and H3K27ac ChIP-seq experiments were performed on C2C12 cells. Peak calling for were performed using MACS2 (v2.2.7.1) with default parameters. Q-value cutoffs of 10^{-7}, 10^{-7} and 0.05 were used to call peaks for CTCF, Rad21 and H3K27ac respectively.

Identification and partition of LADs. To identify LADs, we segmented the genome into 25kb bins. For each genomic bin, we calculated the corresponding CUT&Tag signal intensity of Lamin A/C, LBR and Lamin B1 using the UCSC toolkit (BigWigAverageOverBed). For each genomic bin, three Z-scores corresponding to Lamin A/C, LBR and Lamin B1 respectively were computed across the entire genome and all tested time points. We noticed that LBR CUT&Tag experiments displayed the stronger signal noise ratio than that of Lamin B1 and Lamin A/C. Hence, we decided to define LADs using LBR CUT&Tag results. LAD identification was performed as below: (1) 25kb genomic bins with >0 LBR Z-score at any tested time point were selected. (2) Consecutive bins with a gap distance <50kb were merged together to generate LADs. (3) LADs smaller than 50kb were removed from the final list. In this way, we identified 1022 LADs genome wide. To gain deeper insights into the dynamic LAD reformation, we performed unsupervised *k-means* clustering on LBR and Lamin B1. We identified three LAD clusters with distinct reformation kinetics. Cluster1 LADs displayed high levels of LBR, Lamin B1 and Lamin A/C and were resumed rapidly after mitosis. Cluster2 LADs displayed delayed reformation dynamics for LBR

and Lamin B1 and were not enriched with Lamin A/C. Cluster3 LADs display LBR and Lamin B1 signal at early time points which progressively diminished as cells enter G1.

Hi-C and micro-HiChIP data preprocessing. *In-situ* Hi-C from all samples were processed through HiC-Pro(v3.0.0) workflow. Reads were aligned to the mouse reference genome mm9 using the bowite2(v2.3.5.1) software (global parameters: --very-sensitive -L 30 --score-min L, -0.6, -0.2 --end-to-end –reorder; local parameters: --very-sensitive -L 20 --score-min L, -0.6, -0.2 --end-to-end --reorder). The output SAM files were subsequently sorted and mapped to the bed files labeled with corresponding restriction sites to get the hic fragments. Finally, the fragments were merged into valid interaction pairs as output. Micro-HiChIP data were processed using the Microcket software (v.1.4) with default parameters [57]. Raw contact maps were used for all downstream analysis without balancing.

We then converted the output pair files into ".hic" files using juicertools (v1.9.9 or 1.19.02) [58]. HiC files were also converted to ".cool" files with different resolutions using the Hicexplorer (v3.7) [59]. Unless otherwise indicated, all contact maps, saddle plots, compiled plots (such as APA plots) are merged plots of all corresponding clones or biological replicates.

Eigenvector decomposition. Eigenvector decomposition was performed on the Pearson's correlation matrix of the 25kb binned KR balanced cis-interaction maps using the "eigs-cis" function of Cooltools (v0.4.0). EV1 direction was determined based on gene density.

Saddle plots (conventional and transformed). Conventional saddle plots were generated as previously described as the basis of EV1 values. Briefly, 25kb binned KR-balanced observed over expected Hi-C contact maps were first generated for each sample using the DUMP utility of Juicer tools (v.1.13.02). To generate saddle plots, the above Hi-C contact maps of each cell type or treatment condition were transformed in a way that each row and column of 25kb bins were sorted on the basis of their corresponding late-G1 phase EV1 values in an ascending order from top to bottom and from left to right. In this way, genomic bins at the upper left corner represent B-B contacts whereas those at the lower right corner represent A-A interactions. This operation was independently performed for each chromosome. The resulting transformed maps for each

chromosome were sectioned into 200×200 pixels and averaged together to yield genome-wide saddle plots.

Saddle plots based on Lamin A/C CUT&Tag signals were generated in a similar manner as elaborated above except that each row and column of bins were re-ordered on the basis of corresponding late-G1 phase Lamin A/C CUT&Tag signal intensity. In this way, bins at the lower right corner represent self-interaction between Lamin A/C-bound regions. Bins at the upper left corner represent interactions between Lamin A/C-depleted regions. Bins at the upper right or lower left corner represents the separation between Lamin A/C-enriched and depleted regions. Note that this separation was relatively weak compared to that between A- and B-compartments, suggesting the Lamin A/C-bound regions do not efficiently segregate from the rest of the genome. Quantification of the extent of self-association among Lamin A/C-bound regions was illustrated in Figure 2e.

Contact probability decay curves (P_S curves). The P_S curves were generated using the "expected-cis" function of Cooltools (v0.4.0). Curves from individual chromosomes were averaged to generate the genome wide P_S curve.

Domain calling and partition. Domains were identified using a previously established protocol combining the "Arrowhead" domain calling algorithm and insulation score profiles. We computed insulation scores on the 10kb binned, KR balanced contact maps using the "insulation" function of Cooltools (v0.4.0). We adopted a sliding window of 12bin ✕ 12bin as previously practiced. 10kb bins passing the insulation score threshold (0.2) were selected as tentative boundaries for each sample. The exact same protocol was applied to all post-mitotic *Lmna*^{mAID} and *Lmna*^{mAID}/*Lbr*^{dTag} cells. Tentative boundaries from all samples were merged using the *merge* function of bedtools (maximal gap 50kb) to generate a non-redundant boundary list.

For domain identification, we employed the "Arrowhead" domain calling algorithm. Domains were independently called on 10kb, 25kb and 50kb binned Hi-C contact maps. To eliminate spurious domain calls, for a given sample, we compared the initial domain list (combining 10kb, 25kb and 50kb domain calls) with the above generated non-redundant boundary list. Boundaries

within a single chromosome were randomly paired up so that the distance between each boundary was larger than 50kb and smaller than 10Mb. These boundary pairs were considered as tentative domains. For a tentative domain to be considered as valid, it must overlap with at least 1 domain from the initial domain list with a wiggling size of 50kb for each boundary. The same procedure was performed for all post-mitotic samples.

To identify CTCF/cohesin mediated TADs, we examined the boundary composition of CTCF and cohesin for each domain. A TAD is defined as long as it contains both CTCF and cohesin binding sites in both boundary regions. To determine if a boundary contains CTCF or cohesin binding sites, we applied the below intersection rule. For domains smaller than 1Mb, a wiggle size of 15kb from the center of boundary was used. For domains larger than 1Mb and smaller than 2Mb, a wiggle room of 25kb was used. For domains larger than 2Mb and smaller than 3Mb, a wiggle room of 50kb was used. For domains larger than 3Mb and smaller than 4Mb, a wiggle room of 100kb was used. For domains larger than 4Mb, a wiggle room of 150kb was used.

Loop calling. Loop calling were performed on all post-mitotic *Lmna*^{mAID}, *Lmna*^{mAID}/*Lbr*^{dTag}, *Nipbl*^{mAID}/*Wapl*^{dTag} samples as well as C2C12 cells as previously described at 10kb resolution [35-38]. Merging of loops were performed within the *Lmna*^{mAID}, *Lmna*^{mAID}/*Lbr*^{dTag} cells, the *Nipbl*^{mAID}/*Wapl*^{dTag} cells and C2C12 cells respectively as previously described. For a loop to be considered as a structural loop, both of its anchors must contain CTCF and Rad21 binding sites while at most one anchor may contain cis-regulatory elements (CREs). For a loop to be classified as a CRE loop, it must contain CRE in both anchors and at most contain CTCF/Rad21 binding sites in one anchor. For chromatin tether experiments, loops were independently identified at 10kb resolution for each condition (DMSO or ABA treated) as previously described. Loops were then merged to generate a non-redundant loop list.

Stripe segmentation of structural loops. To quantify cohesin loop extrusion capacity, we analyzed the distribution of intra-loop cohesin-mediated extrusion intermediates within the Rad21 micro-HiChIP contact maps. We partitioned all structural loops previously identified by Hi-C experiments in the *Nipbl*^{mAID}/*Wapl*^{dTag} cells, into 100kb-wide stripes that are parallel to the diagonal. The maximal distance between the stripe and the diagonal was set to be 5Mb. For each

sample, we calculated the average observed/expected value within each j^{th} stripe (SI_j). To evaluate the impact of nuclear peripheral anchoring on cohesin extrusion processivity, we calculated the $\log_2$ fold change in SI_j between $Lbr^{-/-}$ and $Lbr^{+/+}$ conditions as well as between chromatin peripheral-tethered (ABA treated) vs untethered (DMSO treated) conditions for each structural loop. To identify structural loops situated within LADs, we quantified the internal LBR CUT&Tag signal for each loop anchor. Loops were classified as "LAD-resident" using an empirical threshold of 0.1, a cutoff that encompassed approximately 8.3% of all structural loops identified.

Aggregated plots for loops and domains. Aggregated plots were generated using the python package Coolpup (v0.9.7) [60].

TT-seq preprocessing and differential expression analysis. We used STAR (v2.7.10b) to align the sequencing data to the mouse reference genome mm9. The resulting BAM files were subjected to quality control and filtering with Samtools (v1.6) using the parameters "-q 10 -f 0x2" to remove low-quality alignments. PCR duplicates were then removed using the Picard tool (v2.25.5). To obtain strand-specific information, we used Samtools to extract the alignment results of the forward strand with the parameters "-f 128 -F 16" and "-f 80", and those of the reverse strand with the parameters "-f 144 -f 64" and "-F 16", respectively. The "bamCoverage" function in deepTools (v3.5.4) was used to generate bigwig files. Feature quantification was performed using the "multicov" function in bedtools (v2.31.1) to count the gene expression data on the forward and reverse strands. The expression information from both strands was combined, and finally, the DESeq2 package (v1.42.1) in R was used to perform differential expression analysis on the count data. The filtering criteria were set as fold change greater than 1.5 and adjusted *P* value (*padj*) less than 0.05 to identify significantly differentially expressed genes.

ABC model predicts enhancer-promoter interactions. We stratified the candidate elements (promoters or enhancers) associated with dysregulated genes and interrogated their potential connectivity changes upon Lamin A/C or LBR lost using the activity-by-contact (ABC) model (https://github.com/broadinstitute/ABC-Enhancer-Gene-Prediction) [61]. In brief, the region and activity of elements were estimated using both ATAC-seq and H3K27ac ChIP-seq data of

asynchronous G1E-ER4 cells. Then, we calculated the contact frequency for element-gene pairs using a 5 kb resolution Hi-C matrix from each sample. Finally, the ABC score for the influence of element E on gene G is calculated as follows: The activity of element E is multiplied by the contact frequency between E and G, and this product is subsequently divided by the sum of the products of activity and contact frequency for all candidate elements within a 5 Mb range. An elevated ABC score threshold resulted in a reduced number of interactions recognized as higher confidence. We applied an ABC score threshold of 0.025 to call reliable promoter-promoter and enhancer-promoter pairs. Pairs are considered valid as long as the ABC score meets our threshold in at least one sample. Each of these pairs was subsequently linked to differentially expressed genes.

Polymer simulation.

All polymer simulations were performed using Langevin dynamics in the NVT ensemble. The chromatin fiber was represented as a coarse-grained copolymer chain of 500 beads connected via harmonic springs. Distinct bead types corresponded to A and B compartments to capture their differential physicochemical properties. To promote compartmental phase separation, the Lennard-Jones interaction parameters between A and B beads (ϵ_{A-B}) were set significantly lower than self-interaction parameters within each compartment. The NE was modeled as a planar wall of stationary beads. Membrane anchors were represented by flexible polymers of five beads that strongly adhered to the wall, confining their diffusion to the nuclear periphery. To mimic chromatin tethering, B-type chromatin beads could form dynamic bonds with anchor beads, accompanied by a strong isotropic adsorption potential.

Loop extrusion was simulated using a custom module in LAMMPS [62]. Extruders were modeled as sliding bonds that extended loops bidirectionally along the chromatin fiber until encountering barriers. At the start of the simulation, each extruder loaded stochastically between adjacent bead pairs (i and i+2), provided the beads in the new loop were unoccupied and located within a spatial cutoff of 1.12. To reflect the experimentally observed higher enrichment of cohesins in A compartments, the loading probability was set higher for A-compartment beads (0.003) than for B-compartment beads (0.001). Following loading, extrusion attempts occurred every 3000 simulation steps, and each extruder unloaded with a probability of 0.001 per 1000 simulation steps. A key topological constraint was applied during each extrusion step. The distance between

the two chromatin beads that were targeted to become the next base of the expanding loop must be less than 2.0 for a successful extrusion. When two extruders converged at the same position, both stalled until one unloaded, allowing the other to proceed.

In addition to extruders, we incorporated CTCF proteins as directional barriers to loop expansion. Three types of CTCF barriers were defined, blocking extrusion from the left, from the right, or from both directions. In our simulations, an extruding loop had a 1% probability of bypassing a CTCF barrier. In the point-tether setup, CTCF beads (CBS) could form dynamic bonds with anchor beads, accompanied by a strong isotropic adsorption potential.

References:

1 Gruenbaum, Y. & Foisner, R. Lamins: nuclear intermediate filament proteins with fundamental functions in nuclear mechanics and genome regulation. *Annual review of biochemistry* **84**, 131-164, doi:10.1146/annurev-biochem-060614-034115 (2015).

2 Dechat, T. *et al.* Nuclear lamins: major factors in the structural organization and function of the nucleus and chromatin. *Genes & development* **22**, 832-853, doi:10.1101/gad.1652708 (2008).

3 Worman, H. J., Yuan, J., Blobel, G. & Georgatos, S. D. A lamin B receptor in the nuclear envelope. *Proceedings of the National Academy of Sciences of the United States of America* **85**, 8531-8534, doi:10.1073/pnas.85.22.8531 (1988).

4 Crisp, M. *et al.* Coupling of the nucleus and cytoplasm: role of the LINC complex. *The Journal of cell biology* **172**, 41-53, doi:10.1083/jcb.200509124 (2006).

5 Holmer, L. & Worman, H. J. Inner nuclear membrane proteins: functions and targeting. *Cell Mol Life Sci* **58**, 1741-1747, doi:10.1007/PL00000813 (2001).

6 Ye, Q. & Worman, H. J. Interaction between an integral protein of the nuclear envelope inner membrane and human chromodomain proteins homologous to Drosophila HP1. *The Journal of biological chemistry* **271**, 14653-14656, doi:10.1074/jbc.271.25.14653 (1996).

7 Wang, B. *et al.* The molecular basis of lamin-specific chromatin interactions. *Nature structural & molecular biology* **32**, 1999-2011, doi:10.1038/s41594-025-01622-5 (2025).

8 van Schaik, T., Vos, M., Peric-Hupkes, D., Hn Celie, P. & van Steensel, B. Cell cycle dynamics of lamina-associated DNA. *EMBO reports* **21**, e50636, doi:10.15252/embr.202050636 (2020).

9 Renard Lewis, V. S., Krisztian Koos, Cristiana Bersaglieri, Caroline Ashiono, Raffaella Santoro, Constance Ciaudo, Peter Horvath, Puneet Sharma, Ulrike Kutay. LBR and LAP2 mediate heterochromatin tethering to the nuclear periphery to preserve genome homeostasis. *bioRxiv*, doi:https://doi.org/10.1101/2024.12.23.628302 (2024).

10 Guelen, L. *et al.* Domain organization of human chromosomes revealed by mapping of nuclear lamina interactions. *Nature* **453**, 948-951, doi:10.1038/nature06947 (2008).

11 Briand, N. & Collas, P. Lamina-associated domains: peripheral matters and internal affairs. *Genome Biol* **21**, 85, doi:10.1186/s13059-020-02003-5 (2020).

12 van Steensel, B. & Belmont, A. S. Lamina-Associated Domains: Links with Chromosome Architecture, Heterochromatin, and Gene Repression. *Cell* **169**, 780-791, doi:10.1016/j.cell.2017.04.022 (2017).

13 Hoskins, V. E., Smith, K. & Reddy, K. L. The shifting shape of genomes: dynamics of heterochromatin interactions at the nuclear lamina. *Current opinion in genetics & development* **67**, 163-173, doi:10.1016/j.gde.2021.02.003 (2021).

14 Becker, J. S. *et al.* Genomic and Proteomic Resolution of Heterochromatin and Its Restriction of Alternate Fate Genes. *Molecular cell* **68**, 1023-1037 e1015, doi:10.1016/j.molcel.2017.11.030 (2017).

15 Shah, P. P. *et al.* An atlas of lamina-associated chromatin across twelve human cell types reveals an intermediate chromatin subtype. *Genome Biol* **24**, 16, doi:10.1186/s13059-023-02849-5 (2023).

16 Reddy, K. L., Zullo, J. M., Bertolino, E. & Singh, H. Transcriptional repression mediated by repositioning of genes to the nuclear lamina. *Nature* **452**, 243-247, doi:10.1038/nature06727 (2008).

17 Poleshko, A. *et al.* Genome-Nuclear Lamina Interactions Regulate Cardiac Stem Cell Lineage Restriction. *Cell* **171**, 573-587 e514, doi:10.1016/j.cell.2017.09.018 (2017).

18 Ragoczy, T., Bender, M. A., Telling, A., Byron, R. & Groudine, M. The locus control region is required for association of the murine beta-globin locus with engaged transcription factories during erythroid maturation. *Genes & development* **20**, 1447-1457, doi:10.1101/gad.1419506 (2006).

19 Lieberman-Aiden, E. *et al.* Comprehensive mapping of long-range interactions reveals folding principles of the human genome. *Science (New York, N.Y.)* **326**, 289-293, doi:10.1126/science.1181369 (2009).

20 Dixon, J. R. *et al.* Topological domains in mammalian genomes identified by analysis of chromatin interactions. *Nature* **485**, 376-380, doi:10.1038/nature11082 (2012).

21 Rao, S. S. *et al.* A 3D map of the human genome at kilobase resolution reveals principles of chromatin looping. *Cell* **159**, 1665-1680, doi:10.1016/j.cell.2014.11.021 (2014).

22 Fudenberg, G. *et al.* Formation of Chromosomal Domains by Loop Extrusion. *Cell reports* **15**, 2038-2049, doi:10.1016/j.celrep.2016.04.085 (2016).

23 Haarhuis, J. H. I. *et al.* The Cohesin Release Factor WAPL Restricts Chromatin Loop Extension. *Cell* **169**, 693-707 e614, doi:10.1016/j.cell.2017.04.013 (2017).

24 Kim, E., Barth, R. & Dekker, C. Looping the Genome with SMC Complexes. *Annual review of biochemistry* **92**, 15-41, doi:10.1146/annurev-biochem-032620-110506 (2023).

25 Merkenschlager, M. & Nora, E. P. CTCF and Cohesin in Genome Folding and Transcriptional Gene Regulation. *Annu Rev Genomics Hum Genet* **17**, 17-43, doi:10.1146/annurev-genom-083115-022339 (2016).

26 Rao, S. S. P. *et al.* Cohesin Loss Eliminates All Loop Domains. *Cell* **171**, 305-320 e324, doi:10.1016/j.cell.2017.09.026 (2017).

27 Schwarzer, W. *et al.* Two independent modes of chromatin organization revealed by cohesin removal. *Nature* **551**, 51-56, doi:10.1038/nature24281 (2017).

28 Kind, J. *et al.* Genome-wide maps of nuclear lamina interactions in single human cells. *Cell* **163**, 134-147, doi:10.1016/j.cell.2015.08.040 (2015).

29 Gonzalez-Sandoval, A. *et al.* Perinuclear Anchoring of H3K9-Methylated Chromatin Stabilizes Induced Cell Fate in C. elegans Embryos. *Cell* **163**, 1333-1347, doi:10.1016/j.cell.2015.10.066 (2015).

30 Chang, L. *et al.* Nuclear peripheral chromatin-lamin B1 interaction is required for global integrity of chromatin architecture and dynamics in human cells. *Protein Cell* **13**, 258-280, doi:10.1007/s13238-020-00794-8 (2022).

31 Wang, Z. *et al.* Nuclear-lamin-guided plastic positioning and folding of the human genome. *Cell reports* **44**, 116529, doi:10.1016/j.celrep.2025.116529 (2025).

32 Zheng, X. *et al.* Lamins Organize the Global Three-Dimensional Genome from the Nuclear Periphery. *Molecular cell* **71**, 802-815 e807, doi:10.1016/j.molcel.2018.05.017 (2018).

33 Falk, M. *et al.* Heterochromatin drives compartmentalization of inverted and conventional nuclei. *Nature* **570**, 395-399, doi:10.1038/s41586-019-1275-3 (2019).

34 Zhang, H. & Blobel, G. A. Genome folding dynamics during the M-to-G1-phase transition. *Current opinion in genetics & development* **80**, 102036, doi:10.1016/j.gde.2023.102036 (2023).

35 Zhang, H. *et al.* Chromatin structure dynamics during the mitosis-to-G1 phase transition. *Nature* **576**, 158-162, doi:10.1038/s41586-019-1778-y (2019).

36 Zhang, H. *et al.* CTCF and transcription influence chromatin structure re-configuration after mitosis. *Nature communications* **12**, 5157, doi:10.1038/s41467-021-25418-5 (2021).

37 Zhao, H. *et al.* Genome folding principles uncovered in condensin-depleted mitotic chromosomes. *Nat Genet* **56**, 1213-1224, doi:10.1038/s41588-024-01759-x (2024).

38 Zhao, H. *et al.* Extensive mutual influences of SMC complexes shape 3D genome folding. *Nature* **640**, 543-553, doi:10.1038/s41586-025-08638-3 (2025).

39 Dileep, V. *et al.* Topologically associating domains and their long-range contacts are established during early G1 coincident with the establishment of the replication-timing program. *Genome research* **25**, 1104-1113, doi:10.1101/gr.183699.114 (2015).

40 Gibcus, J. H. *et al.* A pathway for mitotic chromosome formation. *Science (New York, N.Y.)* **359**, doi:10.1126/science.aao6135 (2018).

41 Naumova, N. *et al.* Organization of the mitotic chromosome. *Science (New York, N.Y.)* **342**, 948-953, doi:10.1126/science.1236083 (2013).

42 Pelham-Webb, B. *et al.* H3K27ac bookmarking promotes rapid post-mitotic activation of the pluripotent stem cell program without impacting 3D chromatin reorganization. *Molecular cell* **81**, 1732-1748 e1738, doi:10.1016/j.molcel.2021.02.032 (2021).

43 Guttinger, S., Laurell, E. & Kutay, U. Orchestrating nuclear envelope disassembly and reassembly during mitosis. *Nature reviews. Molecular cell biology* **10**, 178-191, doi:10.1038/nrm2641 (2009).

44 Wong, X. *et al.* Lamin C is required to establish genome organization after mitosis. *Genome Biol* **22**, 305, doi:10.1186/s13059-021-02516-7 (2021).

45 Moir, R. D., Yoon, M., Khuon, S. & Goldman, R. D. Nuclear lamins A and B1: different pathways of assembly during nuclear envelope formation in living cells. *The Journal of cell biology* **151**, 1155-1168, doi:10.1083/jcb.151.6.1155 (2000).

46 Ellenberg, J. *et al.* Nuclear membrane dynamics and reassembly in living cells: targeting of an inner nuclear membrane protein in interphase and mitosis. *The Journal of cell biology* **138**, 1193-1206, doi:10.1083/jcb.138.6.1193 (1997).

47 Kaya-Okur, H. S. *et al.* CUT&Tag for efficient epigenomic profiling of small samples and single cells. *Nature communications* **10**, 1930, doi:10.1038/s41467-019-09982-5 (2019).

48 Solovei, I. *et al.* LBR and lamin A/C sequentially tether peripheral heterochromatin and inversely regulate differentiation. *Cell* **152**, 584-598, doi:10.1016/j.cell.2013.01.009 (2013).

49 Hsiung, C. C. *et al.* A hyperactive transcriptional state marks genome reactivation at the mitosis-G1 transition. *Genes & development* **30**, 1423-1439, doi:10.1101/gad.280859.116 (2016).

50 Nishimura, K., Fukagawa, T., Takisawa, H., Kakimoto, T. & Kanemaki, M. An auxin-based degron system for the rapid depletion of proteins in nonplant cells. *Nat Methods* **6**, 917-922, doi:10.1038/nmeth.1401 (2009).

51 Nabet, B. *et al.* The dTAG system for immediate and target-specific protein degradation. *Nat Chem Biol* **14**, 431-441, doi:10.1038/s41589-018-0021-8 (2018).

52 Hirano, Y. *et al.* Lamin B receptor recognizes specific modifications of histone H4 in heterochromatin formation. *The Journal of biological chemistry* **287**, 42654-42663, doi:10.1074/jbc.M112.397950 (2012).

53 Metelova, M., Vigh, M. L. & Krietenstein, N. Deciphering histone mark-specific fine-scale chromatin organization at high resolution with Micro-C-ChIP. *Nature communications* **16**, 9331, doi:10.1038/s41467-025-64350-w (2025).

54 Aboreden, N. G. *et al.* Cis-regulatory chromatin contacts form de novo in the absence of loop extrusion. *bioRxiv*, doi:10.1101/2025.01.12.632634 (2025).

55 Wang, H. *et al.* CRISPR-Mediated Programmable 3D Genome Positioning and Nuclear Organization. *Cell* **175**, 1405-1417 e1414, doi:10.1016/j.cell.2018.09.013 (2018).

56 van Schaik, T. *et al.* CTCF and cohesin promote focal detachment of DNA from the nuclear lamina. *Genome Biol* **23**, 185, doi:10.1186/s13059-022-02754-3 (2022).

57 Zhao, Y. *et al.* Accelerating 3D genomics data analysis with Microcket. *Commun Biol* **7**, 675, doi:10.1038/s42003-024-06382-4 (2024).

58 Durand, N. C. *et al.* Juicer Provides a One-Click System for Analyzing Loop-Resolution Hi-C Experiments. *Cell Syst* **3**, 95-98, doi:10.1016/j.cels.2016.07.002 (2016).

59 Wolff, J. *et al.* Galaxy HiCExplorer 3: a web server for reproducible Hi-C, capture Hi-C and single-cell Hi-C data analysis, quality control and visualization. *Nucleic acids research* **48**, W177-W184, doi:10.1093/nar/gkaa220 (2020).

60 Flyamer, I. M., Illingworth, R. S. & Bickmore, W. A. Coolpup.py: versatile pile-up analysis of Hi-C data. *Bioinformatics* **36**, 2980-2985, doi:10.1093/bioinformatics/btaa073 (2020).

61 Fulco, C. P. *et al.* Activity-by-contact model of enhancer-promoter regulation from thousands of CRISPR perturbations. *Nat Genet* **51**, 1664-1669, doi:10.1038/s41588-019-0538-0 (2019).

62 Thompson, A. P. *et al.* LAMMPS-a flexible simulation tool for particle-based materials modeling at the atomic, meso, and continuum scales. *Comput Phys Commun* **271**, doi:ARTN 108171
10.1016/j.cpc.2021.108171 (2022).

63 Dogan, N. *et al.* Occupancy by key transcription factors is a more accurate predictor of enhancer activity than histone modifications or chromatin accessibility. *Epigenetics Chromatin* **8**, 16, doi:10.1186/s13072-015-0009-5 (2015).

64 Wu, W. *et al.* Dynamic shifts in occupancy by TAL1 are guided by GATA factors and drive large-scale reprogramming of gene expression during hematopoiesis. *Genome research* **24**, 1945-1962, doi:10.1101/gr.164830.113 (2014).

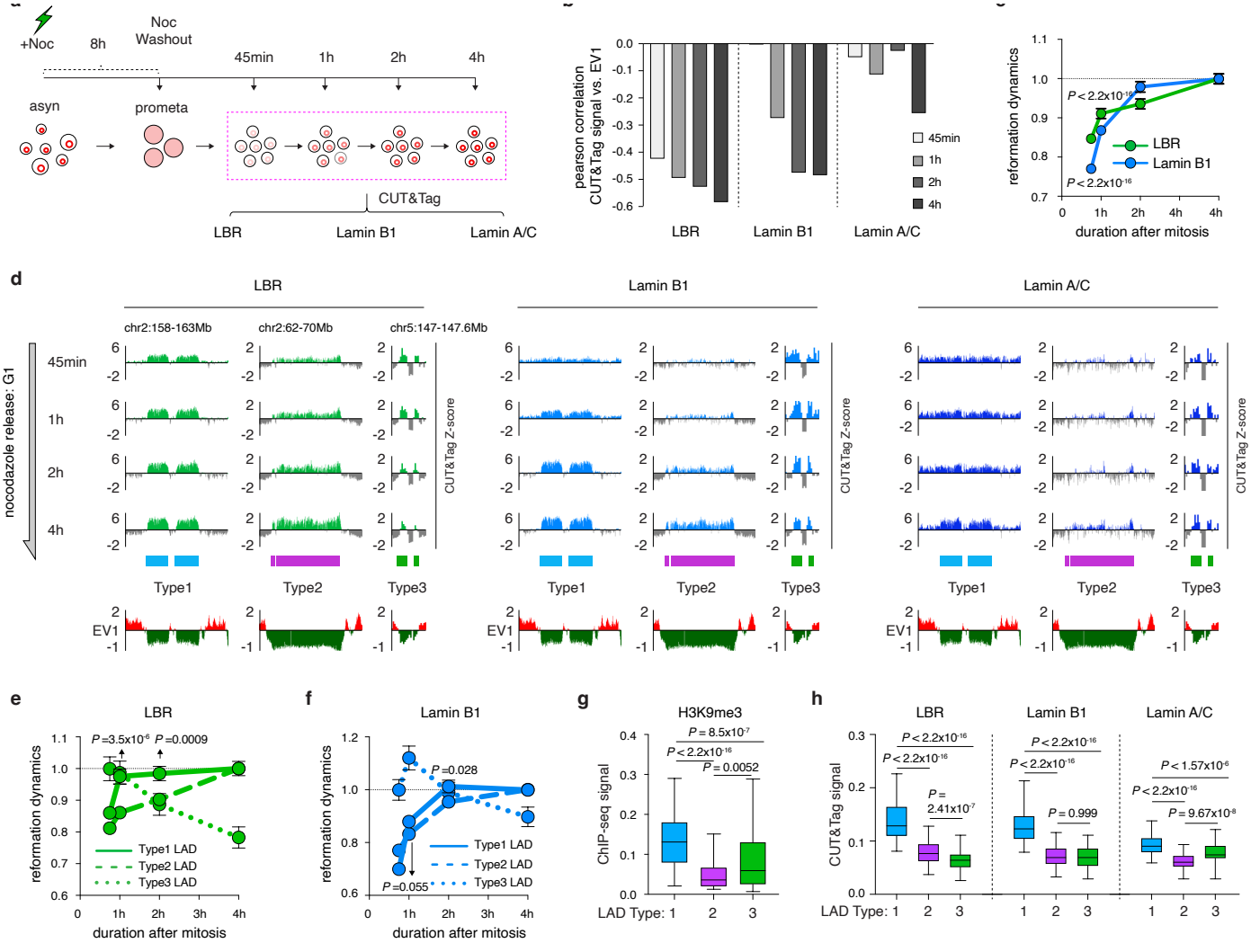

Figure Legends:

Figure 1: Dynamic re-association of chromatin and NE-associating factors after mitosis. a, Schematic illustration showing the nocodazole prometaphase arrest/release strategy to obtain post-mitotic cells at defined time points. **b**, Bar graph showing the pearson correlation coefficient between NL component CUT&Tag signal intensity and EV1 values across all post-mitotic time points. Negative correlation indicates overlap between NE-chromatin association and B-type compartments. **c**, Line graph showing more rapid post-mitotic recruitment of LBR than Lamin B1. *P* values were calculated using a two-sided paired Wilcoxon signed-rank test. **d**, Genomic tracks showing the binding profile of LBR, Lamin B1 and Lamin A/C in Type 1, 2 and 3 LADs across post-mitotic time points. Tracks of corresponding EV1 values were shown in parallel. **e**, Line graph showing LBR binding dynamics in Type1, 2 and 3 LADs. *P* values were calculated using a two-sided Wilcoxon signed-rank test. **f**, Line graph showing Lamin B1 binding dynamics in Type1, 2 and 3 LADs. *P* values were calculated using a two-sided Wilcoxon signed-rank test. **g**, Boxplots showing the H3K9me3 ChIP-seq signals in Type1, 2 and 3 LADs. **h**, Boxplots showing the CUT&Tag signals of indicated NE-associating factors in Type1, 2 and 3 LADs. For all boxplots, central line denotes median. Box limits denote 25th–75th percentile; whiskers denote 5th–95th percentile. *P* values were calculated using a two-sided Wilcoxon signed-rank test.

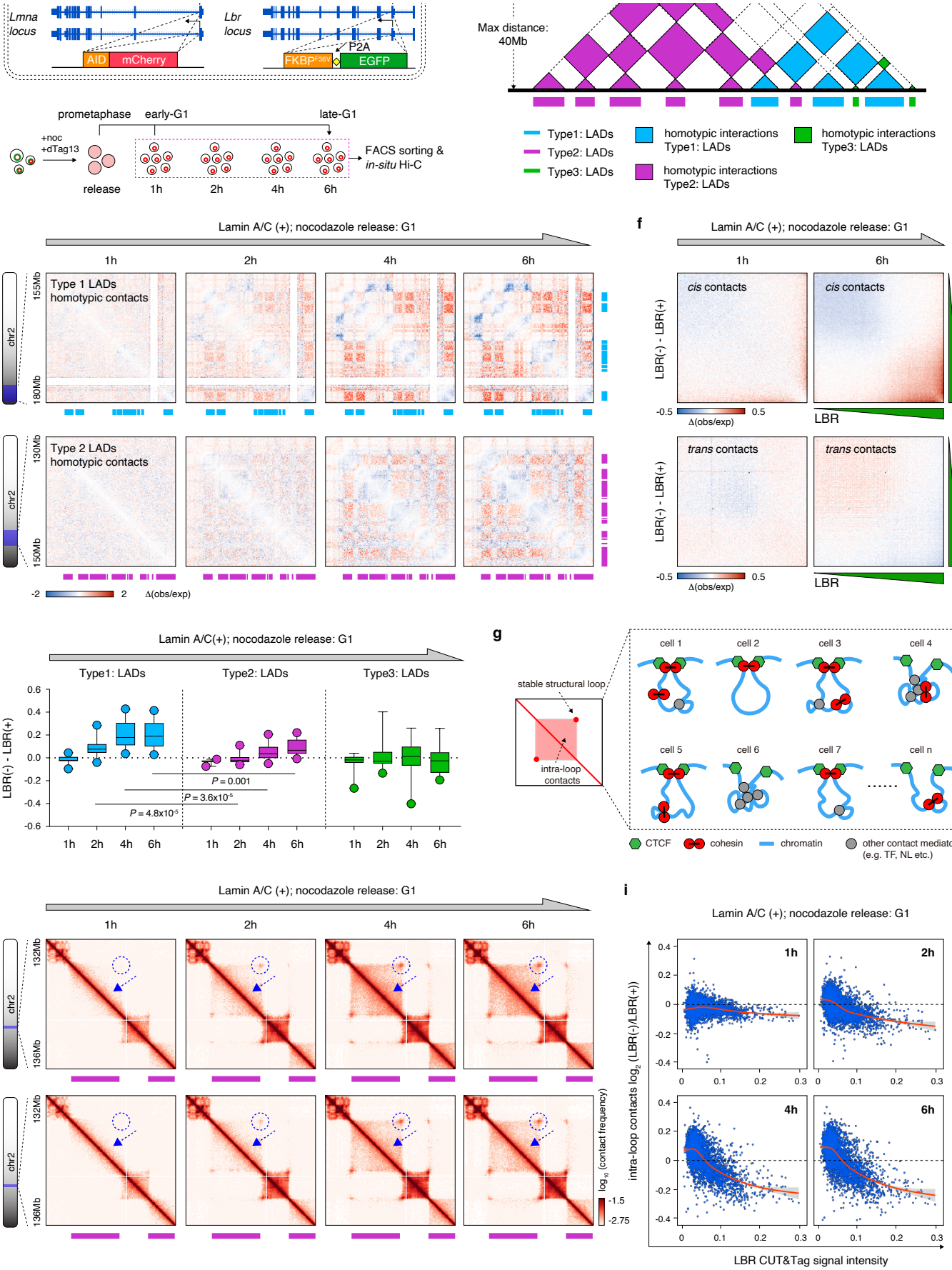

Figure 2: LBR influences post-mitotic genome refolding. a, Schematic illustration, showing the gene editing strategy to generate *Lmna*^{mAID}/*Lbr*^{dTag} cell line. **b**, Schematic illustration, showing the strategy to harvest post-mitotic cells without LBR. **c**, Schematic illustration, showing homotypic interactions within a specific LAD type. **d**, Differential KR-balanced, 100kb binned Hi-C contact matrices showing the progressive gain of homotypic interactions among Type1 or Type2 LADs upon LBR depletion after mitosis. Type1 and 2 LADs were demarcated by blue and purple bars respectively. **e**, Boxplots showing that LBR depletion triggered progressive increments of homotypic interactions within Type1 and 2 LADs. **f**, Differential LBR-based saddle plots showing strengthened LAD self-association in *cis* but not in *trans* upon LBR depletion in late-G1 phase. **g**, Cartoon illustration showing examples of cohesin loop extrusion intermediates that contribute to the intra-loop contact signals. **h**, KR-balanced, 25kb binned Hi-C contact matrices showing a representative structural loop (dotted circle) located within LADs. Note that the intra-loop contacts were reduced by LBR depletion in late-G1 phase (dotted arrow). **i**, Scatter plots showing that intra-loop contact reduction upon LBR loss is positively correlated with internal LBR signal intensity. For all boxplots, central line denotes median. Box limits denote 25th–75th percentile; whiskers denote 5th–95th percentile. *P* values were calculated using a two-sided Wilcoxon signed-rank test.

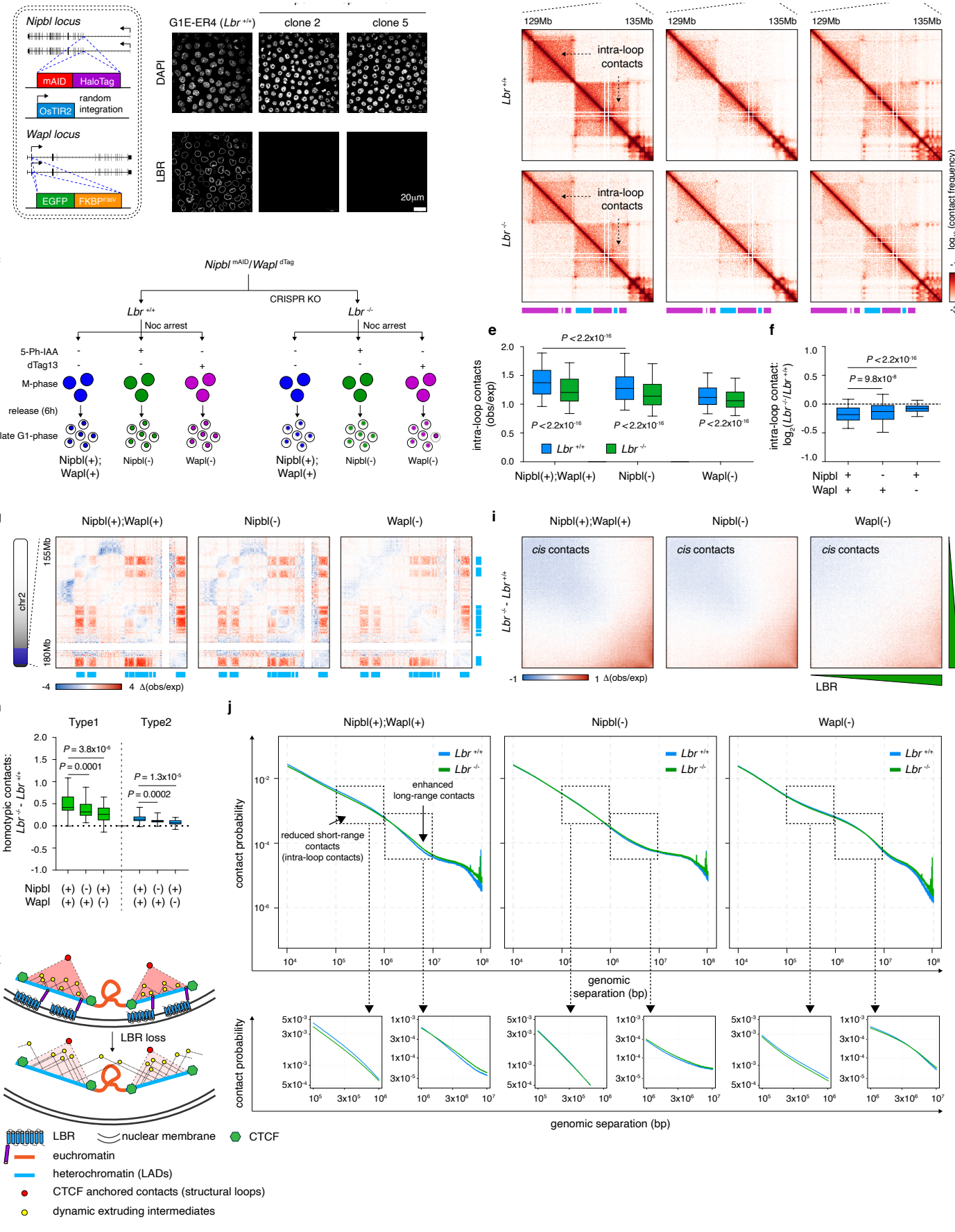

Figure 3: Under- or overload of cohesin both attenuate the impacts of LBR loss on post-mitotic genome refolding. a, Schematic illustration, showing the genome editing strategy of *Nipbl*^{mAID}/*Wapl*^{dTag} cells. **b**, Immunofluorescence staining confirming the results of CRISPR mediated LBR knockout in *Nipbl*^{mAID}/*Wapl*^{dTag} cells. Scale bar: 20μm. **c**, Schematic illustration, showing strategy to obtain late-G1 phase Nipbl(+)/Wapl(+), Nipbl(-) or Wapl(-) cells under LBR-replete or deficient background. **d**, KR-balanced, 25kb-binned, Hi-C contact maps showing that Nipbl or Wapl loss could mitigate LBR-depletion-induced reduction in intra-loop contacts. Type1 and 2 LADs were demarcated by blue and purple bars. **e**, Boxplots showing the reduced intra-loop contacts for structural loops in LADs (LBR signal > 0.1) upon LBR depletion. Nipbl(+)/Wapl(+), Nipbl(-) and Wapl(-) conditions were shown respectively. *P* values were calculated using a two-sided paired Wilcoxon signed-rank test. **f**, Boxplots showing the $\log_2$ fold change of intra-loop contact strength upon LBR loss. Nipbl(+)/Wapl(+), Nipbl(-) and Wapl(-) conditions were shown respectively. *P* values were calculated using a two-sided paired Wilcoxon signed-rank test. **g**, Differential KR-balanced, 25kb-binned Hi-C contact matrices showing that Nipbl or Wapl loss could attenuate LBR-depletion-induced LAD self-association. LADs are labeled by blue bars. **h**, Boxplots showing that the LBR loss-induced gain of LAD self-association was attenuated in cells lacking Nipbl or Wapl. *P* values were calculated using a two-sided paired Wilcoxon signed-rank test. **i**, Differential LBR-based saddle plots showing that the strengthened LAD self-association was weakened by Nipbl or Wapl depletion. **j**, Left panel: P_S curve of LBR-replete or deficient cells. Arrows indicate the changes on P_S curve upon LBR loss. Zoom-in views were provided. Middle panel: attenuated impacts on P_S curve upon LBR loss in Nipbl-deficient cells. Right panel: attenuated impacts on P_S curve upon LBR loss in Wapl-deficient cells. **k**, Cartoon illustration showing that LBR loss could unleash cohesin loop extrusion, leading to reduced intra-loop contacts and enhanced LAD self-association. For all box plots in this figure, box limits denote 25th–75th percentile; whiskers denote 5th–95th percentile.

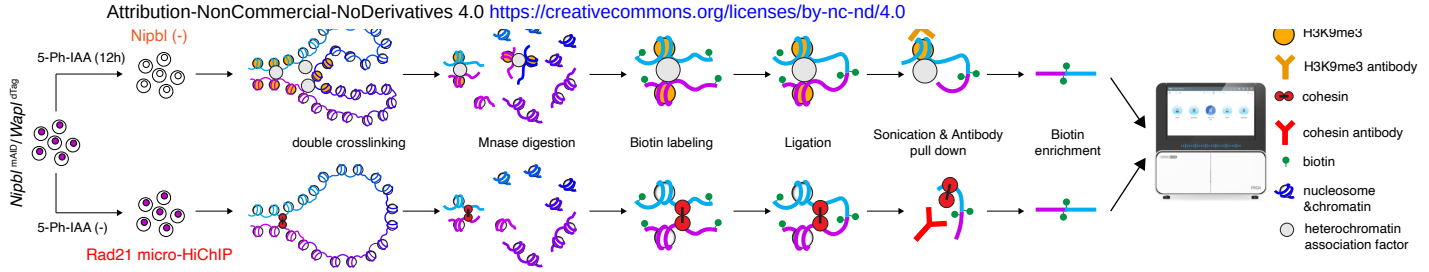

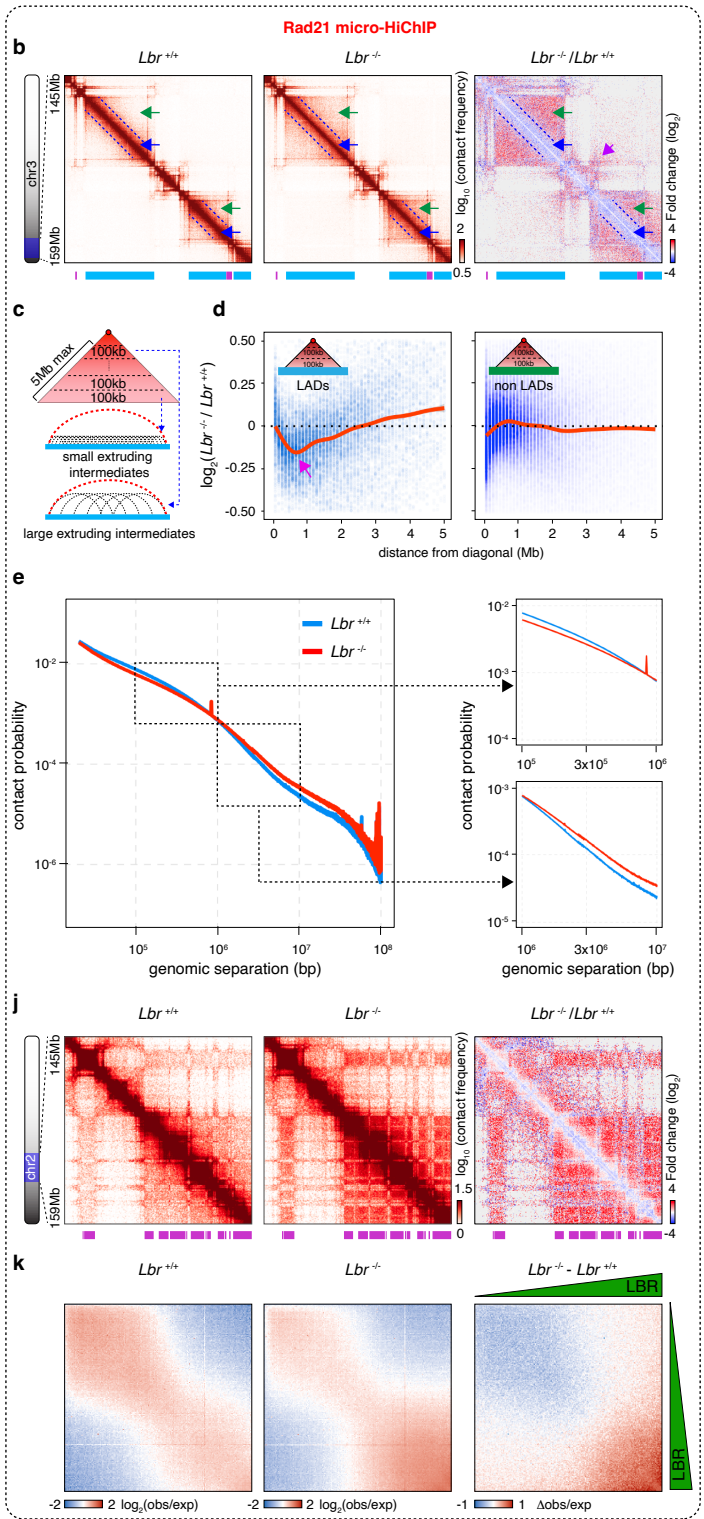

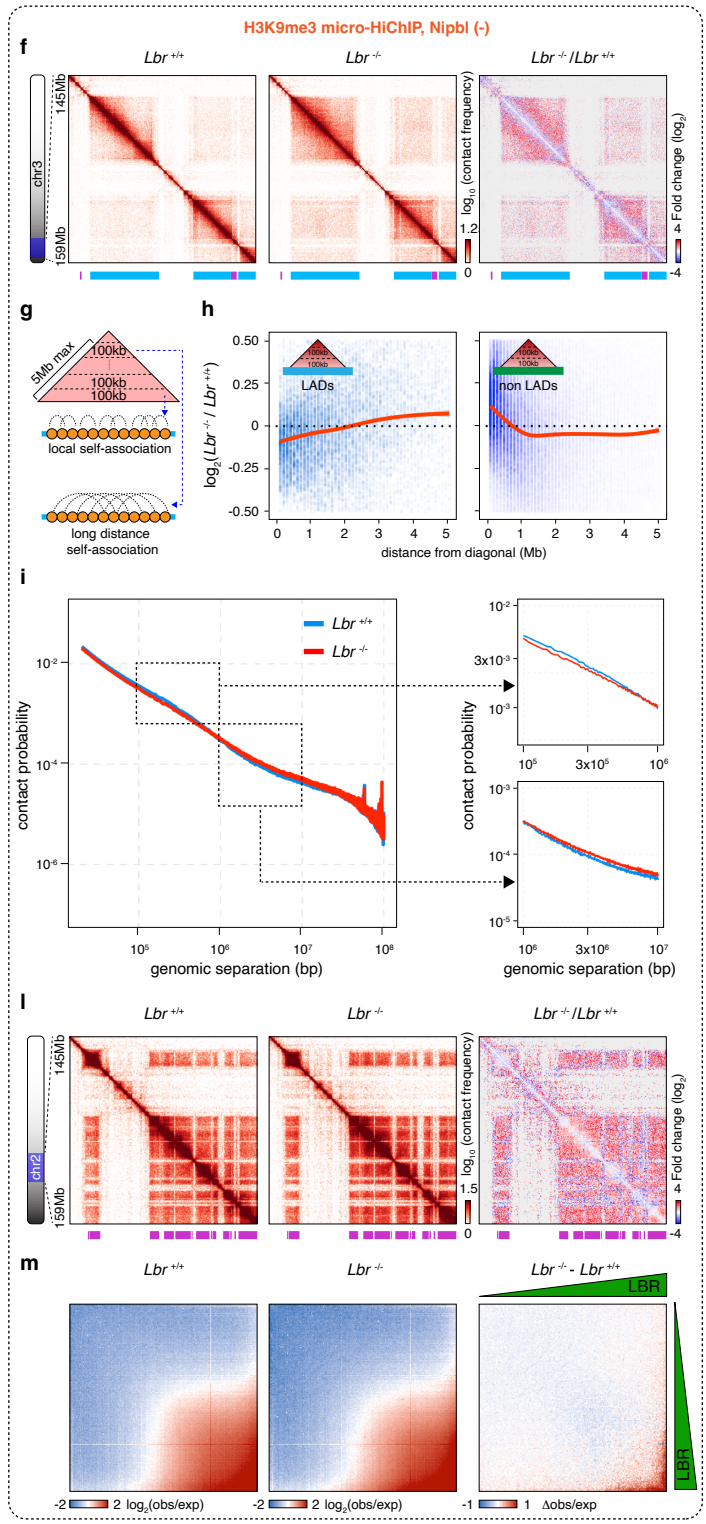

Figure 4: LBR loss directly affects cohesin-mediated chromatin contacts. a, Schematic illustration, showing the experimental workflow of micro-HiChIP targeting Rad21 or H3K9me3 respectively. **b**, Raw, 25kb-binned Rad21 micro-HiChIP contact maps showing the expansion of cohesin-mediated contacts upon LBR loss. Concentrated short-range contacts at diagonal proximal regions are indicated by blue dotted lines. LBR-loss-induced reduction of short-range contacts and gain of long-range contacts within structural loops are indicated by blue and green arrows, respectively. Gain of inter-LAD contacts mediated by cohesin is indicated by the purple arrow. Type1 and 2 LADs are demarcated by blue and purple bars respectively. **c**, Schematic illustration, showing the segmentation of structural loop domains into 100kb-wide stripes. **d**, Line plots showing the LBR-loss induced reduction of cohesin-mediated short-range interactions (<2-3Mb) and gain of longer range interactions (>2-3Mb) within LAD-located structural loop domains. Note that for non-LAD located structural loops, no such changes were observed. **e**, P_S curves showing the bidirectional shift of contact frequency upon LBR depletion. **f-i**, Similar to (**b-e**) showing weaker changes of H3K9me3 associated contacts upon LBR loss in the Nipbl-deficient cells. **j**, Raw, 100kb-binned micro-HiChIP contact matrices showing elevated levels of cohesin-mediated inter-LAD contacts upon LBR loss. LADs are demarcated by purple bars. **k**, LBR-based saddle plots showing gain of cohesin-mediated LAD self-association upon LBR depletion. **l-m**, Similar to (**j-k**) showing that LBR-induced LAD self-association without cohesin is only observed for LADs with strongest LBR binding signals.

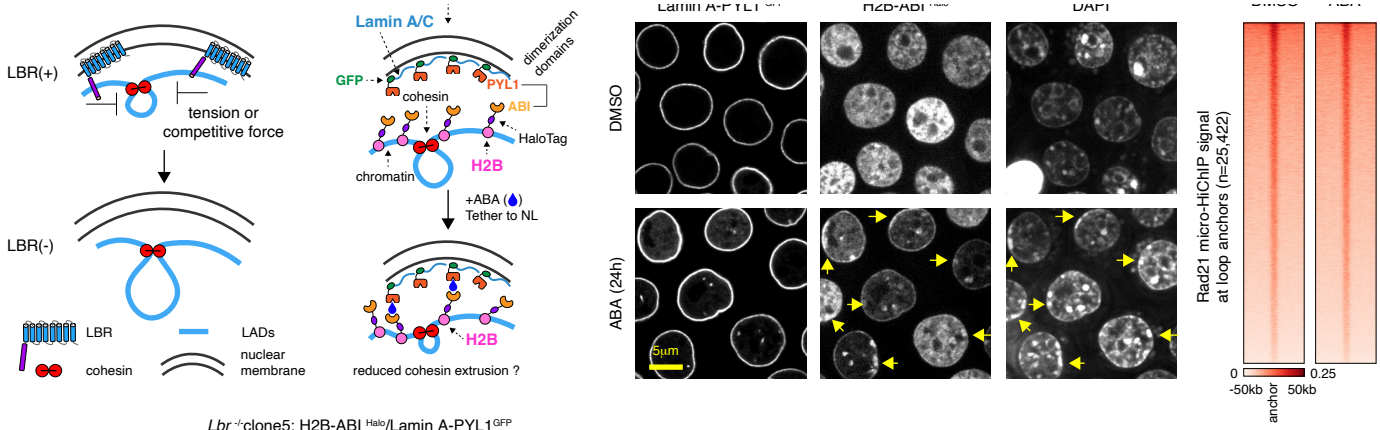

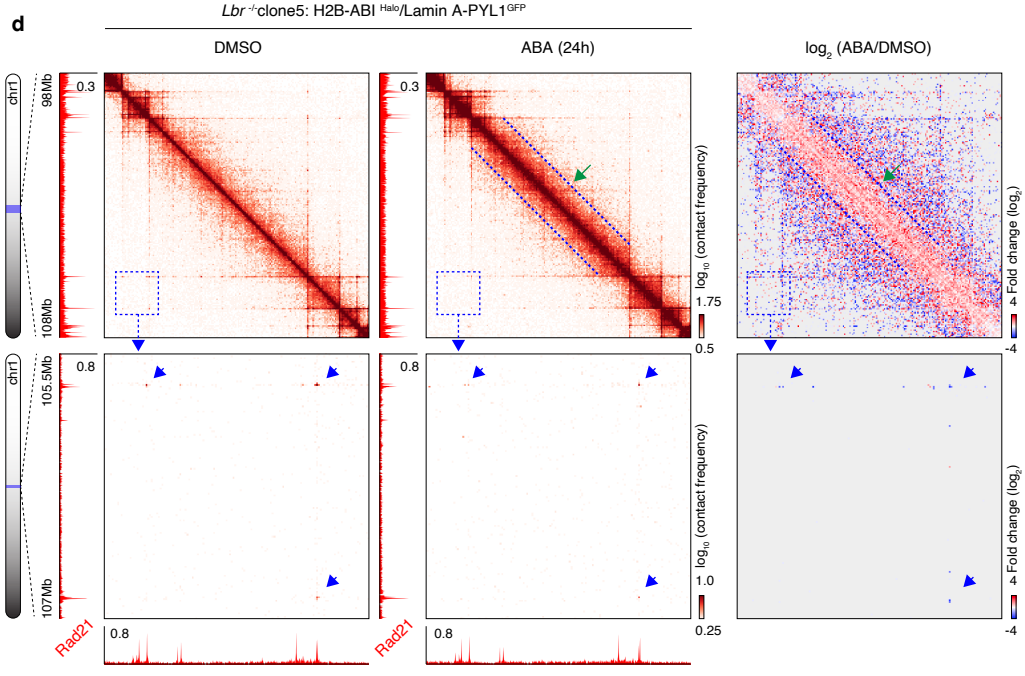

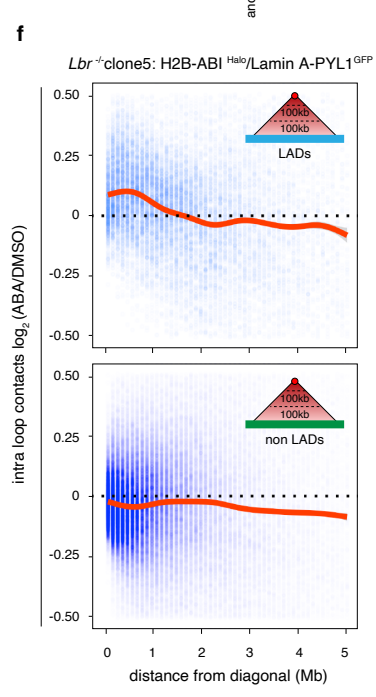

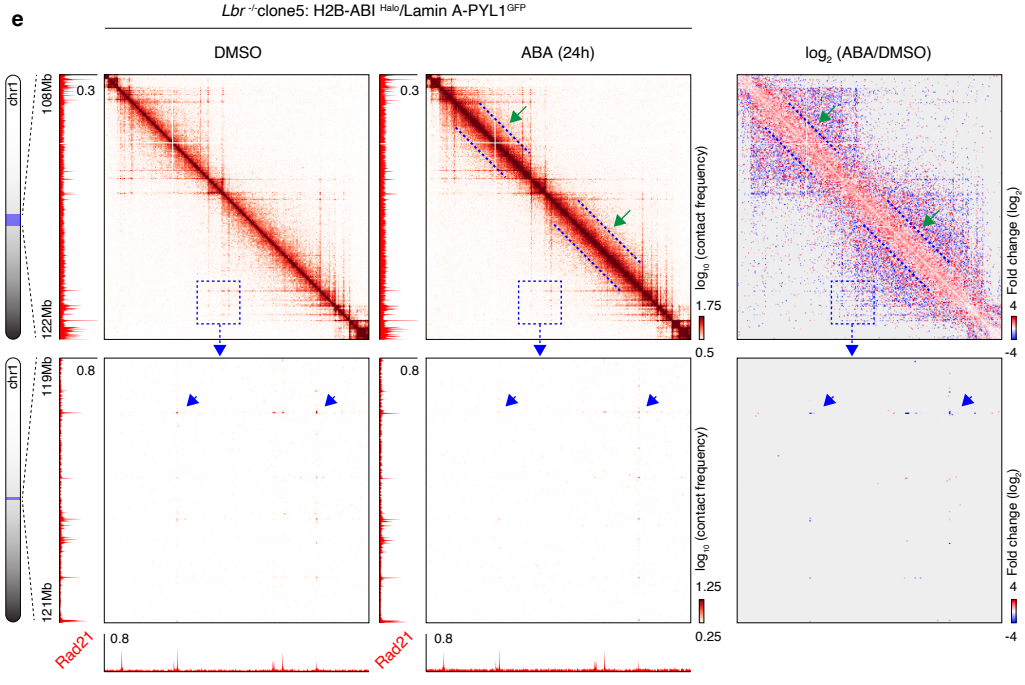

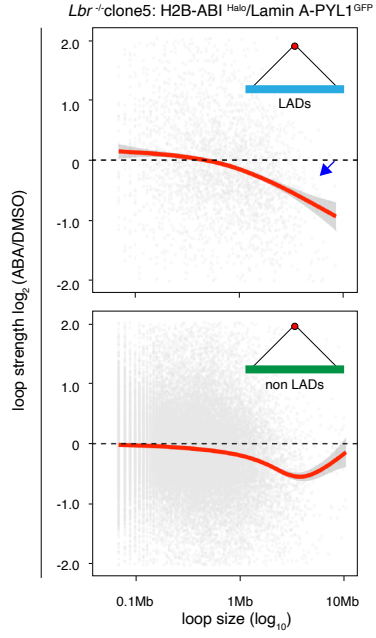

Figure 5: Bulk chromatin-tethering to the nuclear periphery results in constrained cohesin loop extrusion. a, A tension model to explain how LBR-mediated nuclear periphery anchorage restricts of cohesin loop extrusion. **b,** Experimental design to relocate bulk chromatin (H2B) to nuclear lamina (Lamin A) using the ABA mediated ABI-PYL1 dimerization system. **c**, Representative images showing the nuclear periphery localization of H2B upon ABA treatment for 24 hours (yellow arrows). Scale bar: 5μm. **d**, Raw, 50kb-binned Rad21 micro-HiChIP contact matrices showing gain of cohesin-mediated short-range contacts (dotted blue lines and green arrows) within loop domains upon ABA treatment. Zoom-in views are 10kb-binned contact matrices showing reduced structural loop strength upon ABA treatment (blue arrows). Genomic tracks of Rad21 ChIP profile are shown in parallel. **e**, Similar to **d**, showing another representative locus. **f**, Line plots showing that bulk chromatin tether by ABA treatment leads to the gain of short-range intra-loop contacts within LAD-located loops. **g**, Line plots showing that bulk chromatin tether by ABA treatment results in a reduction of large structural loop signal intensity. LAD and non-LAD located loops were shown respectively. **h**, Heatmap showing that Rad21 micro-HiChIP signals are not measurably changed upon ABA treatment.

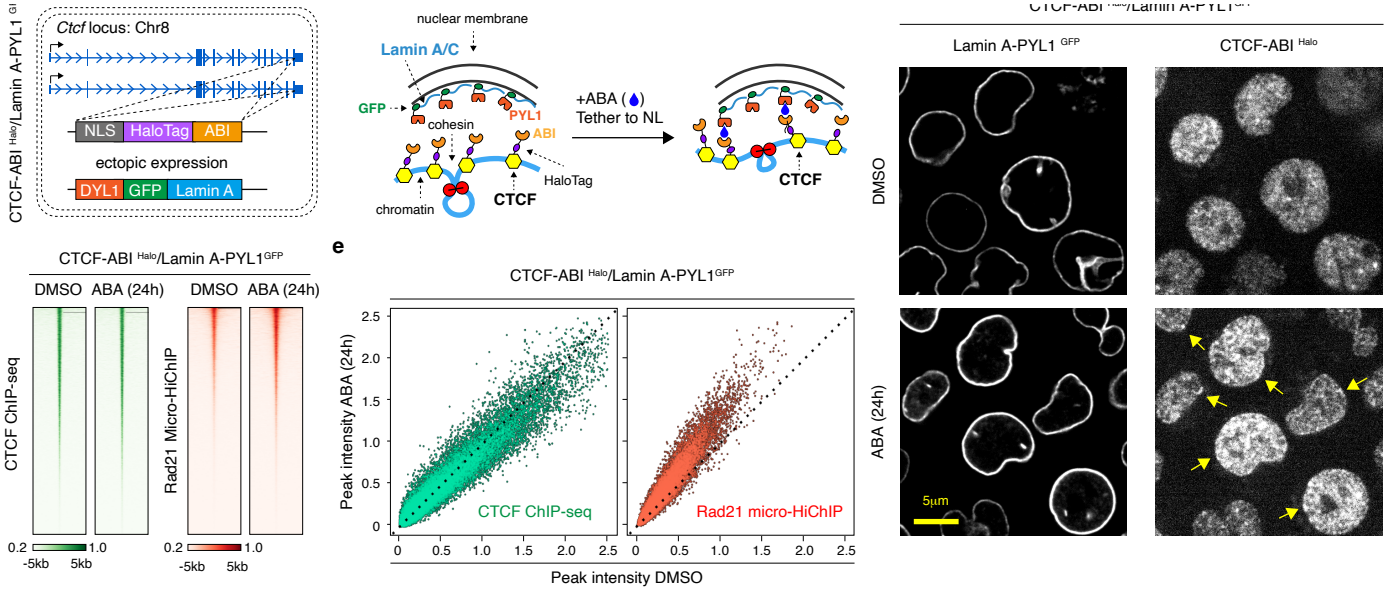

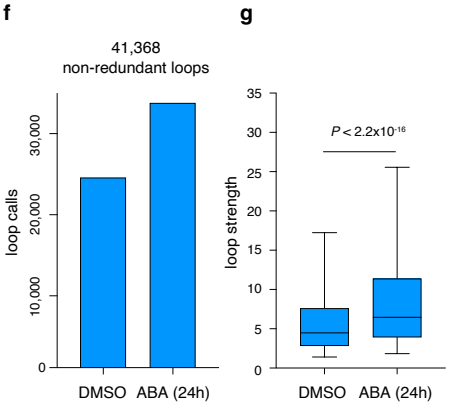

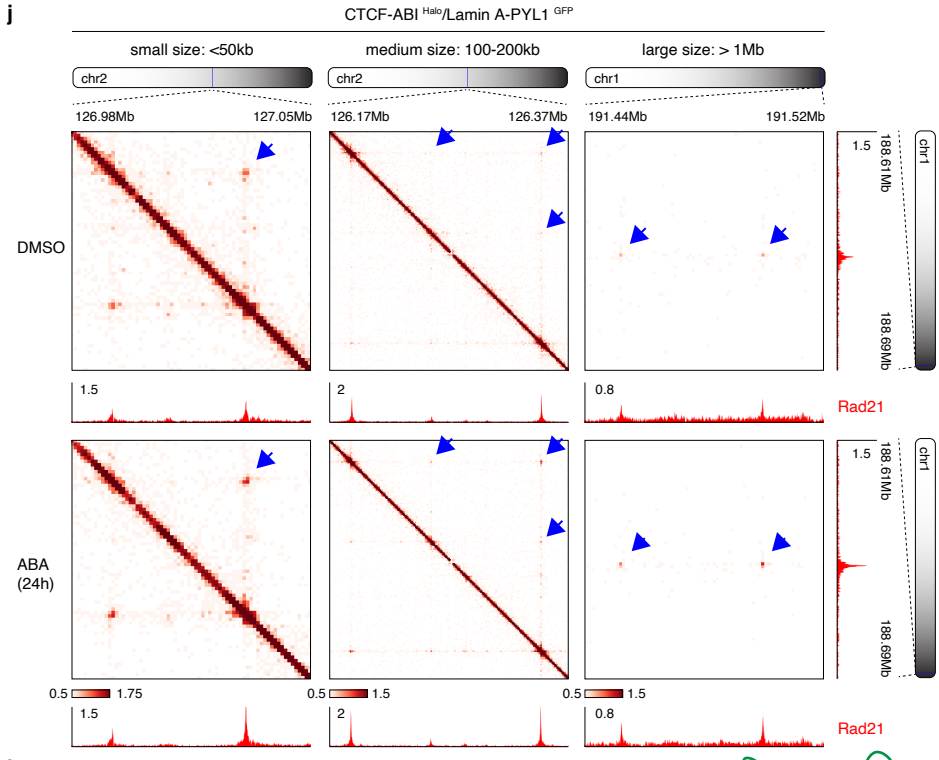

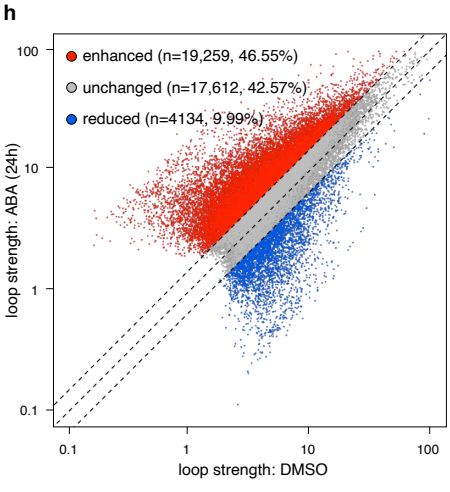

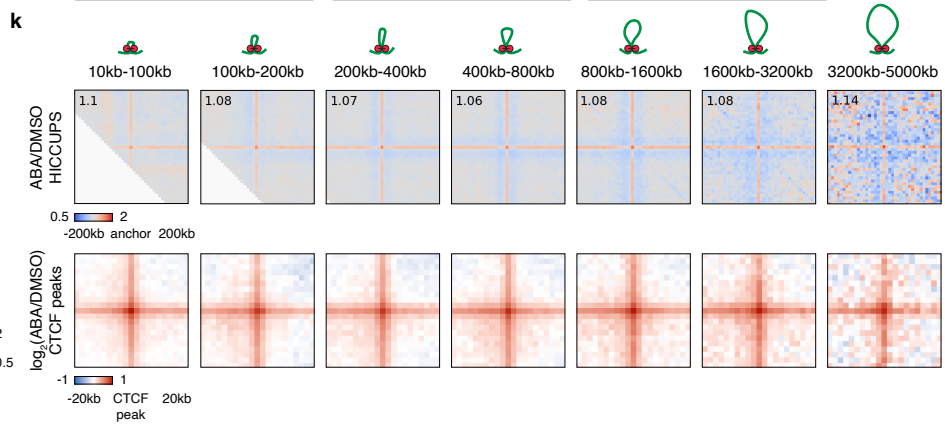

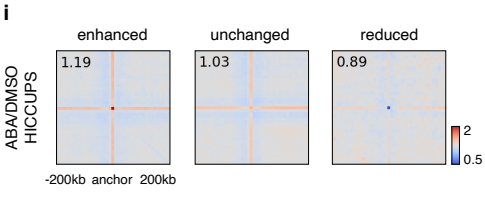

Figure 6: Focal tethering CTCF binding sites (CBS) to the nuclear periphery stabilizes local cohesin occupancy and promotes loop formation. a, Schematic illustration, showing the genome editing strategy to generate CTCF-ABI^{Halo}/Lamin A-PYL1^{GFP} cells. **b**, Experimental design to position CBS at the nuclear lamina (point tether). **c**, Representative image showing the enrichment of CTCF at nuclear rim (yellow arrows). **d**, Heatmap showing the ChIP-seq signals of CTCF-ABI^{Halo} and the micro-HiChIP signals of Rad21 before and after ABA treatment. **e**, Scatter plot showing that Rad21 but not CTCF occupancy at CBS was elevated upon ABA treatment. **f**, Bar graph showing the number of HICCUPS loop calls with or without ABA treatment. **g**, Boxplots showing that loop strength was significant larger in the ABA treated samples. **h**, Scatter plots showing that a large fraction of loops was strengthened upon ABA treatment. **i**, APA plots showing the ratio of composite loop signals in ABA-treated samples relative to DMSO controls for the indicated loop groups. **j**, Representative raw 1kb binned Rad21 micro-HiChIP contact maps showing that small, medium or large-sized loops (blue arrows) were increased upon ABA treatment. Genomic tracks of Rad21 was shown in parallel. **k**, Upper panel: APA plots (10kb) showing the enrichment ratio (ABA/DMSO) of composite signals for identified loops across the indicated size ranges. Lower panel: APA plots (1kb) showing the log2 fold change (ABA relative to DMSO) for all possible pairs of CTCF peaks, stratified by genomic separation. For all boxplots, central line denotes median. Box limits denote 25th–75th percentile; whiskers denote 5th–95th percentile. *P* values were calculated using a two-sided paired Wilcoxon signed-rank test.

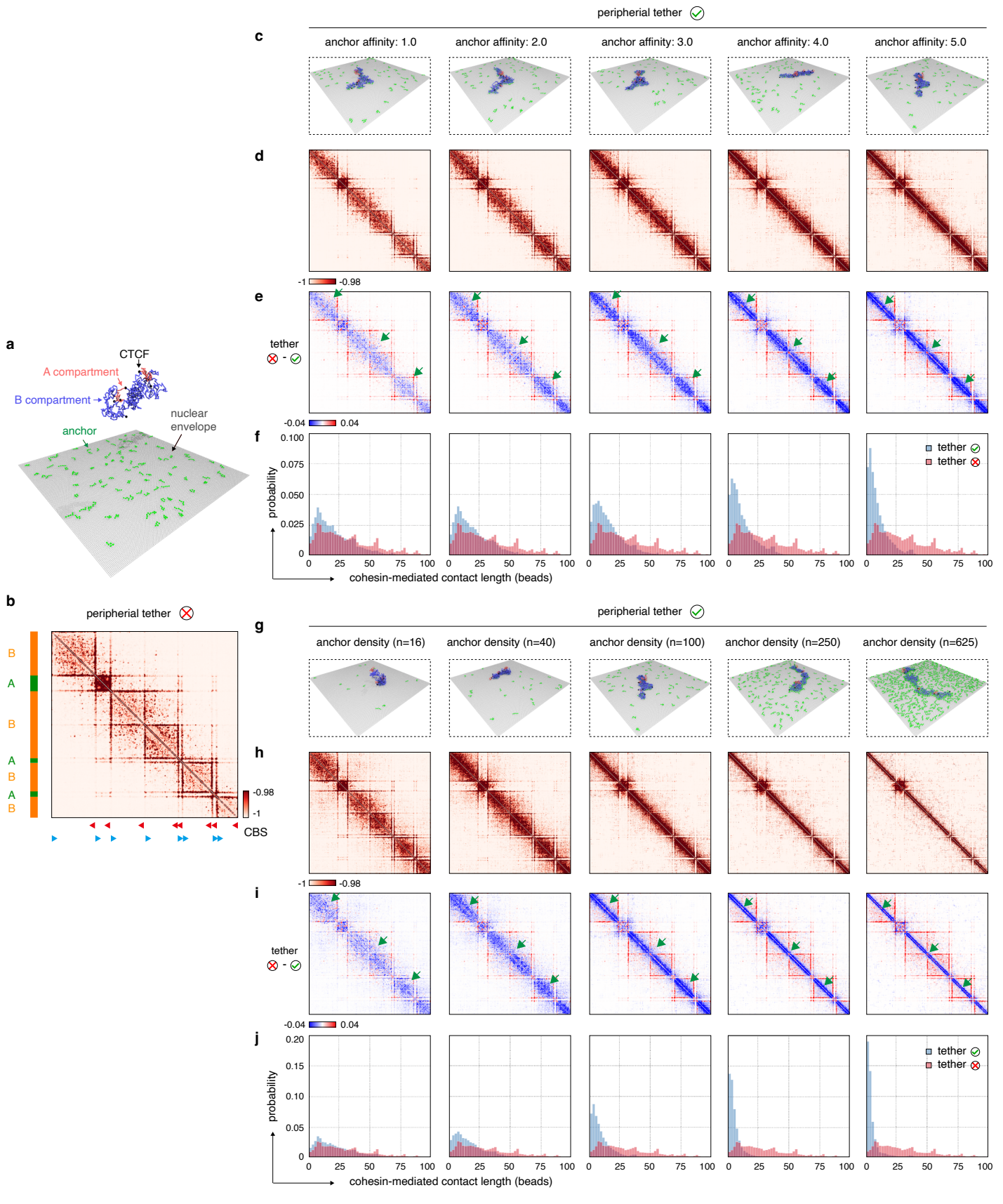

Figure 7: Polymer simulation of bulk chromatin tethering to the NE. a, Simulation snapshot showing the chromatin polymer without NE attachment. **b**, Simulated contact map of cohesin-mediated interactions in the absence of peripheral tethering. **c**, Representative simulation snapshots of the chromatin polymer, illustrating the chromatin conformation at the indicated anchor affinities. **d**, Simulated contact maps showing the patterns of cohesin-mediated contacts across the indicated range of B-compartment/anchor affinities. **e**, Differential contact maps (control subtracted by tethered) showing a progressive gain in short-range interactions as B-compartment/anchor affinity increases. **f**, Histograms showing the frequency distribution of cohesin-mediated contact lengths for control and tethered simulations across the indicated B-compartment/anchor affinities. (**g**-**j**), Similar to (**c**-**f**) showing the influence of anchor density on cohesin-mediated contacts.

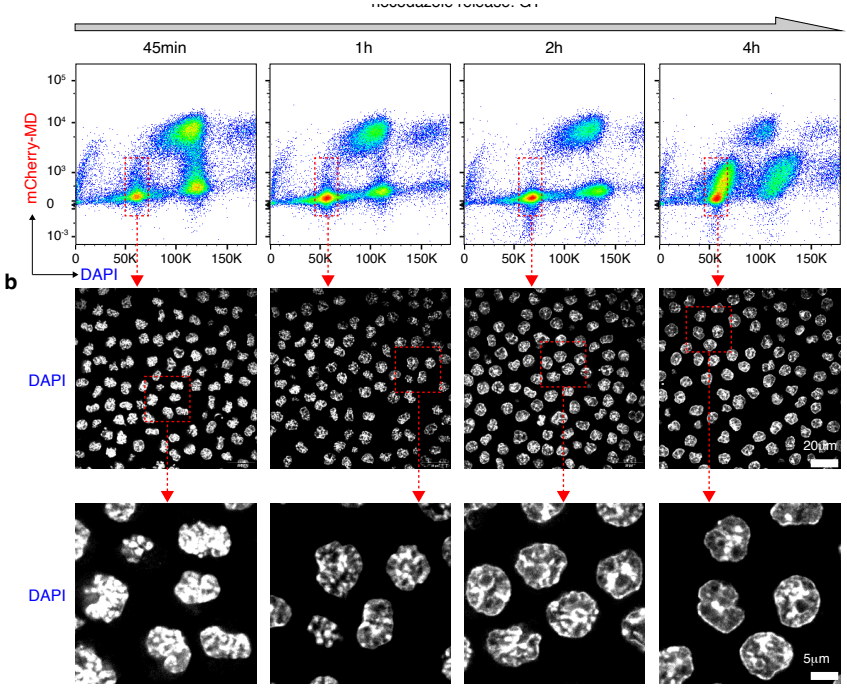

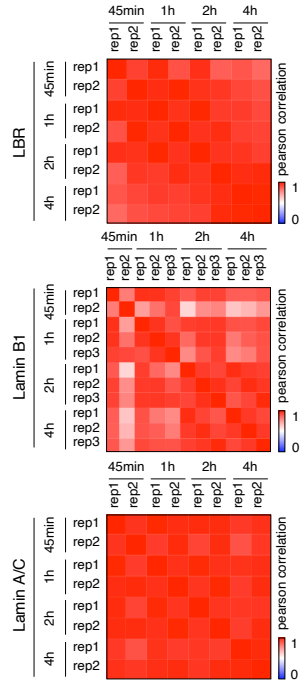

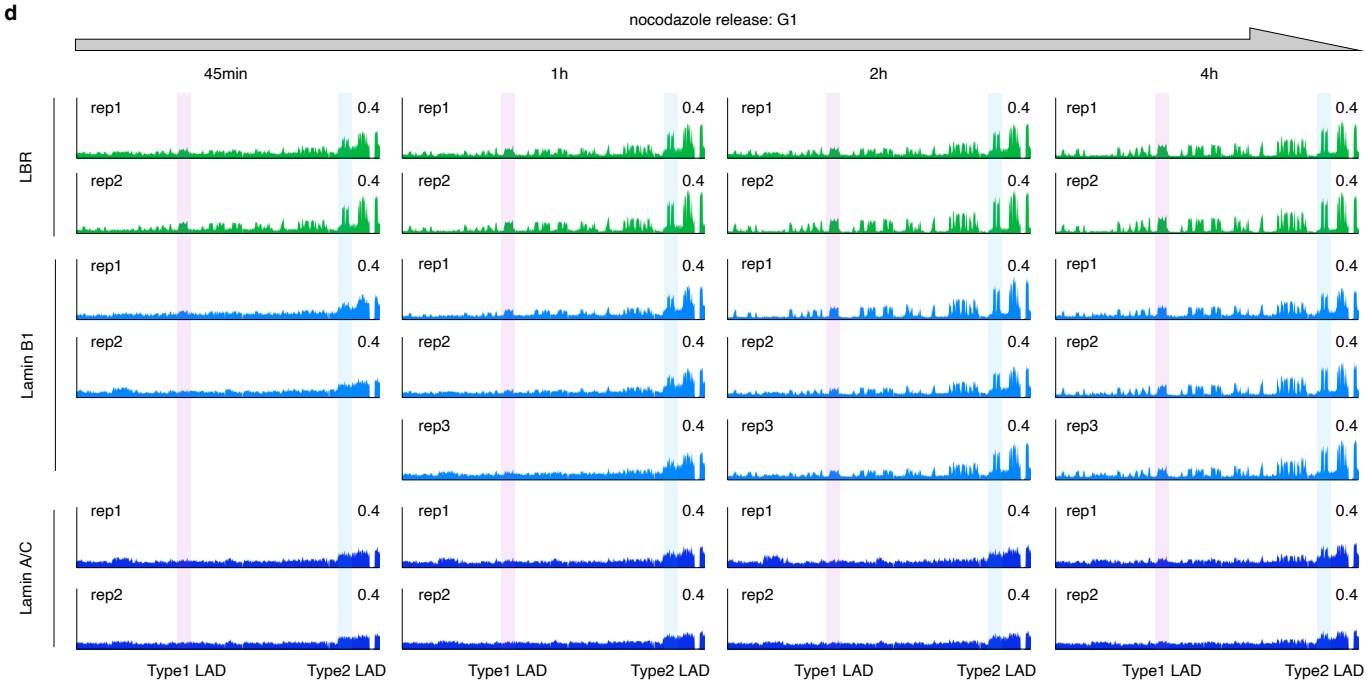

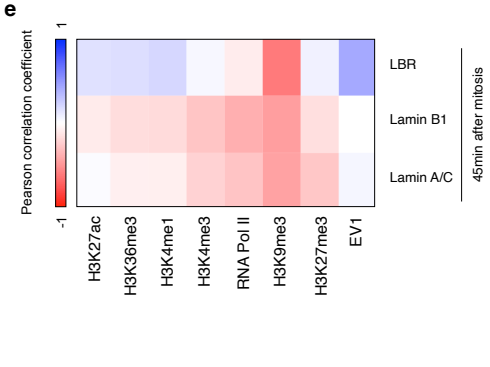

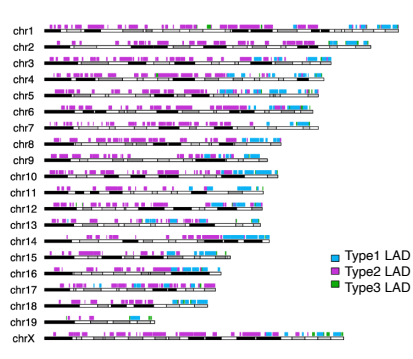

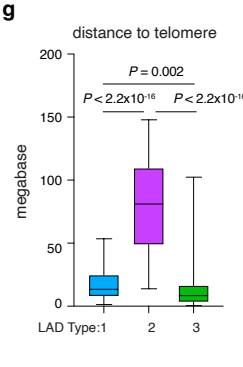

Extended Data Figure 1: Post-mitotic cell sorting. a, Flow plots showing the sorting strategy of newborn G1-phase cells after nocodazole release. **b**, Fluorescence images of sorted cells. Zoom-in views are provided. Scale bars: 20μm (5μm for zoom-in view). **c**, Heatmap showing the high correlation among biological replicates in CUT&Tag experiments. **d**, Tracks showing the dynamic recruitment of LBR, Lamin B1 and Lamin A/C after mitosis. Tracks of individual replicates are plotted. **e**, Heatmap showing the high correlation of LBR occupancy with H3K9me3 constitutive heterochromatin mark at early-G1 phase (45min). **f**, Genomic position of Type1, 2 and 3 LADs. Note that Type 1 and 3 LADs are located in telomere-proximal regions. **g**, Boxplots showing the distance to telomere of Type1, 2 and 3 LADs. For all boxplots, central line denotes median. Box limits denote 25th–75th percentile; whiskers denote 5th–95th percentile. *P* values were calculated using a two-sided Wilcoxon signed-rank test.

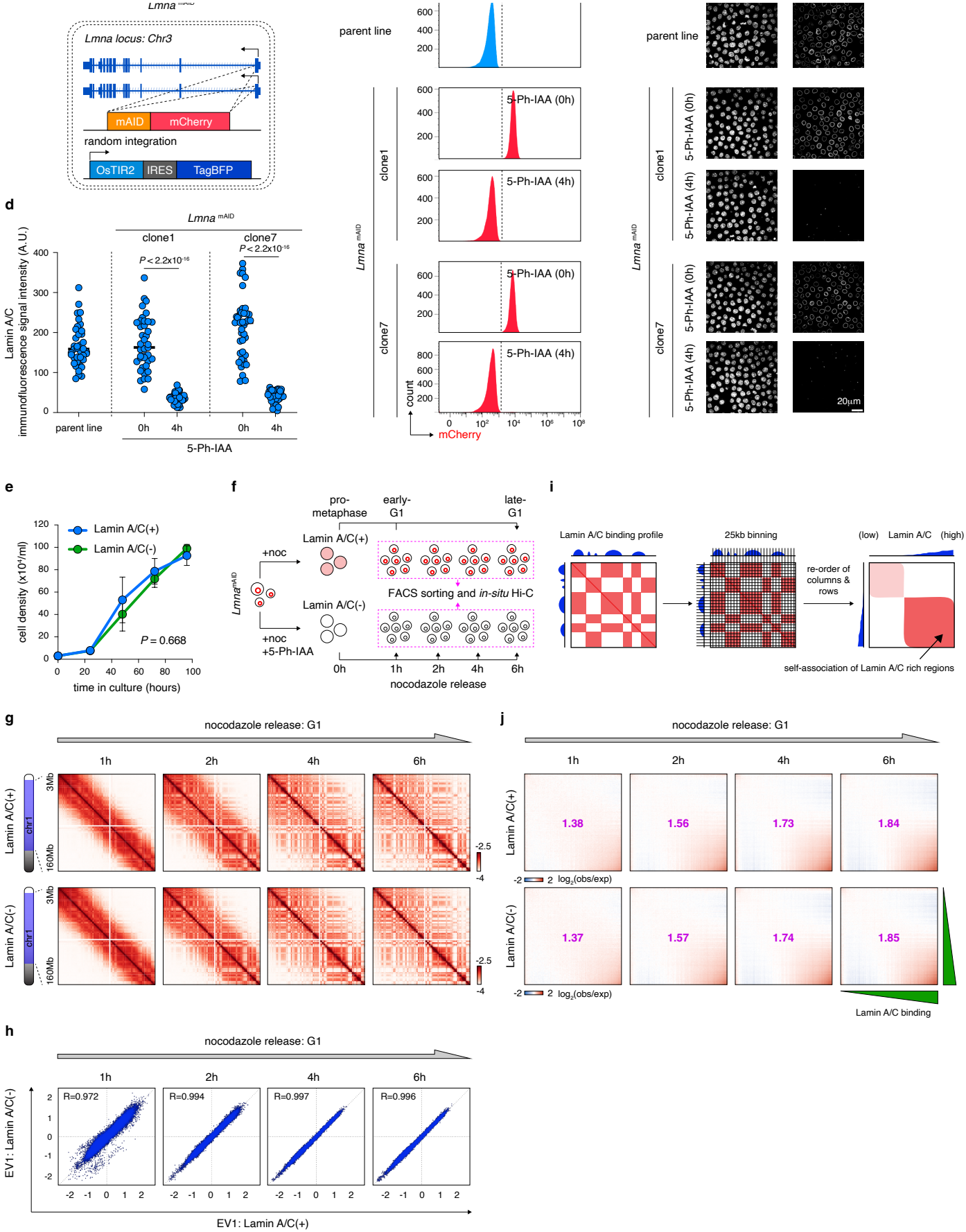

Extended Data Figure 2: Lamin A/C depletion does not affect post-mitotic chromatin re-compartmentalization. a, Schematic illustration, showing the genome editing strategy to generate the *Lmna*^{mAID} cell line. **b**, Flow plots showing the rapid degradation of Lamin A/C in response to 5-Ph-IAA treatment. **c**, Immunofluorescence staining showing the rapid depletion of Lamin A/C in response to 5-Ph-IAA treatment. One experiment was performed for each clone. Scale bar: 20μm. **d**, Quantification of (**c**). *P* values were calculated using a two-sided Wilcoxon signed-rank test. One experiment was performed for each clone. More than 30 cells were quantified for each clone. **e**, Line plot showing that cell growth was not affected by Lamin A/C depletion. Error bar denotes SEM (n=4). *P* value was calculated using two-sided *ANOVA* test. **f**, Schematic illustration, showing the strategy to harvest post-mitotic cells with or without Lamin A/C. **g**, KR-balanced, 100kb-binned, Hi-C contact maps showing that Lamin A/C depletion does not affect post-mitotic chromatin re-compartmentalization. **h**, Scatter plots showing the high correlation of EV1 values between Lamin A/C (+) and (-) samples after mitosis. **i**, Schematic illustration, showing the strategy to generate modified saddle plots based on Lamin A/C CUT&Tag signal. **j**, Modified saddle plots showing that Lamin A/C depletion does not affect the self-aggregation of Lamin A/C enriched genomic regions.

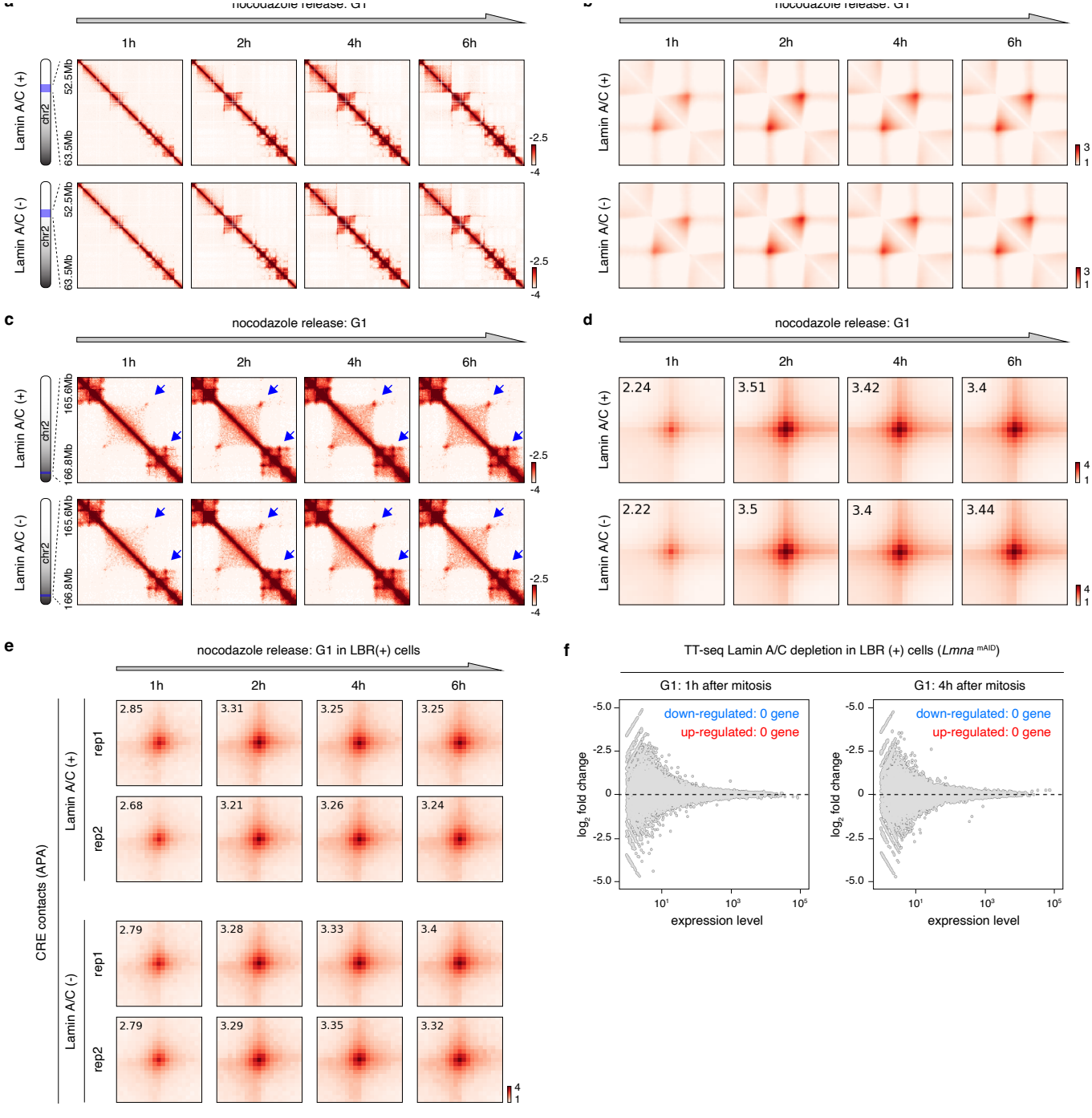

Extended Data Figure 3: Lamin A/C is dispensable for the post-mitotic re-establishment of TADs, structural loops, and CRE interactions, as well as transcriptional reactivation. a, KR-balanced, 25kb binned, Hi-C contact matrices showing that Lamin A/C depletion does not affect post-mitotic TAD reformation. **b**, Aggregated plots showing that TADs reformation were unaffected by Lamin A/C loss. **c**, KR-balanced, 10kb binned, Hi-C contact matrices showing that chromatin structural loop reformation (blue arrow) was unaffected by Lamin A/C loss after mitosis. **d**, Aggregated peak analysis (APA) showing that genome-wide structural loop reformation was unaffected by Lamin A/C loss after mitosis. **e**, APA plots showing that CRE contacts was unaffected by Lamin A/C loss after mitosis. **f**, Scatter plots showing that nascent transcripts (TT-seq) was unaffected by Lamin A/C depletion after mitosis.

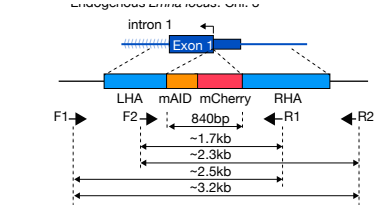

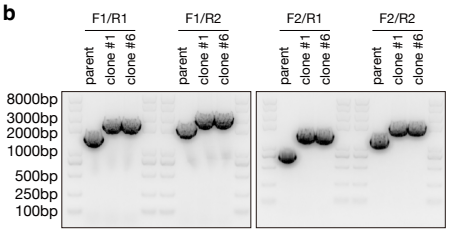

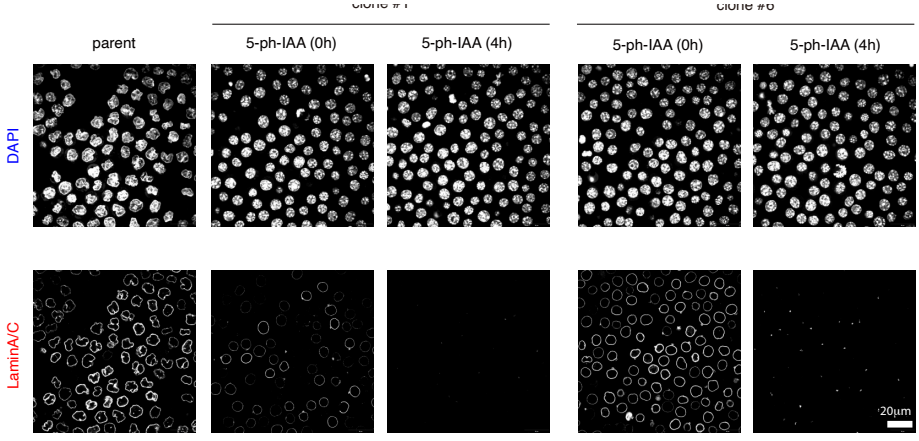

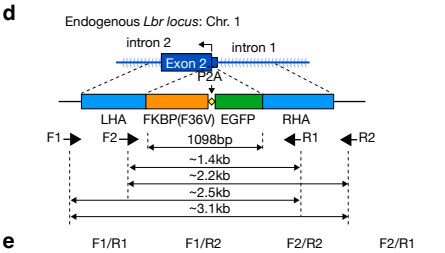

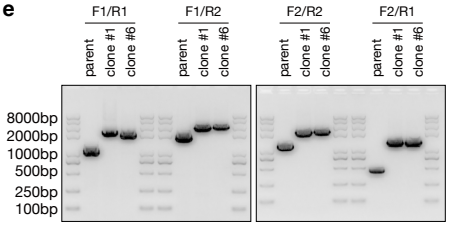

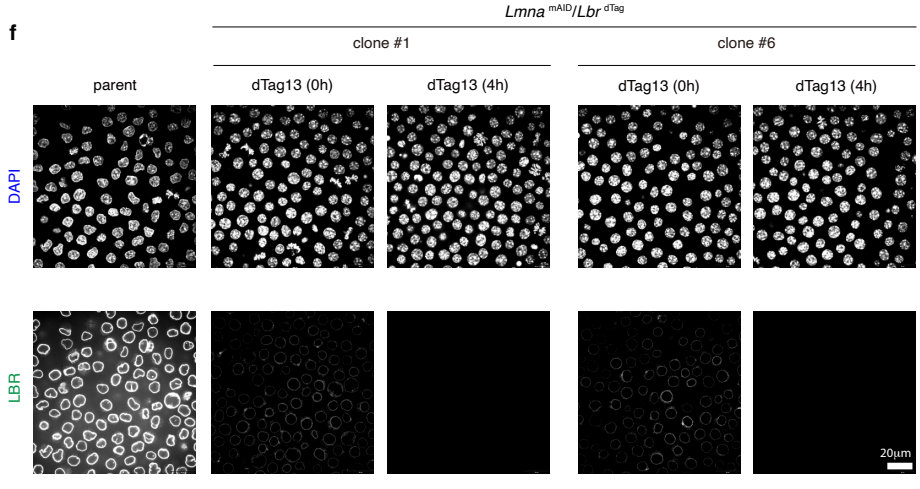

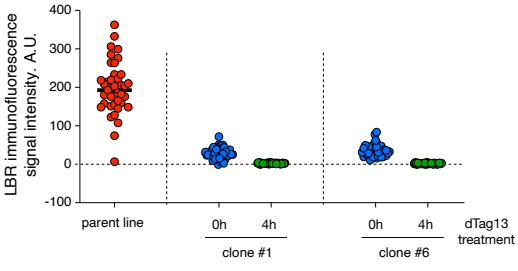

Extended Data Figure 4: Characterization of the *Lmna*^{mAID}/*Lbr*^{dTag} cell line. a, Schematic illustration, showing the genotyping strategy of *Lmna* locus. **b**, Genotyping results showing the homozygous insertion of mAID-mCherry into *Lmna* locus. **c**, Immunofluorescence staining showing Lamin A/C depletion upon 5-Ph-IAA treatment. Scale bar 20μm. **d**, Schematic illustration, showing the genotyping strategy of *Lbr* locus. **e**, Genotyping results showing the homozygous insertion of dTag-P2A-EGFP into *Lbr* locus. **f**, Immunofluorescence staining showing the background degradation of LBR and the complete degradation of LBR upon dTag13 treatment. Scale bar 20μm. **g**, Quantification of (**f**). One experiment was performed for each clone. More than 30 cells were calculated.

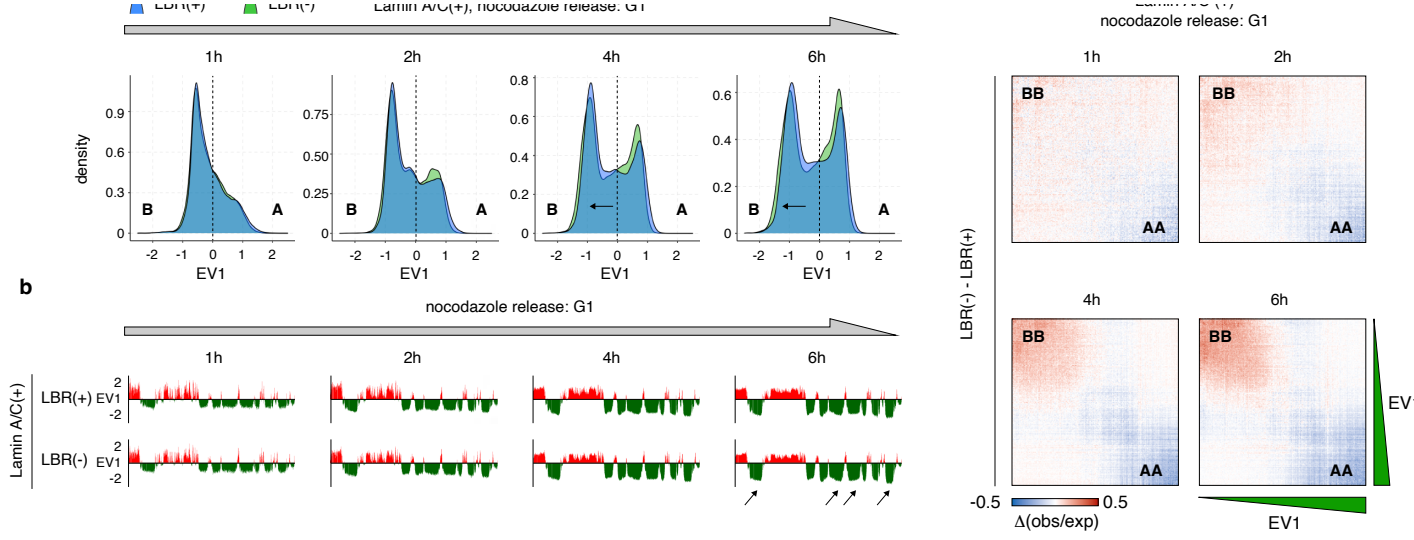

b

Extended Data Figure 5: LBR depletion strengthens post-mitotic B-B compartmental interactions. a, Density plots showing the distribution of EV1 values in LBR-deficient and replete cells across post-mitotic time points. Note that EV1 values shifted toward the negative direction upon LBR loss in late-G1 stages (arrows), suggesting strengthened B-B compartmental interactions. **b**, Representative genome browser tracks (chr2:120-150Mb) showing the shift of EV1 values toward the negative direction (black arrows) in B-type compartments. **c**, Differential saddle plots showing progressively increased B-B contacts upon LBR depletion after mitosis.

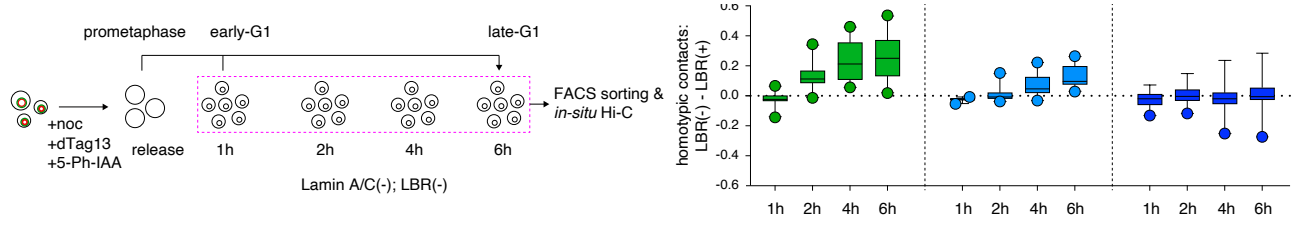

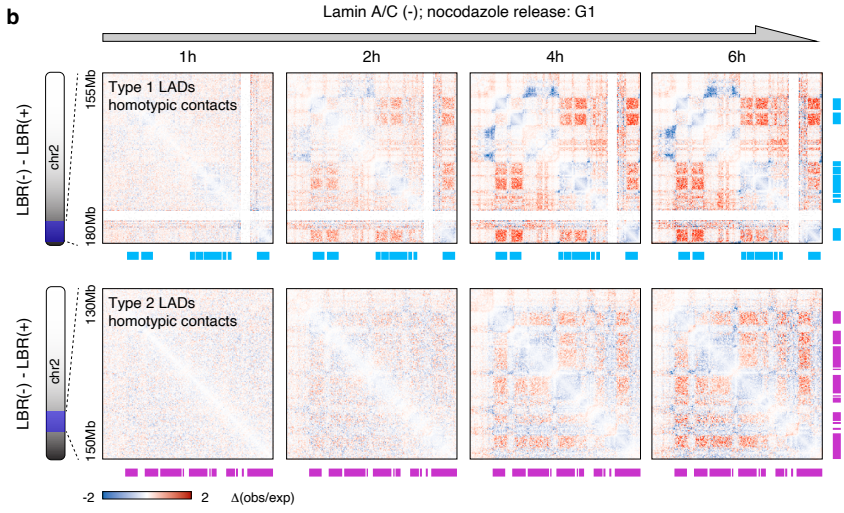

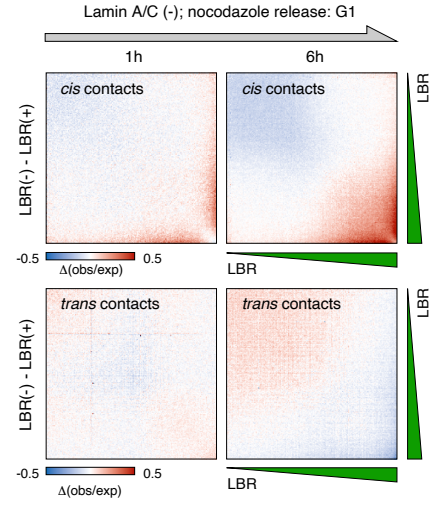

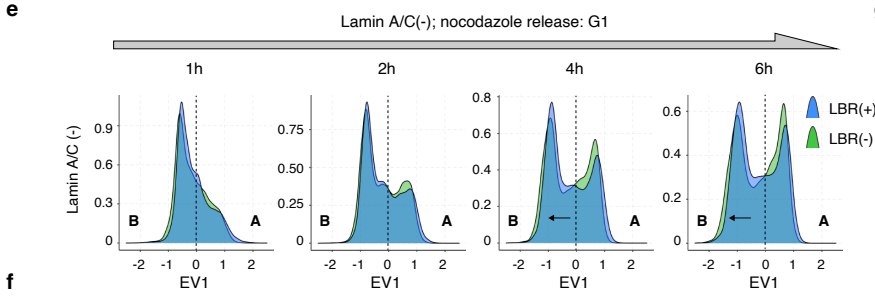

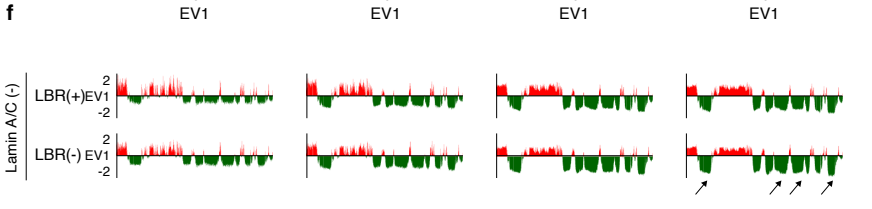

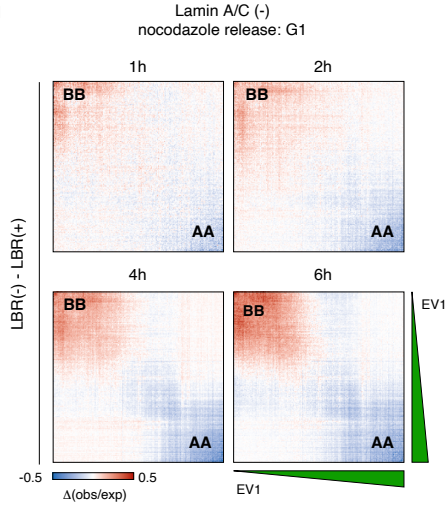

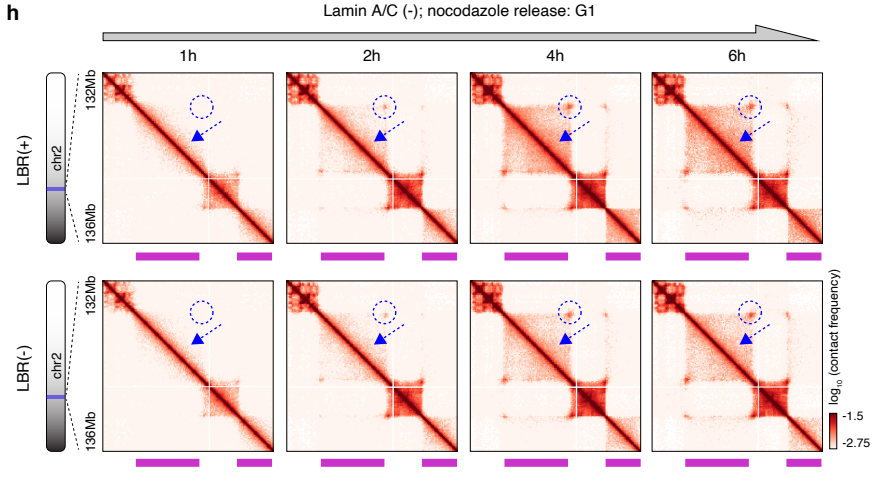

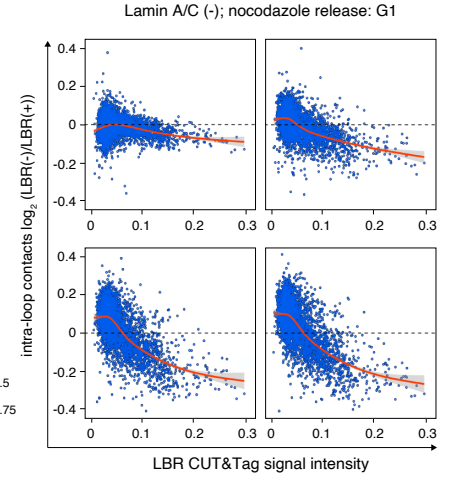

Extended Data Figure 6: LBR depletion induces LAD self-association and increases B-B contacts in Lamin A/C-deficient cells after mitosis. a, Schematic illustration, showing the strategy to obtain Lamin A/C and LBR co-depleted cells after mitosis. **b**, Differential KR-balanced, 100kb binned Hi-C contact matrices showing the progressive gain of homotypic interactions among type1 or type2 LADs upon LBR depletion in Lamin A/C-deficient cells after mitosis. Type1 and 2 LADs were demarcated by blue and purple bars respectively. **c**, Boxplots showing that LBR depletion triggered progressive increments of homotypic interactions within type1 and 2 LADs in Lamin A/C-deficient cells. **d**, Differential LBR-based saddle plots showing strengthened LAD self-association in *cis* but not in *trans* upon LBR depletion in Lamin A/C-deficient cells in late-G1 phase. **e**, Density plots showing the distribution of EV1 values upon LBR removal in Lamin A/C-deficient cells across post-mitotic time points. Note that EV1 values shifted toward the negative direction upon LBR loss in late-G1 stages (arrows), suggesting strengthened B-B compartmental interactions. **f**, Representative genome browser tracks (chr2:120-150Mb) showing the shift of EV1 values toward the negative direction (black arrows) in B-type compartments in Lamin A/C-deficient cells. **g**, Differential saddle plots showing progressively increased B-B contacts upon LBR depletion after mitosis, in Lamin A/C-deficient cells. **h**, KR-balanced, 25kb binned Hi-C contact matrices that the intra-loop contacts were reduced by LBR depletion in late-G1 phase in Lamin A/C-deficient cells (dotted arrow). **i**, Scatter plots showing that intra-loop contact reduction upon LBR loss is positively correlated with internal LBR signal intensity in Lamin A/C-deficient cells. For all boxplots, central line denotes median. Box limits denote 25th–75th percentile; whiskers denote 5th–95th percentile.

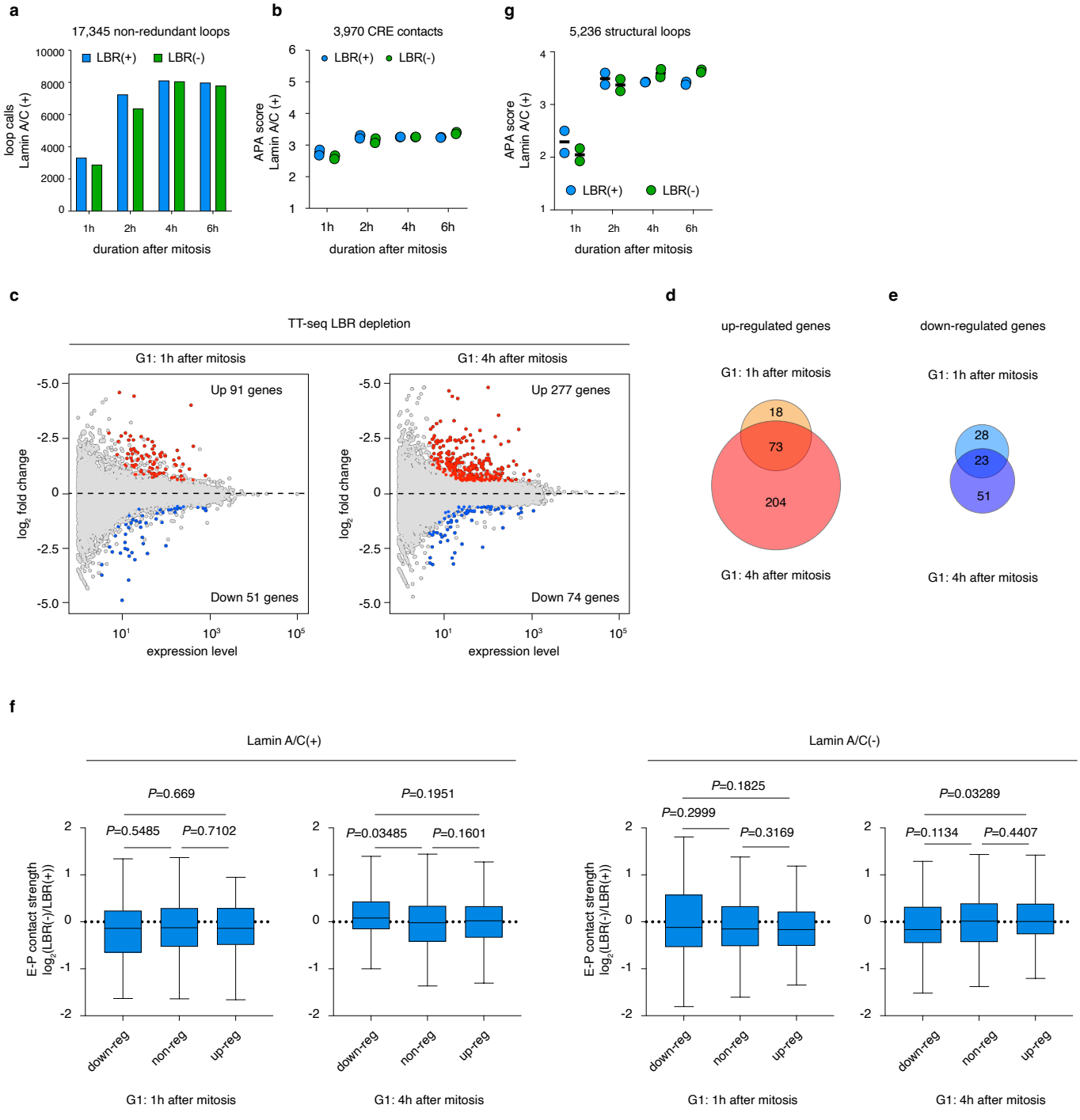

Extended Data Figure 7: LBR loss-induced transcription dysregulation is not caused by dysregulated E-P contacts. a, Bar graph showing the number of loop calls in LBR (+) and LBR (-) samples after mitosis. **b**, Dot plots showing that CRE contact strength (APA score) was not affected by LBR loss after mitosis. **c**, Scatter plots showing the $\log_2$ fold change (FC) in gene body TT-seq signal in early and late-G1 after LBR depletion. **d**, Venn-diagram showing that 73 up-regulated genes were shared between early- and late-G1 phase samples upon LBR loss. **e**, Venn-diagram showing that 23 down-regulated genes were shared between early- and late-G1 phase samples upon LBR loss. **f**, Box plots showing that E-P contact frequencies are decoupled from transcriptional changes in LBR-deficient cells. Box limits denote 25th–75th percentile; whiskers denote 5th–95th percentile. *P* values were calculated using a two-sided Wilcoxon signed-rank test. **g**, Dot plots showing that structural loop strength (APA score) was only minimally affected by LBR loss after mitosis.

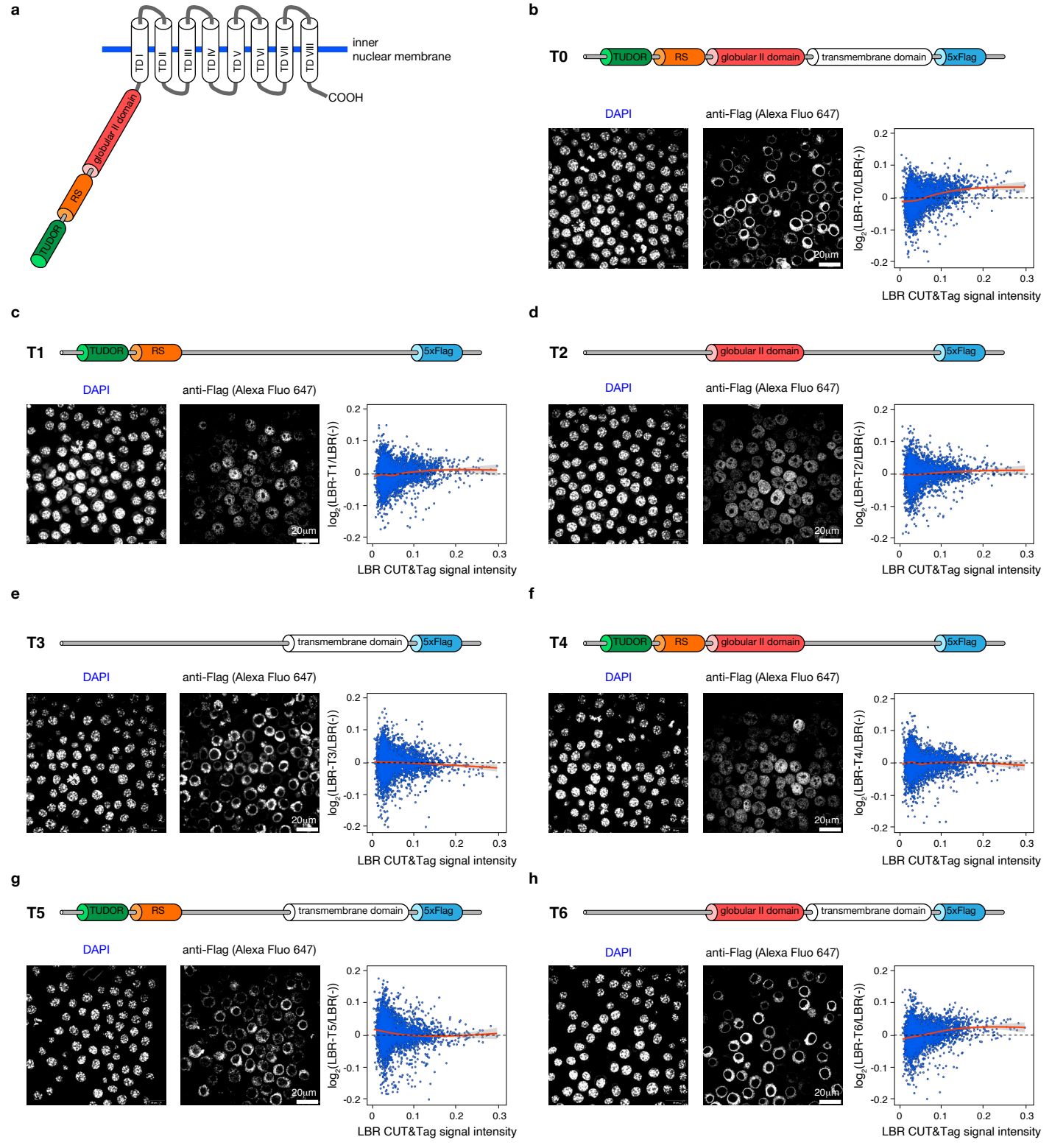

Extended Data Figure 8: Rescue of intra-loop contact frequency in LBR-deficient cells through ectopic LBR expression. a, Schematic illustration, showing the Tudor/RS, second globular, and transmembrane domains of LBR. **b-h**, Top panel: schematic illustration, showing the full-length or truncated mutants of LBR to be ectopically expressed in LBR-deficient cells. Lower left panel: Immunofluorescence staining showing the subcellular localization of full-length or truncated mutants of LBR. Scale bar: 20μm. Lower right panel: Scatter plot showing the changes in late-G1 phase intra-loop contact strength upon the introduction of full-length or truncated LBR mutants. Note that the transmembrane domain of LBR is required to rescue LBR's effect on intra-loop contacts.

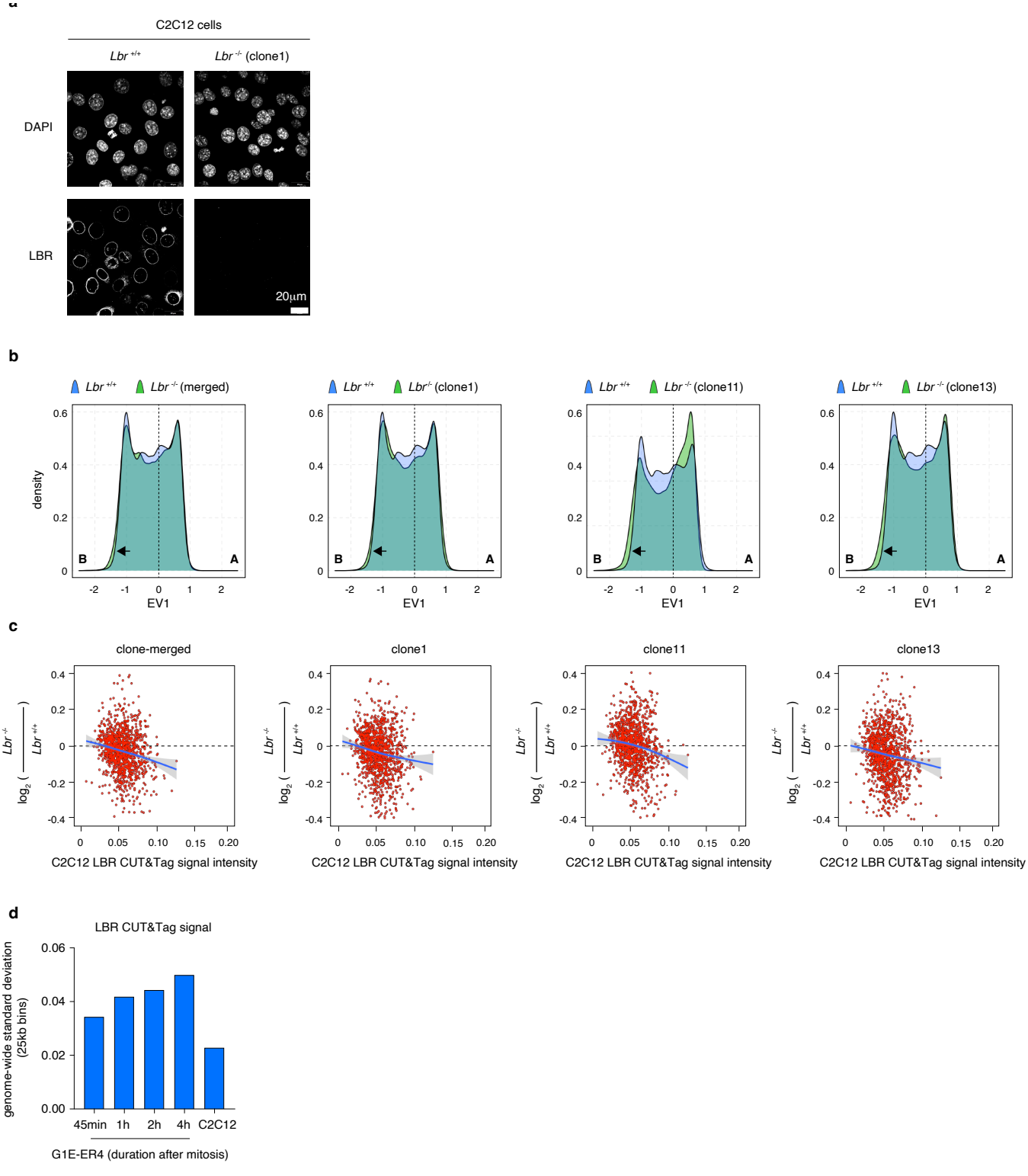

Extended Data Figure 9: LBR depletion in C2C12 cells recapitulates the attenuation of intra-loop contact frequency. a, Representative immunofluorescence staining confirming the loss of LBR in the LBR-knockout clone. Scale bar: 20μm. **b**, Density plots showing that the distribution of EV1 values shifted towards the negative direction (arrows) by LBR depletion in C2C12 cells. Plots for both clone-merged and independent clones were shown. **c**, Scatter plots showing the correlation between internal LBR signal strength and intra-loop contact strength reduction upon LBR loss. Plots for both clone-merged data and independent clones were shown. **d**, Bar graph showing the genome-wide standard deviation of LBR CUT&Tag signals in G1E-ER4 cells and C2C12 cells.

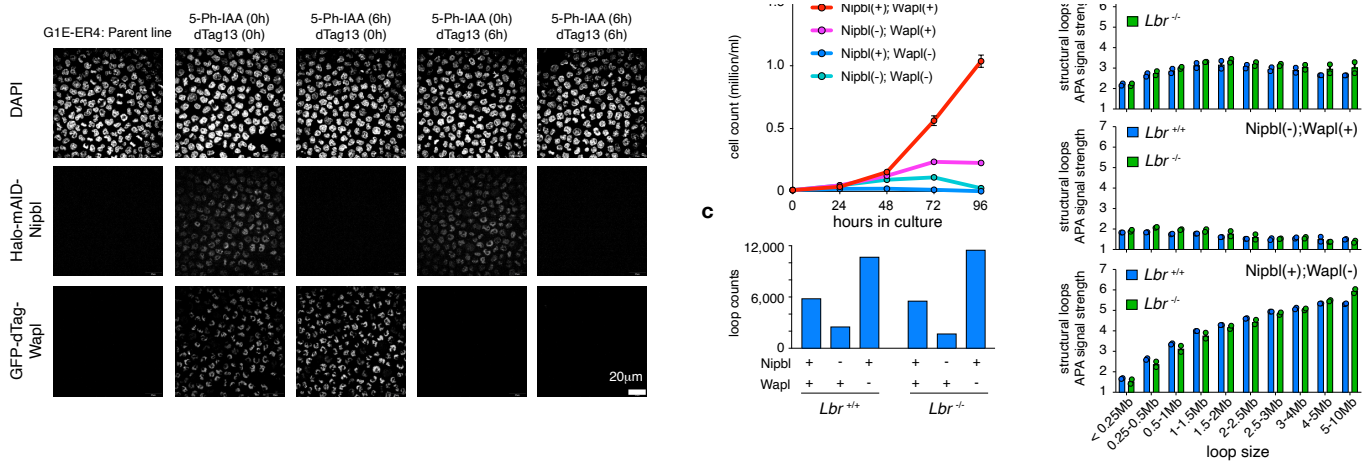

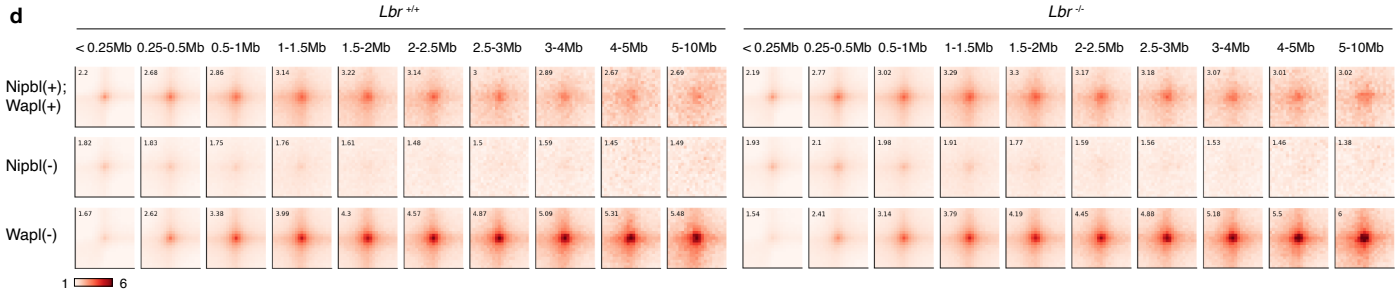

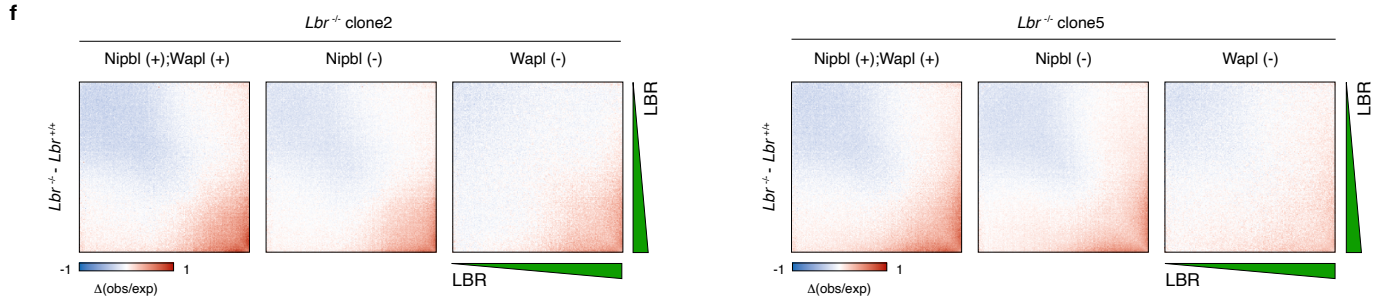

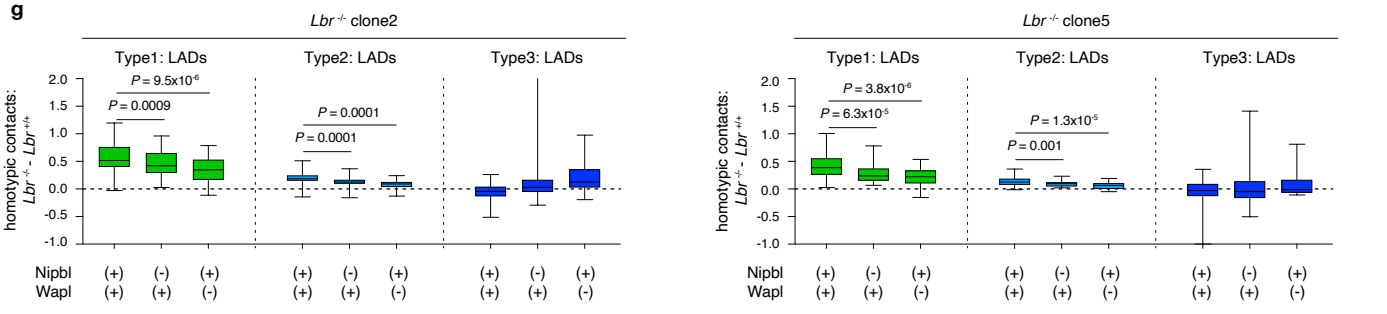

Extended Data Figure 10: Impact of LBR depletion on chromatin architecture in Nipbl- or Wapl-deficient backgrounds. a, Fluorescence images showing the loss of Nipbl or/and Wapl upon 5-Ph-IAA or/and dTag13 treatment. Scale bar: 20μm. **b**, Growth curve showing that Nipbl and Wapl were both crucial for cell growth. Error bar denotes SEM (n=3). **c**, Bar graphs showing the number of loop calls in cells with indicated configurations of Nipbl and Wapl. **d**, APA plots showing the effects of Nipbl or Wapl depletion on structural loops. Results in both $Lbr^{+/+}$ and $Lbr^{-/-}$ cells were shown. **e**, Bar graphs showing the quantification of (**d**). **f**, Differential LBR-based saddle plots for independent clones showing that the strengthened LAD self-association was weakened by Nipbl or Wapl depletion. **g**, Boxplots showing that the LBR loss-induced gain of LAD self-association was attenuated in cells lacking Nipbl or Wapl. Plots were shown for two independent clones separately. For all boxplots, central line denotes median. Box limits denote 25th–75th percentile; whiskers denote 5th–95th percentile. *P* values were calculated using a two-sided paired Wilcoxon signed-rank test.

a

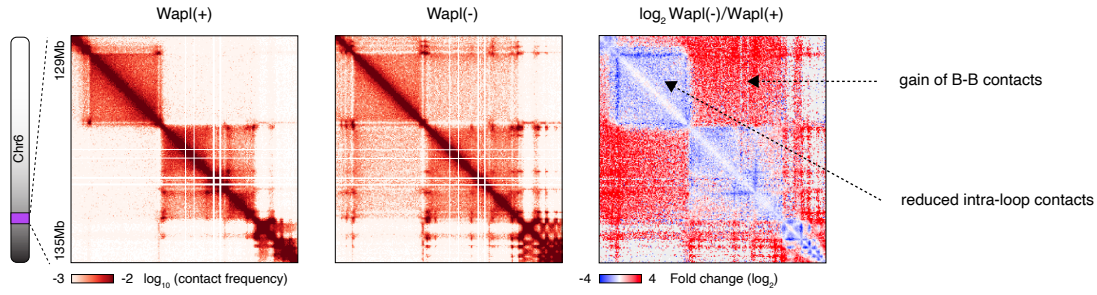

b

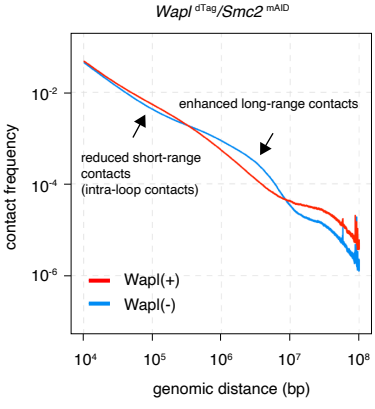

Extended Data Figure 11: Wapl depletion induces a characteristic shift in the P_S curve, featuring the attenuation of intra-loop contacts and a concomitant increase in B-B compartmental interactions. a, KR-balanced, 25kb-binned, Hi-C contact maps showing that the intra-loop contacts were reduced and that B-B compartmental interactions were strengthened in Wapl-depleted cells. **b**, P_S curves showing the bi-directional shifts of contact frequency induced by Wapl depletion in asynchronous population.

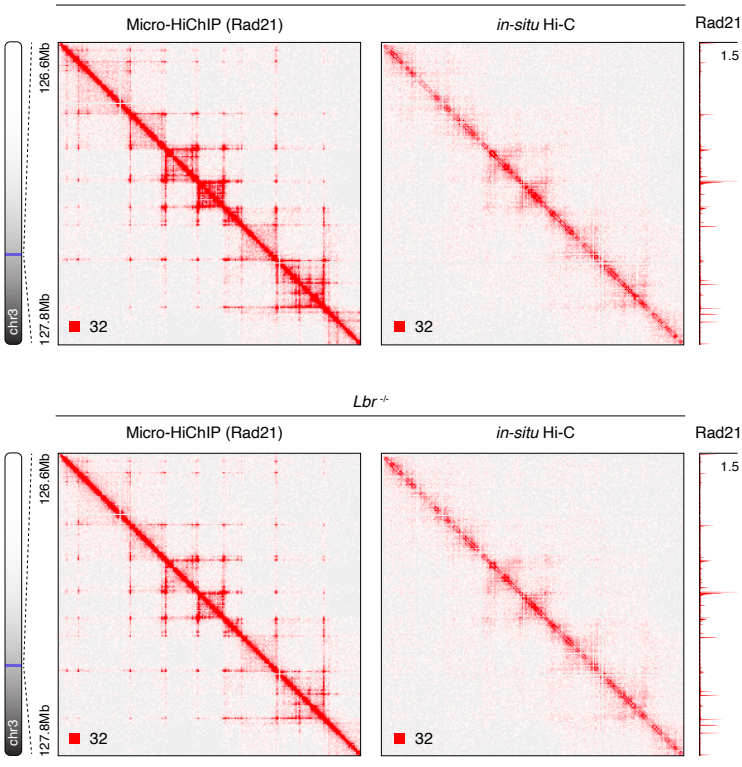

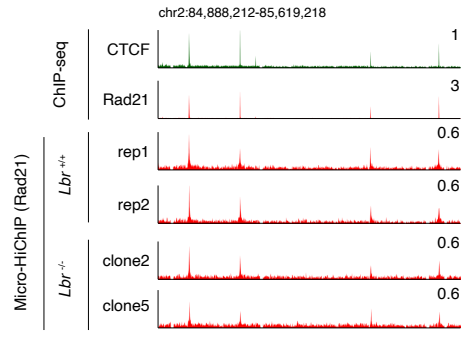

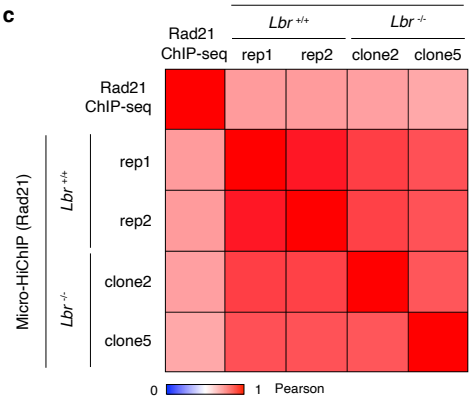

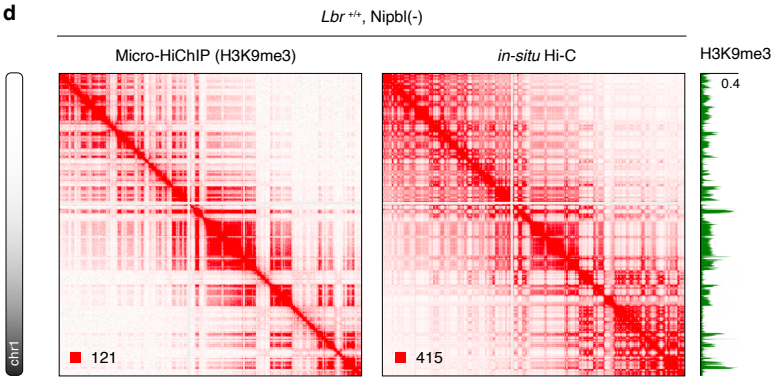

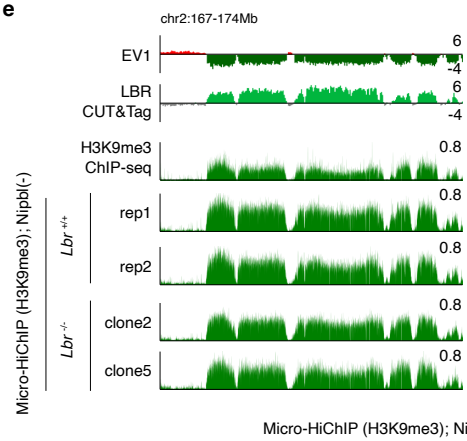

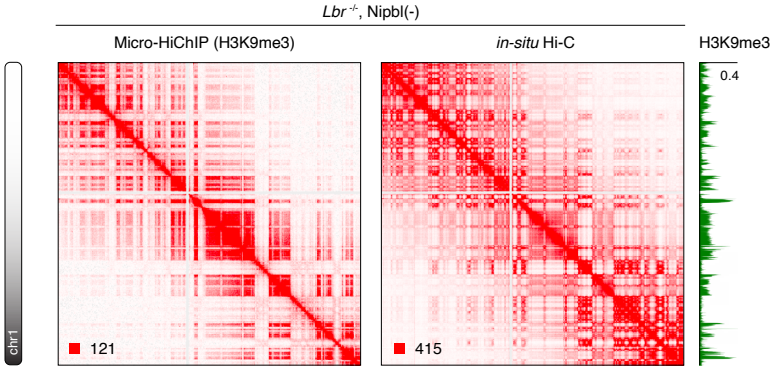

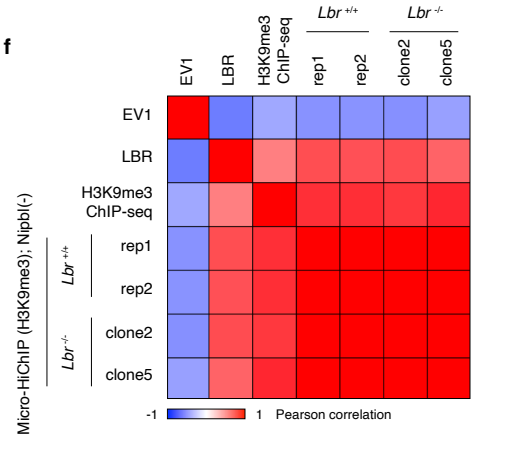

Extended Data Figure 12: Characterization of Rad21 and H3K9me3-targeting micro-HiChIP assays. a, Raw, 5kb-binned Rad21 micro-HiChIP contact matrices and *in-situ* Hi-C contact matrices showing that micro-HiChIP could detect loops that are obscured by Hi-C. Maps for $Lbr^{+/+}$ and $Lbr^{-/-}$ samples are shown respectively. Rad21 ChIP-seq profiles are shown in parallel. **b**, Genomic browsers showing that micro-HiChIP could reproduce the genomic binding profiles of Rad21 from ChIP-seq. **c**, Heatmap showing the high correlation between micro-HiChIP biological replicates as well as between micro-HiChIP and ChIP-seq datasets. **d**, Raw, 100kb-binned micro-HiChIP and *in-situ* Hi-C contact matrices for H3K9me3 in Nipbl-deficient cells. Maps for $Lbr^{+/+}$ and $Lbr^{-/-}$ samples are shown respectively. H3K9me3ChIP-seq profiles are shown in parallel. **e**, Genomic browsers showing that micro-HiChIP could reproduce the ChIP-seq profiles of H3K9me3. **f**, Heatmap showing the high correlation between H3K9me3 micro-HiChIP biological replicates as well as between micro-HiChIP, ChIP-seq and EV1 (inverse correlation) profiles.

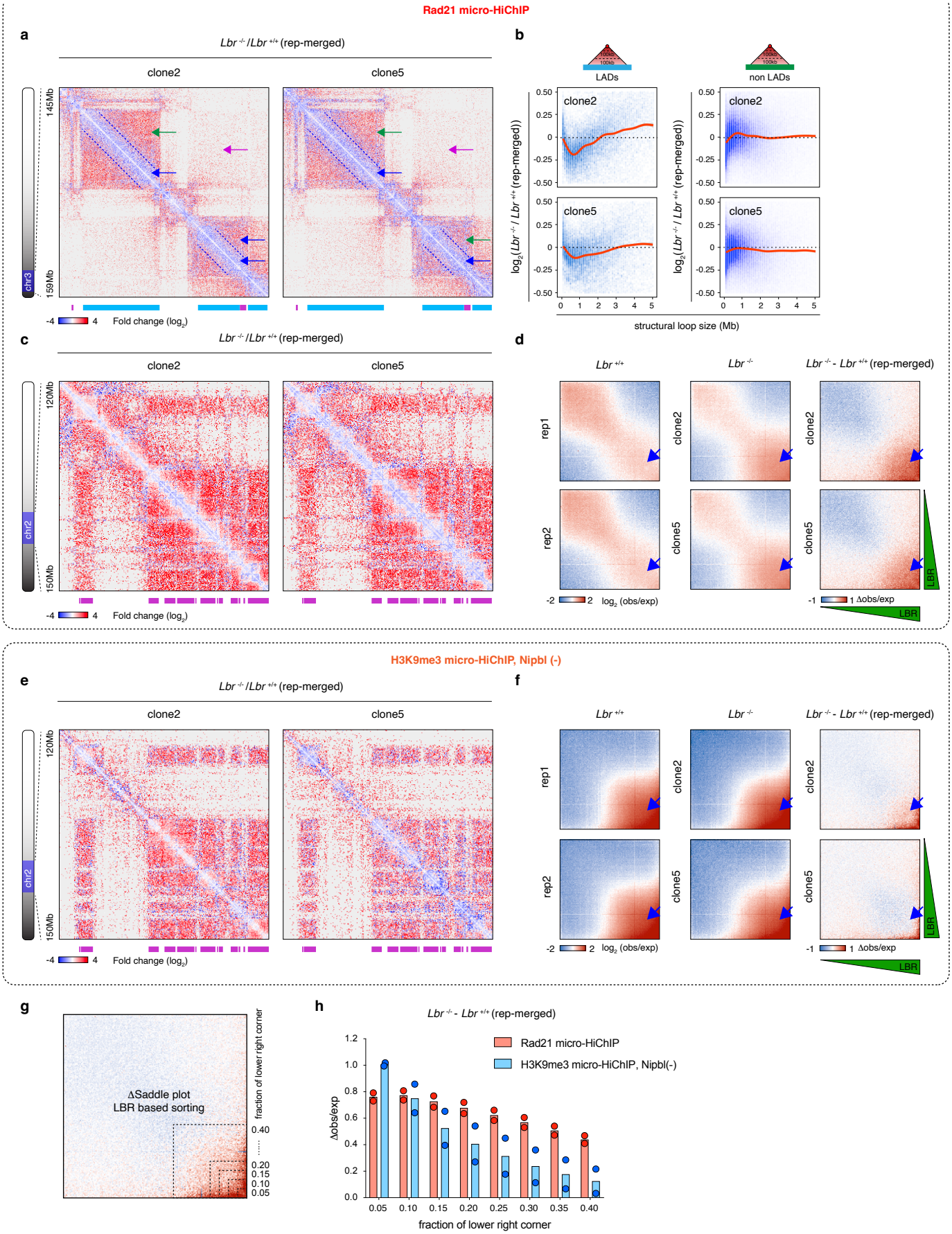

Extended Data Figure 13: Replicate reproducibility of Rad21 and H3K9me3-targeting micro-HiChIP assays. a, Raw, 25kb-binned Rad21 micro-HiChIP contact maps for each independent clone showing the expansion of cohesin-mediated contacts upon LBR loss. Concentrated short-range contacts at diagonal proximal regions are indicated by blue dotted lines. LBR-loss-induced reduction of short-range contacts and gain of long-range contacts within structural loops are indicated by blue and green arrows, respectively. Gain of inter-LAD contacts mediated by cohesin is indicated by the purple arrow. Type1 and 2 LADs are demarcated by blue and purple bars respectively. **b**, Line plots showing the LBR-loss induced reduction of cohesin-mediated short-range interactions and gain of longer range interactions within LAD-located structural loop domains. Line plots for each independent clone was shown. **c**, Raw, 100kb-binned micro-HiChIP contact matrices for each independent clone showing elevated levels of cohesin-mediated inter-LAD contacts upon LBR loss. LADs are demarcated by purple bars. Genomic tracks of EV1 values were shown in parallel. **d**, LBR-based saddle plots for each independent clone and biological replicate showing gain of cohesin-mediated LAD self-association upon LBR depletion. **e**, Raw, 100kb-binned micro-HiChIP contact matrices for each independent clone showing the slight increase of LAD self-association (measured by H3K9me3-associated contacts) without Nipbl. **f**, LBR-based saddle plots for each independent clone and biological replicate showing the gain of LBR-loss induced LAD self-association (measured by H3K9me3-associated contacts) in Nipbl-deficient cells. Note that such gain was only observed in regions heavily demarcated by LBR. **g**, Schematic illustration, showing the quantification of LBR-based saddle plots. **h**, Bar graph showing the quantification of (**d** & **f**) across different sections of the lower-right corner.

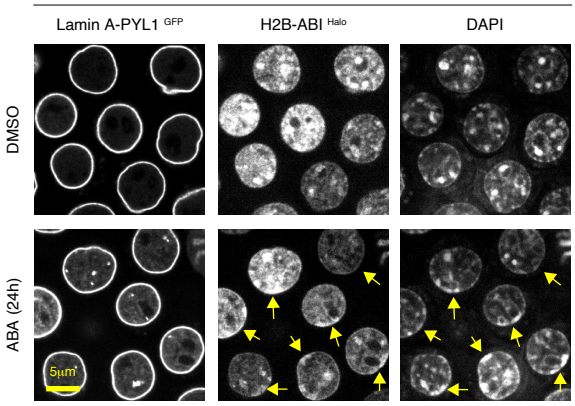

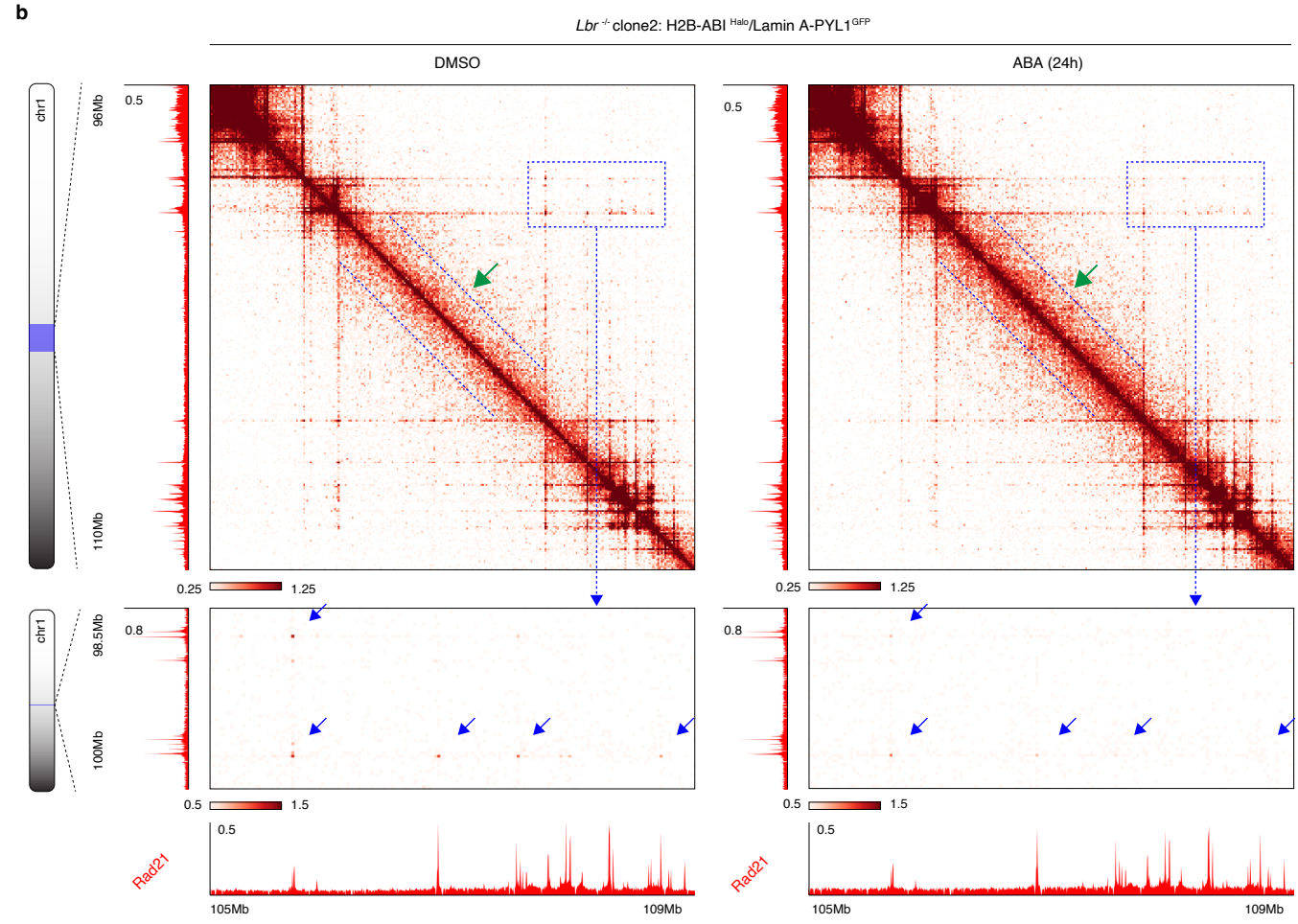

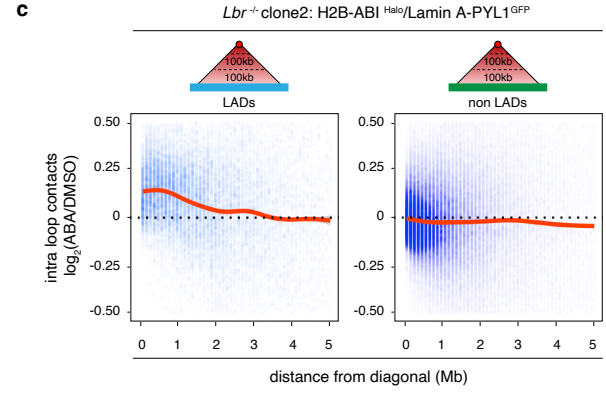

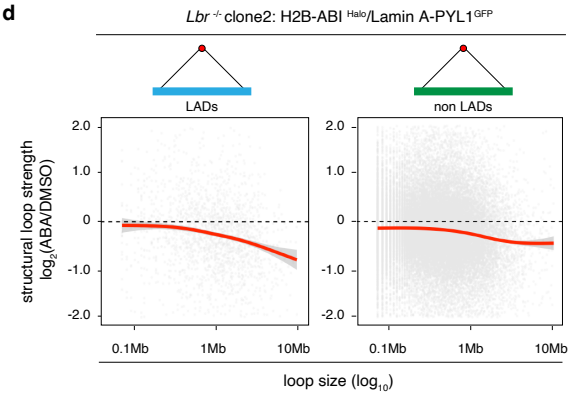

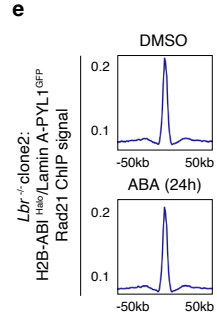

Extended Data Figure 14: Restricted cohesin loop extrusion in *Lbr*$^{-/-}$ cells (clone2) upon H2B-mediated bulk chromatin tethering to the NE. a, Representative images showing the nuclear periphery localization of H2B upon ABA treatment for 24 hours in clone2 *Lbr*$^{-/-}$ cells. **b**, Raw, 50kb-binned Rad21 micro-HiChIP contact matrices showing gain of cohesin-mediated short-range contacts (dotted blue lines and green arrows) within loop domains upon ABA treatment. Zoom-in views are 10kb-binned contact matrices showing reduced structural loop strength upon ABA treatment (blue arrows). Genomic tracks of Rad21 ChIP profile are shown in parallel. **c**, Line plots showing that ABA-induced H2B-mediated nuclear periphery anchor of bulk chromatin led to a gain of short-range intra-loop contacts within LAD-located loops. **d**, Line plots showing that bulk chromatin tether by ABA treatment leads to the reduction of large structural loop signal intensity. LAD and non-LAD located loops were shown respectively. **e**, Meta-region plots showing that Rad21 micro-HiChIP signal is not measurably affected upon ABA treatment.

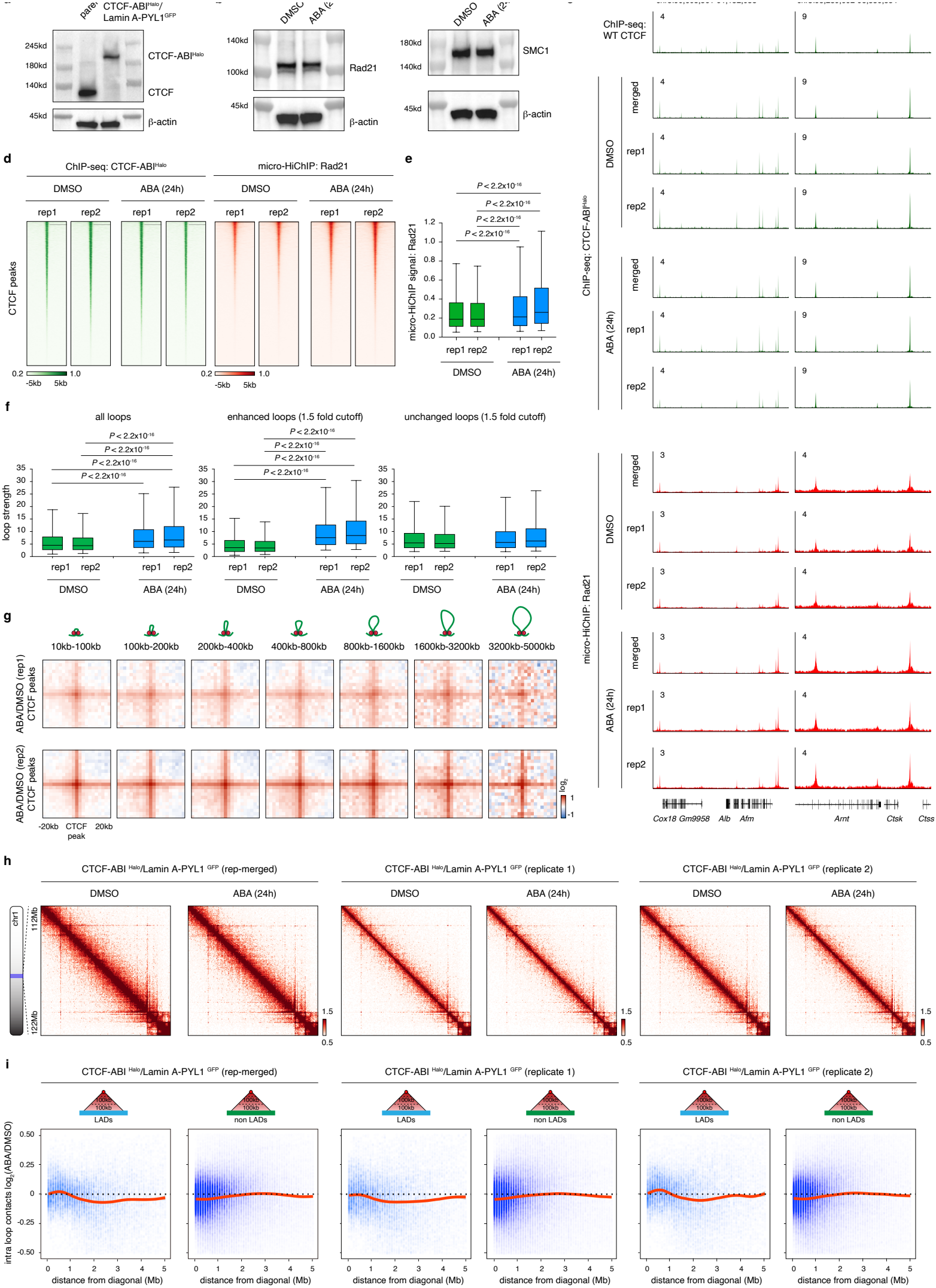

Extended Data Figure 15: NE tethering of CBS stabilizes chromatin loops without affecting cohesin processivity. a, Western blot analysis showing the size shift of endogenous CTCF-ABI^{Halo} compared to wildtype CTCF. **b**, Western blot showing that cohesin subunits Rad21 and SMC1 protein levels were not affected by ABA treatment. **c**, Genome browser tracks of CTCF (ChIP-seq) and Rad21 (micro-HiChIP) before and after ABA treatment. Tracks of replicate-merged and individual biological replicates replicates are shown respectively. **d**, Heatmap showing the ChIP-seq signals of CTCF-ABI^{Halo} and the micro-HiChIP signals of Rad21 for each biological replicate before and after ABA treatment. **e**, Boxplots showing the reproducible increase of Rad21 micro-HiChIP signal upon ABA treatment. **f**, Boxplots showing the reproducible strengthening of chromatin loops after ABA treatment. **g**, APA plots (1kb) showing the log2 fold change (ABA relative to DMSO) for two biological replicates for all possible pairs of CTCF peaks, stratified by genomic separation. **h**, Raw, 50kb binned Rad21 micro-HiChIP contact maps showing that short-range intra-loop contacts were not increased upon ABA treatment. Plots for replicate-merged and individual replicates were shown separately. **i**, Line plots showing that short-range intra-loop contacts within LAD-located loop domains were not increased upon ABA treatment. For all boxplots, central line denotes median. Box limits denote 25th–75th percentile; whiskers denote 5th–95th percentile. *P* values were calculated using a two-sided paired Wilcoxon signed-rank test.

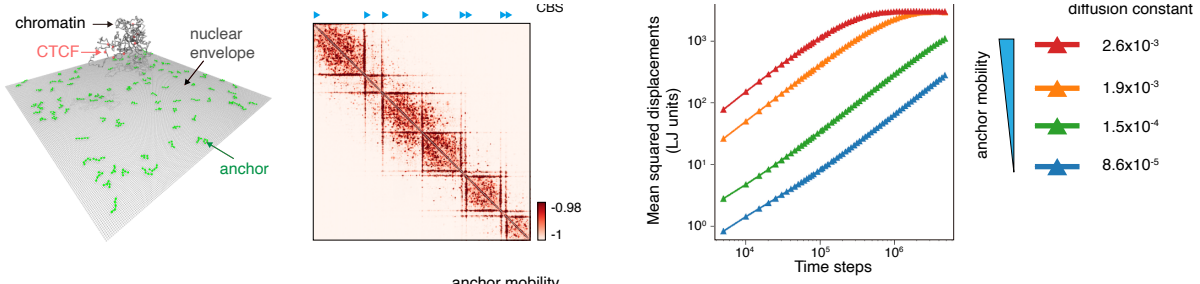

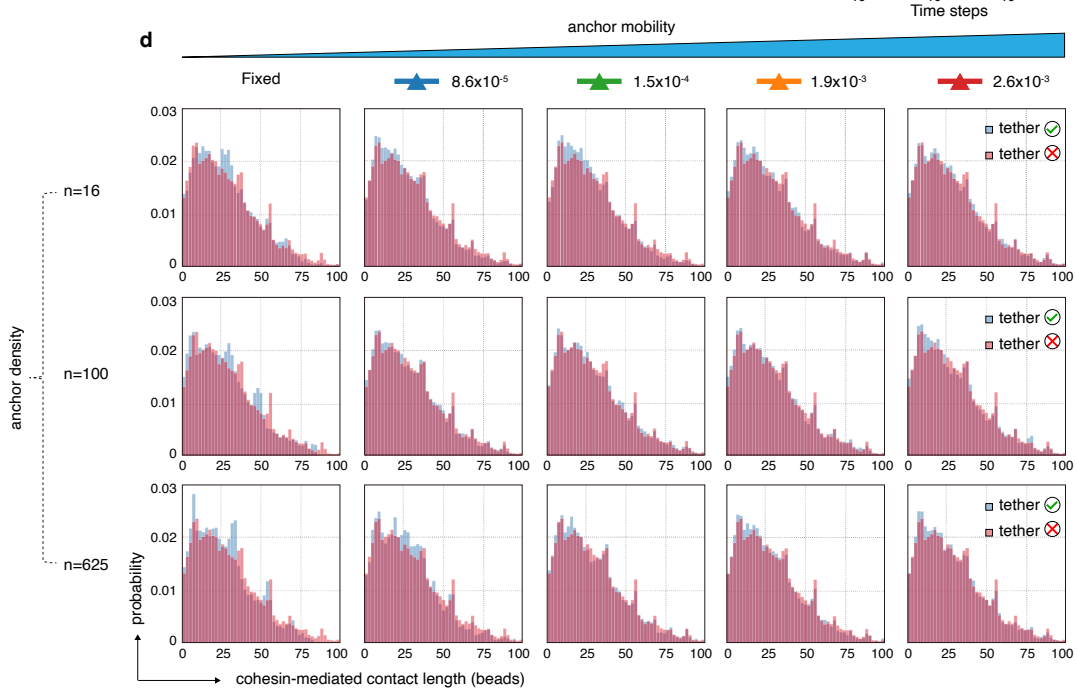

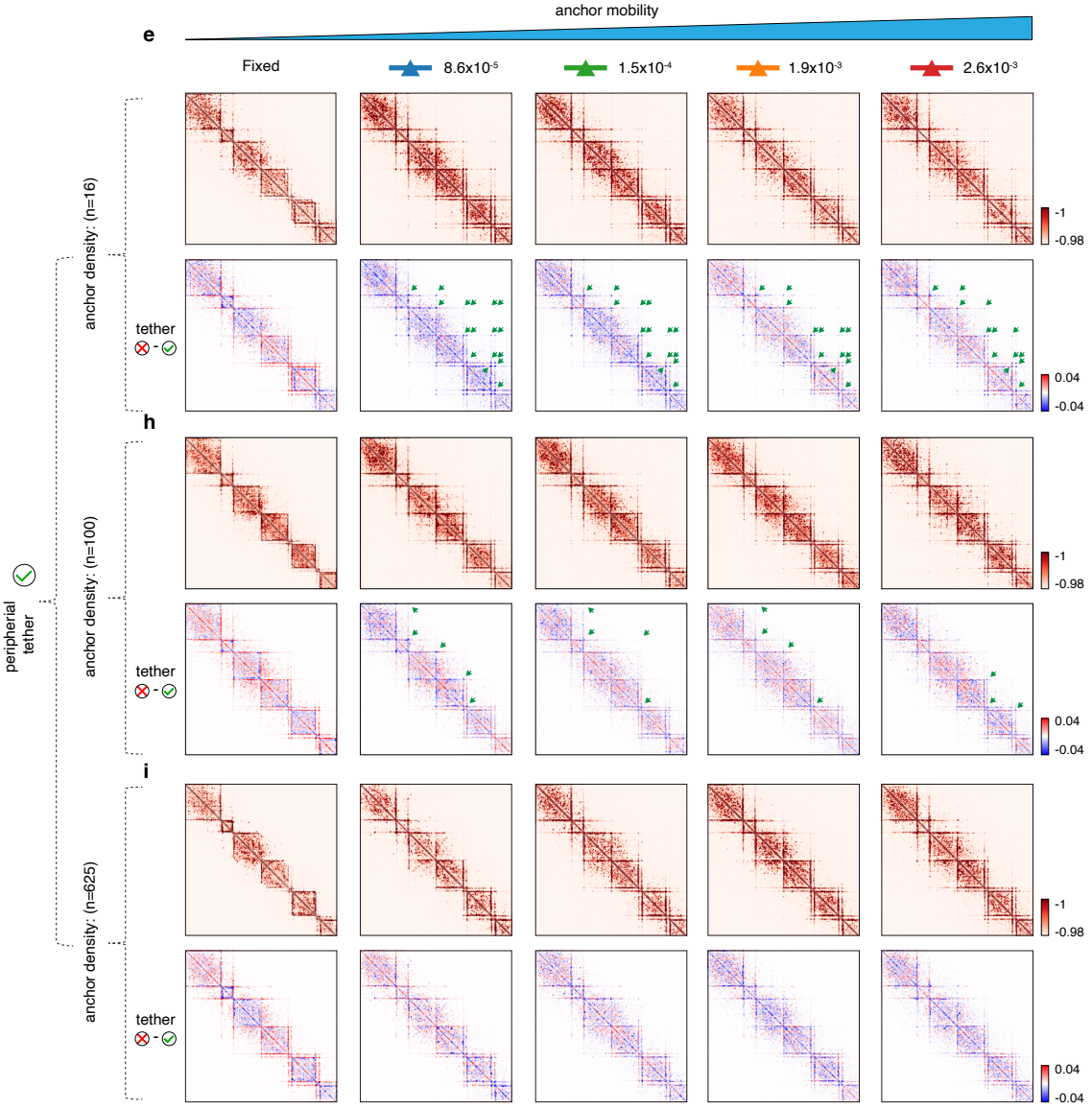

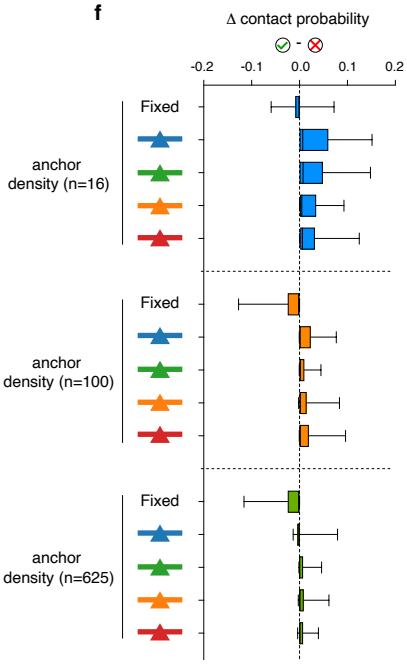

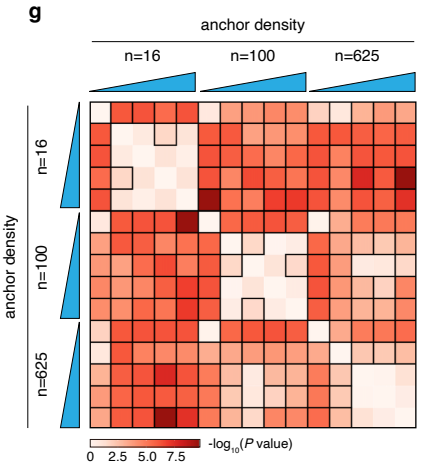

Extended Data Figure 16: Polymer simulations of CBS focal tethering across a range of lateral anchor mobility. a, Simulation snapshot of a uniform chromosome homopolymer in the absence of A/B compartment partitioning and NE attachment. **b**, Simulated contact map of cohesin-mediated interactions for the unpartitioned polymer shown in (**a**). CBS directions are indicated by blue and red triangles. **c**, Diffusion dynamics of peripherally adsorbed anchor under varying simulation conditions. Mean squared displacement (MSD) of purely adsorbed anchor molecules localized at the NE is plotted as a function of lag time (Δt). Four distinct simulation parameter regimes are represented by solid lines in different colors. Corresponding diffusion constants were derived from linear fits to the MSD curves. **d**, Histograms showing the frequency distribution of cohesin-mediated contact lengths for control and CBS tethered simulations across the indicated anchor densities and lateral anchor mobility. **e**, Upper panel: Simulated contact maps showing cohesin-mediated interactions during focal CBS tethering across the indicated range of lateral anchor mobilities (fixed parameters: anchor density = 16, CBS/anchor affinity = 5.0). Lower panel: Differential contact maps (tethered minus control) illustrating shifts in CTCF loop strength upon peripheral CBS anchorage. Green arrows highlight visible reductions in loop intensity. **f**, Boxplots showing the change in contact probability (Δ contact probability, tethered minus control) for all convergent CTCF pairs. **g**, Heatmap of $\log_{10}$-transformed *P*-values (two-sided paired Wilcoxon rank-sum test) for pairwise comparisons of the conditions shown in (**e**). Significant differences ($P < 0.05$) are indicated by black borders. **h** & **i**, Similar to (**e**), showing the simulated contact maps of cohesin-mediated contacts with CBS tethering across the indicated range of lateral anchor mobility at mid (n=100) and high (n=625) anchor density, respectively. For all boxplots, central line denotes median. Box limits denote 25th–75th percentile; whiskers denote 5th–95th percentile.